Pixel Array Application of High Temperature Superconducting YBCO Transition Edge Infrared Bolometers

A Thesis Submitted to
the Graduate School of Engineering and Sciences of
İzmir Institute of Technology
in Partial Fulfillment of the Requirements for the Degree of

Master of Science

in Physics

by
Barış PEKERTEN

March 2009
İZMİR

We approve the thesis of **Barış PEKERTEN**

Prof. Dr. Doğan ABUKAY
Supervisor

Yrd.Doç.Dr. Yusuf SELAMET
Committee Member

Doç. Dr. Mustafa TEPE
Committee Member

19 March 2009

Prof. Dr. Durmuş Ali DEMİR
Head of Physics Department

Prof. Dr. Hasan BÖKE
Dean of the Graduate School of
Engineering and Sciences

ACKNOWLEDGEMENTS

Many people have contributed, directly or indirectly, to this thesis. I would like to thank my advisor, Prof. Dr. Doğan ABUKAY for his guidance. My lab partner, Mr. H. Yusuf Günel, deserves much more than a "Thank you" for being there through the thick and the thin, and for being a great friend. I would also like to thank Dr. İlbeyi Avcı for his mentoring and his showing the ropes to us. Without him, this work would have been impossible. I also appreciate greatly Dr. Ali Bozbey's generous sharing of his experiences in the topic of high T_c bolometers. Dr. Mustafa Tepe's assistance has greatly facilitated this work. He graciously opened his lab and the equipment within to us. The distance between our lab and Dr. Tepe's lab would have been prohibitively large and the completion of this work nearly impossible had my father, Dr. Bülent Pekerten, not volunteered to provide us transport at no cost to us whenever we needed it. I would also like to thank all of my friends and colleagues at the IYTE Physics Department, not the least for their companionship during the long, long lab nights. Last but not the least, I would like to thank my family for being understanding and being always there for me.

This work was partly supported by IYTE-BAP-11.

ABSTRACT

PIXEL ARRAY APPLICATION OF HIGH TEMPERATURE SUPERCONDUCTING YBCO TRANSITION EDGE INFRARED BOLOMETERS

In this thesis, we patterned pregrown epitaxial YBCO thin films on MgO, LAO and STO substrates into meander shaped high-T_c superconducting transition edge monolithic bolometers. We set up and automatized the electrical characterization processes of the bolometers. We also measured the bolometric response of the meanders to red and near-infrared light and fit them to theoretical models in literature. We compared the single pixel bolometric responses to literature and found that our results are similar to or better than the results for similar devices in the literature.

We also patterned staring arrays (focal plane arrays) and explored the resolution limit put in place by thermal crosstalk. We compared the measured crosstalk to theory and found a very good agreement. We quantified the crosstalk for our pixels. We then explored substrate etching method to decrease crosstalk via thermal isolation.

ÖZET

YÜKSEK SICAKLIK ÜSTÜNİLETKEN YBCO GEÇİŞ KENARI KIZILÖTESİ BOLOMETRELERİN GÖZEK DİZESİ UYGULAMASI

Bu tezde önceden MgO, STO ve LAO alttaşları üzerine epitaksiyel olarak büyütülmüş YBCO ince filmlerini kıvrımlı yüksek sıcaklık tek katmanlı üstüniletken bolomet-releri olarak şekillendirdik. Elektronik karakterizasyon işlemini hazırladık ve otomatikleştirdik. Kıvrımların kırmızı ve yakın kızılötesi ışıklara karşı bolometrik tepkisini ölçtük ve literatürle karşılaştırdık. Sonuçlarımızın literatürdekilere benzer veya onlardan daha iyi olduğunu gördük.

Ayrıca bu kıvrımlardan bakan gözek dizeleri (odak düzlemi dizeleri) oluşturduk ve bu dizelerin ısısal karşılıklı konuşmasından gelen çözünürlük sınırını araştırdık. Karşılıklı konuşmayı teoriyle karşılaştırdık ve deneyle çok iyi uyum bulduk. Gözeklerimizdeki karşılıklı konuşmayı sayısallaştırdık. Alttaş aşındırma yöntemiyle gözeklerin ısısal izolasyonunu arttırarak ısısal karşılıklı konuşmanın azalışının nasıl olabileceğini inceledik.

To family and friends,

TABLE OF CONTENTS

LIST OF TABLES

LIST OF FIGURES

CHAPTER 1

INTRODUCTION

1.1. Superconductivity

In this section, a brief background on superconductivity will be presented. For details and a fuller discussion, the reader will be referred to other sources. In the first subsection, a brief history of superconductivity research in superconducting materials and theory will be presented. Cryogenic requirements will be briefly touched upon. In the second subsection, basic concepts of low and high T_c superconductivity will be presented. In the final subsection, structural properties of $YBa_2Cu_3O_{7-\delta}$ that are relevant to this thesis will be mentioned. Optical absorbance of superconducting YBCO thin films will be discussed.

1.1.1. History and Overview

Since its discovery in the early twentieth century, superconductivity has attracted a lot of research, promising many applications. In no fewer than five times, and most recently in 2003, the Nobel prize in physics was awarded directly for research in superconductivity. Many applications of superconductivity exist and many more are being researched. Many engineering firms are working on making better superconducting wires, both for energy transportation and for giant electromagnet production. Maglev trains are used daily in Japan. Superconducting magnets are used in particle accelerators as well as in medicine in magnetic resonance imaging. On the micro- to nano-scale, superconducting circuits utilizing RSFQ technology are promising to take over the territory where semiconducting circuits cannot compete in speed and power consumption. Logic gates using this technology has long since been demonstrated. SQUID sensors are the most sensitive magnetic field sensors known to man. Superconducting tunnel junctions, hot electron bolometers and transition edge sensors are some of the most responsive and sensitive sensors working in infrared region.

When first discovered by H. Kamerlingh Onnes in 1911, who was awarded the Nobel prize two years later for his discovery, superconductivity manifested itself as perfect

conductivity in some metals below a critical temperature (Onnes 1911). In 1933, Meissner and Ochsenfeld discovered another signature phenomenon, that of perfect diamagnetism in superconductors, later dubbed as the Meissner effect (Meissner and Ochsenfeld 1933). During the first three quarters of the twentieth century, many metals and their alloys were shown to be superconductive (Bennemann and Ketterson 2008). Until the second half of the 1980's, the highest critical temperature had been observed for Nb_3Ge at around 30K. This was consistent with the limit thought to be indicated by the BCS (Bardeen-Cooper-Schrieffer) theory. Bednorz and Müller's historic paper elevated this limit to 35K for LaBaCuO, a ceramic with CuO layers (Bednorz and Müller 1986). Their work brought them a Nobel prize. This discovery ushered an era of rapid research, both in theoretical and experimental branches. Within a year, Wu, et al. and Chu, et al. (1987) jointly announced the discovery of $YBa_2Cu_3O_{7-\delta}$ (YBCO), another ceramic compound with CuO layers, which showed a critical temperature of 93K. Current record for critical temperature at normal pressures is held by $HgBa_2Ca_2Cu_3O_8$, clocking in at 135K.

Superconductivity is an area of research where the experiments usually come before the theory. In 1934, Gorter and Casimir (Gorter and Casimir 1934) announced their phenomenological model, the "two-fluid model," where they identified two components of the electron "fluid," namely the normal and superconducting fluids. This theory was useful in analyzing the thermal properties of superconductors (Mourachkine 2002). London brothers (London and London 1935) came up with a theory in 1935 explaining the Meissner effect where they combined quantum mechanics with Maxwell's equations by indicating the relationship between the probability density flux in quantum mechanics and charged current density in electromagnetism. Shubnikov, et al. first observed vortices in superconductors in 1937 (Shubnikov et al. 1937). This was an important step in the research on type-II superconductors. These superconductors did not expel the trapped magnetic flux wholly. What Shubnikov and coworkers discovered was the so called "mixed state", or "Shubnikov's phase" which was then a new phase of superconductors. The isotope effect was first observed in 1950 by Maxwell (Maxwell 1950), which hinted at the fact that electron-phonon coupling was behind the phenomenon of superconductivity (Bennemann and Ketterson 2008). In the same year, Vitaly Ginzburg and Lev Landau put forth their thermodynamical theory of superconductors known as the Ginzburg-Landau theory (Ginzburg and Landau 1950). This phenomenological theory successfully

explained the distinction between type-I and type-II superconductors and the existence of the mixed state in the latter type. Abrikosov announced his results in 1957, indicating that the vortices formed a lattice (Abrikosov 1957). This research brought the Nobel prize in 2003 to Abrikosov and Ginzburg, and to Leggett who observed the vortices experimentally. Lev Landau had already earned his Nobel prize in 1969 for related research. The microscopic theory of Bardeen, Cooper and Schrieffer (BCS theory) successfully and fully explained the physics behind type-I superconductors in 1957 (Bardeen, et al. 1957), thereby earning the Nobel prize in 1972. BCS proved, using the machinery of second quantization, that electron-phonon interaction can produce an energy level lower than the Fermi level by an amount on the order of meV and electrons form pairs (called Cooper pairs) via this interaction. Much of the superconducting device physics is based on Cooper-pair tunneling, which was theoretically predicted by B.D. Josephson in 1962 (Josephson 1962). This was one of the few times where theory came before the experiment. The theory brought the Nobel prize to Josephson who shared it with Esaki and Giaever, the latter of whom experimentally observed the Josephson effect one year after the advancement of the theory. This, in broad strikes, was the state of the field up until the discovery of high-T_c ceramic superconductors.

Many models have been advanced since 1987, attempting to explain the microscopic origins of type-II superconductivity. Some of these models are based on experiments that indicate a d-wave symmetry in the superconducting phase, and are variations of Hubbard models. Others are based on solitons. Experiments have shown the presence of two superconducting energy gaps, and models based on this fact also exist. Andersen proposed a model in 1987 suggesting that the pairing of electrons is a different process from the establishment of the macroscopic phase coherence of the superconducting wavefunction (Anderson 1987). Spin excitations were also proposed as being behind the superconductivity in some ceramic superconductors. This is a very active field of research, and many other theories and models exist (Mourachkine 2002), (Bennemann and Ketterson 2008).

Low temperature superconductors are used in several temperature regimes: 10 to 30 K, at liquid helium temperature ($\sim$4K), at 300 mK and at 100 mK. Each of these temperature regions present their own problems in the realization and application of superconductivity. Good, stable cooling technologies, coupled with good vacuum technol-

ogy (usually high or ultrahigh vacuum), are required. This part of the application could easily become prohibitively expensive. In comparison, most high-T_c applications require only LN_2 levels of cooling and rough vacuum is usually enough for the working of these devices.

1.1.2. Low T_c and High T_c Superconductivity

The critical temperatures of the thousands of known superconducting materials range from several millikelvins to 135K (163K under pressure). Since the binding mechanism of Cooper pairs is related to phonons, increased pressure usually leads to higher critical temperatures. From the experimentalist's view, the distinction between low T_c and high T_c superconductors is whether the critical temperature of a material is above or below 30K (Mourachkine 2002). A more physical criterion is to distinguish between the two types of superconductors, type I and type II, delineated by their ability to expel or let pass magnetic flux through their bulk. The thermodynamical theory of Ginzburg and Landau provide the theoretical background for such a distinction.

To advance the discussion on different types of superconductors, one first needs to briefly define and investigate a few key concepts of superconductors, such as the superconducting energy gap (2Δ), the London penetration depth (λ_L) and the coherence length (ξ). However, it should be noted that this thesis does not claim to provide a general review of superconductivity. Only the very basic concepts will be given here. The reader is encouraged to consult some of the many excellent books on superconductivity (Tinkham 1975, van Duzer 1998, Seeber 1998, Bennemann and Ketterson 2008). The discussion in subsection 1.1.2.mostly follows these references except where noted below.

In conventional (type I) superconductors, below a critical temperature and a critical magnetic field, perfect conductivity and perfect diamagnetism is manifested. The electrons form Cooper pairs, which are in the singlet states and act as bosons. The energy level of the Cooper pairs is below the Fermi surface by an amount of 2Δ, where Δ is the the superconducting energy gap. According to London equations, magnetic fields applied on a type-I superconductor only penetrate a certain thickness into the bulk of the superconductor. The magnitude of the magnetic field inside such a superconductors falls to $1/e$ of its value at a distance of λ_L from its surface. If there was any magnetic field inside the bulk of the superconductor material at a temperature higher than its critical

temperature, all of this field would be suddenly expelled as the material is cooled below this temperature. Another important parameter describing the superconducting state is the length scale over which the electrons forming the Cooper pairs can still attractively interact. This length scale is called the *coherence length* and is usually denoted by $\xi(T)$. The temperature dependence of $\xi(T)$ is such that the coherence length goes to zero near the critical temperature. The coherence length also signifies the length scale over which the macroscopic superconducting wavefunction decays in response to an external magnetic field (see figure 1.1.).

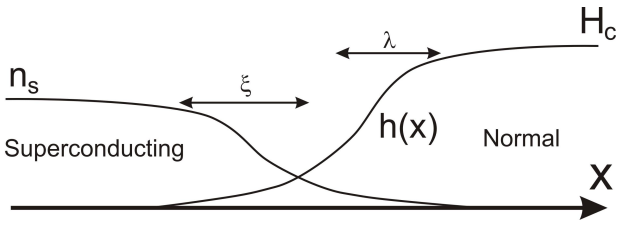

Figure 1.1. The variation of the magnetic field $h(x)$ and coherence length ξ inside a superconductor. As the field drops from its critical value H_c over a characteristic length λ, the number density of Cooper pairs increase over a characteristic length scale of ξ. (Source: Tinkham 1975).

In type-II superconductors, the magnetic field was observed to penetrate the bulk of the material in integer multiples of the *flux quantum* $\Phi_0 = hc/2e = 2.07 \times 10^{-15}$Wb. This goes against what London equations predict. A phenomenological explanation for this behavior came with the Ginzburg-Landau (GL) theory, later amended by Abrikosov to account for the appearance of supercurrent vortices in type-II superconductors. The GL theory builds on the work of Lev Landau on second order transitions. Ginzburg and Landau start by assuming the existence of an order parameter ψ that goes to zero at the transition, as appropriate for the phase transition theory of Landau. This order parameter is later shown to be the macroscopic superconducting wavefunction representing the Bose-Einstein condensate of the superconducting Cooper pairs. They also assume that the free energy of the system may be expanded in powers of this order parameter and the coefficients of the expansion are regular functions of temperature (Saint James and Sarma 1969). Adding the energy per unit volume due to the existence of the magnetic field and the energy due to the supercurrent, the free energy per unit volume becomes

$$F_s = F_n + \alpha|\psi|^2 + \frac{\beta}{2}|\psi|^4 - \frac{1}{2m^*}|\hat{p}_{\text{canonical}}\psi|^2 - \frac{\vec{h}^2}{2\mu_0} \tag{1.1}$$

where F_s and F_n are the free energies corresponding respectively to the superconducting and normal states, α and β are the coefficients of expansion, m^* is the effective mass of the Cooper pairs, $\hat{p}_{\text{canonical}} = -i\hbar\nabla - e\vec{A}$ is the canonical momentum in the presence of a magnetic field and $\overrightarrow{h}$ is the magnetic field strength. Minimizing the integral of this free energy per unit volume in a region where there's a normal-superconductor interface, Ginzburg and Landau found that a parameter $\kappa(T) = \lambda_L(T)/\xi(T)$, later dubbed the Ginzburg-Landau parameter, controls the sign of the free energy of a normal-superconductor interface. Whenever $\kappa < 1/\sqrt{2}$, the interface has a positive energy and is thus thermodynamically unfavorable. Such superconductors are called type-I superconductors. When $\kappa > 1/\sqrt{2}$, the free energy of the interface is negative, thus rendering its presence thermodynamically favorable (Saint James and Sarma 1969). These superconductors are called type-II superconductors. Therefore, for $\kappa > 1/\sqrt{2}$, magnetic fields will penetrate into the superconductors, making some regions of the superconductor normal and creating normal-superconducting interfaces. A more careful analysis shows that filamentary interfaces are more favorable than laminar ones. A filamentary interface, surrounding a flux tube, must carry a supercurrent flowing around in a vortex around the flux tube. Abrikosov (Abrikosov 1957) showed that these vortices form a two dimensional lattice in the superconductor. (He initially predicted a square lattice for the flux tubes, but the correct 2D lattice is the triangular lattice.)

The amount of the flux that can be held in a flux tube is given by the London equations. The order parameter of the GL theory, which turns out to be the macroscopic wavefunction representing the superconducting state, must be single valued. Its phase difference along a path around the flux tube must be an integer multiple of 2π in much the same way as the Aharanov-Bohm effect. This result confines the magnetic flux to an integer multiple of the flux quantum Φ_0. The radii of the vortices are on the order of the coherence length ξ. Moreover, each vortex carries only a single flux quantum due to thermodynamical considerations. Therefore, when a superconducting material under the influence of a magnetic field is cooled down past its critical temperature, as long as the material is wide enough to accommodate the vortices, it will let pass an integer multiple of the flux quantum through its bulk and repel the remainder.

The above discussion assumes perfectly isotropic perfect superconducting crystals. An imperfection in a crystal may force the surrounding area to be a normal (as opposed to superconducting) material. Magnetic flux will penetrate through these defects. These impurities, along with local heating and hot spot formation, will produce some type-II effects on type-I superconductors. Sometimes, especially in bulk materials, the impurities will not be local, forming grains. This will change the behavior of the crystal to one well modeled by a network of Josephson junctions. In type-I superconductors, nonmagnetic impurities have little effect on the critical temperature, while magnetic impurities suppress T_c dramatically (Mourachkine 2002). The impurities also play an important role as *flux pinning centers*, especially in thin films. When supercurrent is forced in a direction perpendicular to the magnetic flux passing through the superconducting material, Lorentz force moves the flux tubes, thus doing work and losing energy. This creates a resistance in the superconductor. It is not easy to push a flux tube off an impurity. If the tube does not move, the Lorentz force does not do work and the sample does not gain resistance.

1.1.3. YBCO as a High T_c Superconductor

While conventional superconductors have relatively simple structures and Fermi surfaces, high T_c materials are usually highly complex and anisotropic. Even the structurally simplest of the high-T_c compounds, such as MgB_2, show a layered structure with a highly complex Fermi surface. $YBa_2Cu_3O_{7-\delta}$ (YBCO) shows high anisotropy and a layered structure. It belongs to a family of perovskite ceramics, with several CuO layers sandwiched in between isolation planes containing rare earth atoms (see figure 1.2.).

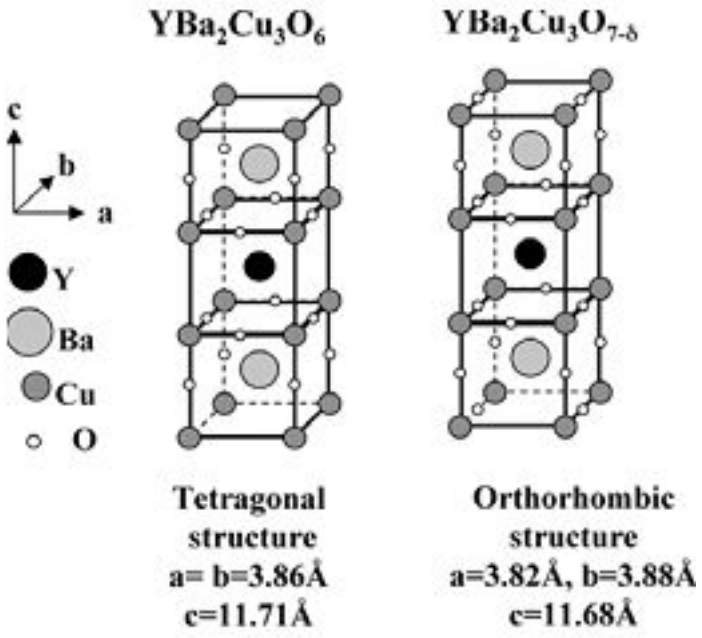

Figure 1.2. The tetragonal and orthorhombic phases of YBCO.

(Source: Ayache 2006)

YBCO has a variable stochiometry and is a doped superconductor. The parent compound, $YBa_2Cu_3O_6$ ($\delta = 1$), is an insulator (Mischke 2003). At all values of δ from 0 to 1, YBCO has two closely separated CuO_2 layers with a distance of 3.2 Å and a Y atom in between these two planes. The next set of CuO_2 planes are 8.2 Å away in the z-direction (see figure) (Burns 1991), separated by BaO planes and Cu-O chains. Each Cu atom in the CuO_2 planes is surrounded by a pyramid of 5 O atoms (Mourachkine 2002). The distance between the Cu and O in these chains shows a slight ab anisotropy and is roughly equal to 1.9 Å. Each Cu As the doping level increases (δ goes from 1 to 0), the structure of YBCO undergoes a phase shift at $\delta = 0.6$ Å from tetragonal to orthorhombic. The doping reversibly adds oxygen atoms to the Cu-O chains. The extra oxygen supplies a hole to the CuO_2 planes. Therefore, the chains act as charge reservoirs for the CuO_2 planes. Superconductivity manifests itself coplanar to these CuO_2 planes as the hole doping increases. While one usually uses the ab-direction for the supercurrent, it is also possible to use the c-direction. The BaO planes between the superconducting CuO_2 planes act as insulators, so the supercurrent in the c-direction can be thought of as passing through a series of Josephson junctions. The phase diagram of YBCO as a function of oxygen doping can be seen in figure (see figure 1.3.). The optimal level of

doping, in terms of higher T_c, is at $\delta = 0.05$.

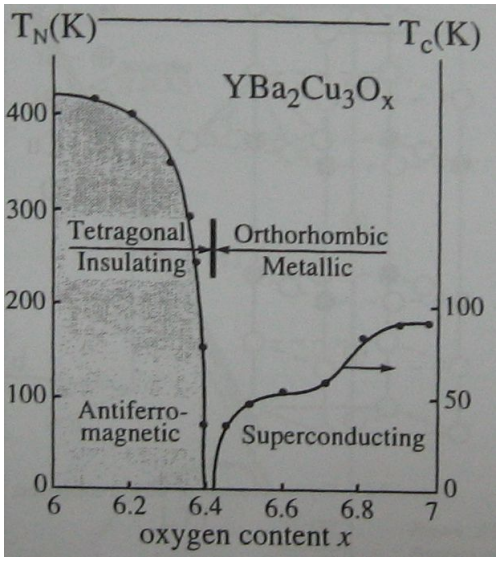

Figure 1.3. The phase diagram of YBCO. (Source: Mourachkine 2002).

It is not too easy to grow bulk single crystal YBCO as the bulk material will have a grainy structure. This structure acts as a network of Josephson junctions (see figures 1.4. and 1.5.). However, single crystal YBCO can be grown epitaxially as a thin film (see section 1.3.1). The thin film growth of YBCO has been extensively studied and it is relatively easy to produce highly c-axis single crystal thin film of YBCO on suitable substrates (see, for example, Norton (1998) or Wördenweber (1999) and references therein).

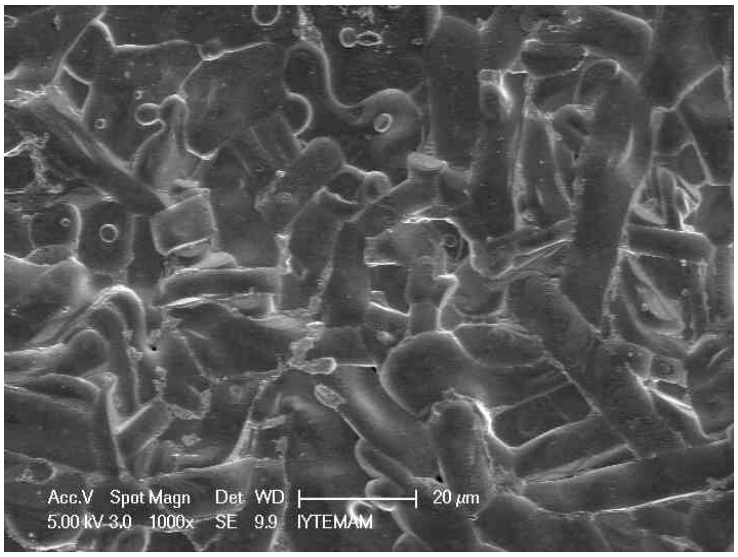

Figure 1.4. Ex-situ annealed bulk YBCO, grown at the Superconductivity Laboratory at the physics department of Ege University, İzmir, Turkey, by Dr. Mustafa Tepe and his student, Ms. Belkis Karci. Note the grains and grain sizes. The SEM picture was taken at IYTE-MAM (Izmir Institute of Technology's Materials Research Center).

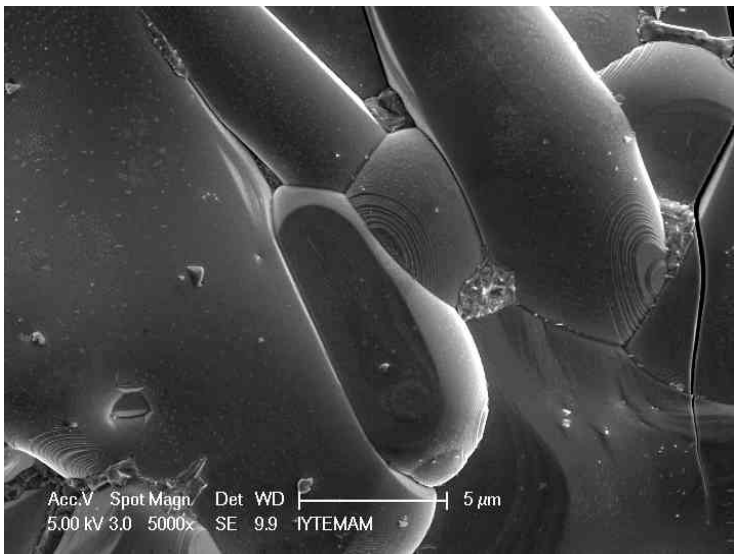

Figure 1.5. The same bulk sample in figure 1.4. with a higher magnification. The SEM picture was taken at IYTE-MAM.

As we will be using epitaxial thin films of YBCO as radiation detectors, it is important to know the absorbance and reflectance of the material as a function of wavelength, as well as the spectral absorption lines. Kakehi, et al. (1998) have investigated

the spectral emission lines of their YBCO thin films. Two infrared radiation ranges of interest in this thesis are wavelengths slightly above 600 nm and slightly above 900 nm, which roughly correspond to the peak wavelengths of the radiation we used to test our devices. In the first range, Y, Ba and especially O radicals have spectral lines, as well as the singly ionized Ba^+ and Cu^+ and molecular YO. Their work also showed the presence of Ar atoms, a residue of the sputtering process, in their spectral lines. In the second range of interest, Kakehi, et al. report no spectral lines. Kelly, et al. (1989) have carried out optical spectroscopy measurements of several high T_c materials in 1989. While this work is limited to the materials known as of 1989, important observations can be made about the optical properties of YBCO based on this paper. The authors report high optical anisotropy in the absorbance of YBCO in the mid-infrared region, but no such anisotropy in near infrared. They show a 20% absorbance within the regions of interest.

1.2. Infrared Detection

In this section, we will start from the basics of infrared radiation detection and make our way towards transition edge bolometers, the kind of infrared radiation detectors which will be the main topic of this thesis. Along the way, we will touch upon the history, uses and realizations of IR detection, followed by specific realizations such as bolometers and calorimeters. Finally we will further specialize towards transition edge sensors.

1.2.1. History and Overview of IR Detection

Infrared radiation was first detected by Herschel in 1800. His method was remarkably similar to current day bolometers in its basic principle: He passed light through a prism to separate it into its colors and put a thermometer where he expected the radiation corresponding to infrared wavelengths would be. Even though no radiation was visible, there was a significant temperature change. Such detectors, which convert incoming light to heat or temperature change are called *thermal detectors* (Vincent 1989). Thermal detectors were the main method of infrared detection up until the second half of the 20th century. Seebeck discovered the thermoelectric effect in 1821 and presented the first thermocouple, leading to a direct temperature-voltage transducer (Rogalski 2002). The first thermopile was produced by Leopoldo Nobili in the early 18th century. Bolometers made

their appearance in 1880, when Langley demonstrated his bolometer, a radiation power to resistance change transducer, made of two thin ribbons of a platinum foil used in a Wheatstone bridge. He kept developing his bolometer until he could thermally sense a cow from almost half a kilometer away (Rogalski 2002).

Photon detectors made their appearance in the early twentieth century. The first IR photoconductor was demonstrated by Case in 1917 (Rogalski 2002). One of the more common photoconductors, lead sulfide, was discovered in 1933. Semiconductor technology took off in the 1950s. In his paper, Norton (Norton 1999) gives the rule of thumb that any physical phenomenon within the energy range of 0.1 eV to 1 eV is a candidate for infrared detection. Other phenomena that fit this rule of thumb and have been successfully adapted as IR detectors include gas expansion (Golay cell), Josephson effect (STJ and SQUID detectors), quantum wells and internal emission (Schottky diodes). Rogalski gives a good summary of the uncooled IR sensors (see figure 1.6.).

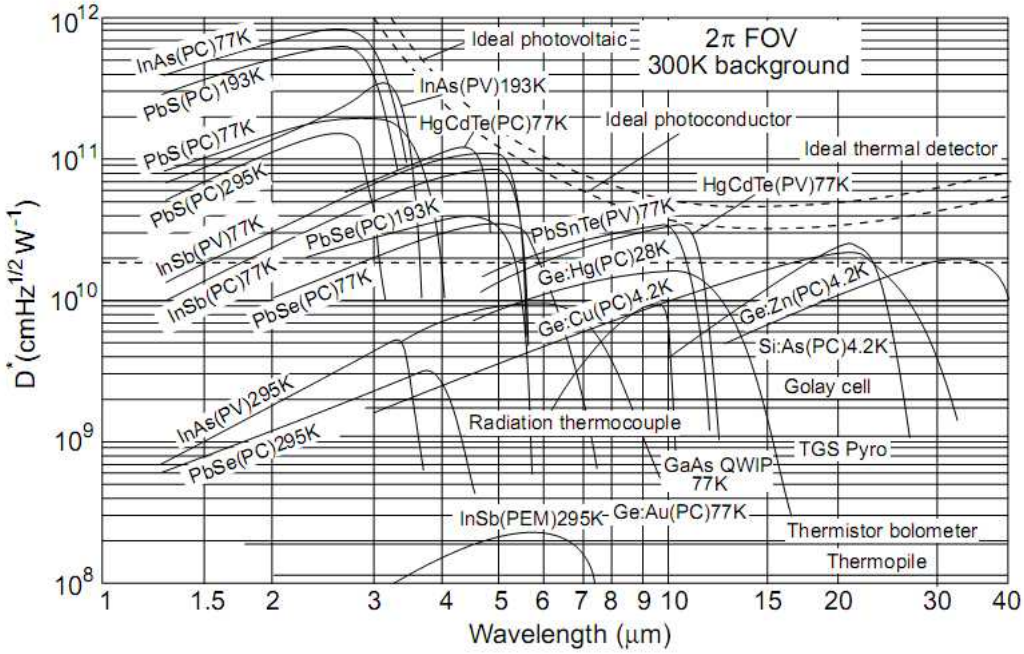

Figure 1.6. Overview of specific detectivities of various infrared detectors as a function of wavelength. (Source: Rogalski 2003)

Until the 1950s, room temperature devices such as Golay cells and thermopiles had advantages over bolometers in their operability or sensitivity. The modern bolometers, competitive with other devices in terms of senstivity, operability and producibility, were first demonstrated by Boyle and Rogers in 1959 (Richards 1994). Their bolome-

ter was operated at liquid helium temperatures. The next important step, as described in P. L. Richards' review of infrared bolometers (Richards 1994), came with the doped germanium resistance thermometer as presented by Low in 1961. First superconducting bolometers were put forth by Goetz in 1939, which Clarke, et al. improved in 1974. Next up was ion implanted Si bolometers as described by Downey, et al. in 1982. This design is still in use for millimeter waves, as it has very low inherent noise. High T_c transition edge bolometers were first analyzed by Hu and Richards (Hu and Richards 1989) and Richards and Verghese demonstrated the first high T_c transition edge superconducting bolometer in 1988 (Richards et al. 1988).

1.2.2. Uses and Realizations of IR Detection

For a layman, the first use that comes to mind for an infrared sensor is probably the military use. Heat of an object can be sensed from very far away, and indeed, lead salt thermal detector technology was developed in the 1950s for anti-air-missile seekers (Rogalski 2003). Room temperature near-infrared sensors based on semiconductor photoconductors are easy to produce and operate. Perhaps the most common solution in the room temperature military use detector is HgCdTe technology, with peak specific detectivities around 10^{11} cmHz$^{1/2}$W^{-1} at 3 μm.

Another security related use of infrared detectors, those of noninvasive scanners which could find use in airport checks, are terahertz detectors. Terahertz frequencies, or submillimeter wavelengths, can be utilized to detect nonmetallic objects that can't be detected by conventional metal detectors. They usually pass through any nonmetallic obstacle of reasonable thickness. They also provide the advantage over x-ray scanning of being harmless. Terahertz detectors would also be appropriate for medical uses, and they are already used widely in astronomy (Winler 2003, Richards 1994, Kreisler and Gaugue 2007, Schlechtweg and Tessmann 2006, Rahman 2006, Rieke 2007). However, in the case of photoconductors and photon counters, the energy of a single terahertz photon corresponds to a few Kelvins. Therefore, these detectors benefit greatly from being operated at low temperatures. However, at the terahertz range, the most competitive detectors are SIS (Josephson junction) mixers and hot electron bolometers. The former is limited by the superconductor energy gap frequency, whereas the latter is limited by quantum noise (Winler 2003). Today, NbN hot electron bolometers and SIS junctions operate in

the terahertz range at only 10 times the quantum limit (Kreisler and Gaugue 2007). Photoconductive devices and depletion zone photodiodes are devices are also widely used in infrared detectors for astronomical research. In his review, Rieke (Rieke 2007) mentions InSb and HgCdTe detectors. High Electron Mobility Transistors (HEMTs) are also mentioned.

Among other realizations are PtSi based Schottky diode detectors with cutoff wavelengths about 6 μm. While they work at about 0.1% of the quantum limit, they can be integrated into arrays to increase their sensitivity. GaAs/AlGaAs quantum well detectors are also in use, operated below LN_2 temperatures with cutoff wavelengths at 20 μm. The growth technology of these films are mature and therefore they can be incorporated easily into large arrays for obtaining images. Figure 1.7. shows the performances of some of these devices (Rogalski 2002).

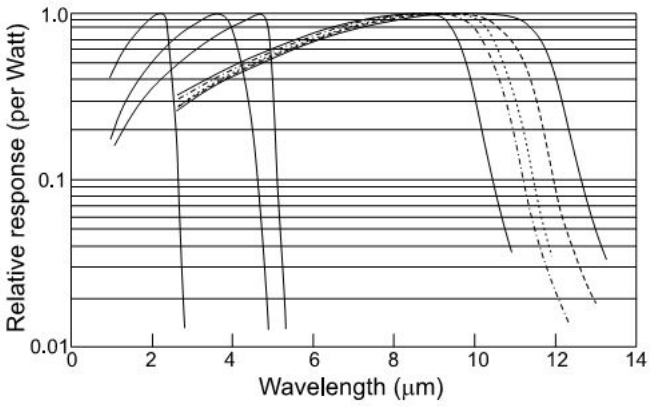

Figure 1.7. Representative normalized detectivities of HgCdTe photodiodes at different temperatures. (Source: Rogalski 2002)

Some applications, including some astronomical research, do not require imaging. They only require the measure of the incoming power or energy. The measurement could be repeated at a different time and position to generate an overall image later. However, some applications, including security applications and some astronomical research, require imaging, i.e. taking data at many different but close points at the same time. This would require thermal detectors built in arrays. Silicon based technology, or other semiconductor technologies, are in the forefront in this area. Not only do we have more mature growth techniques, but also the ambient temperature of the pixels in the device can be slightly different than each other and we would still get the same image. This is not too

easy to achieve with hot electron bolometers and especially transition edge sensors. The stability of the latter is improved by voltage biasing, but this method is usually applied for very small temperatures (300 mK or below) so that the joule heating of the current can stabilize temperature fluctuations (Rieke 2007, Rahman 2006).

1.2.3. Bolometers and Calorimeters

Bolometers and calorimeters are among the oldest realizations of thermal detectors. While their operating principles are simple, a bolometer measures the incoming power whereas the calorimeter measures the integrated energy of the incoming particle or radiation. The most simple bolometer is a thermistor that absorbs radiation which is weakly coupled to a heat bath at a certain temperature (see figure 1.8.). The incoming radiation (or particle flux, for particle detector calorimeters) raises the temperature of the thermistor to a value higher than that of the heat bath. The radiation is then chopped off, allowing the thermistor to cool back to the temperature of the heat bath. The thermistor is usually DC biased by current or voltage, and the change in voltage (for current bias) or current (for voltage bias), is monitored, and converted to a change in resistance. This change can be observed on an oscilloscope, or the process can be repeated continuously and the change can be read off of a lock-in amplifier referenced to the radiation chopper.

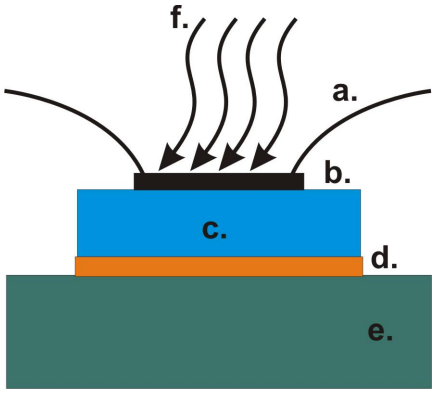

Figure 1.8. Basic thin film bolometer design. Not shown is the radiation coupling mechanism. a. Electrical contacts b. Thin film sensor c. Substrate d. Thermal coupling to the heat bath, usually thermal grease or silver paint e. Heat bath, or cold head for cryogenic applications f. Incoming radiation, although different radiation coupling mechanisms may accept radiation from other directions.

A few points should be noted in reference to bolometers. First, it must be noted

that bolometers measure resistance (or conductance) change as a function of temperature. For one to talk about temperature, there must be a heat bath and a system at equilibrium. Therefore, bolometers must be operated at time constants much larger than the fluctuation time constants. Another point is that the bolometer described above is a *monolithic* bolometer. The radiation absorber can be a separate physical object, coupled strongly thermally to the thermistor. This setup, dubbed a *composite* bolometer, increases responsivity at the possible cost of speed and increased noise by introducing an extra noise source. The radiation absorber structure can be an antenna rather than some material that increases absorptivity. Such bolometers are hard to produce, but they have excellent sensitivities. The third point is saturation. A bolometer with a thermistor having a large thermal mass usually has lower sensitivity and speed, but it can absorb a lot of background radiation before becoming saturated. This is not true for small scale devices, such as microbridge hot electron bolometers or SIS mixers.

Hot electron bolometers (HEBs) are the state of the art in bolometer technology. Semenov, et al. (2002) give an excellent review of the matter up to the year 2002. Kreisler, et al. (2007) describe the efforts toward building better THz detectors, including hot electron bolometers, in Europe up to the year 2007. Cherednichenko, et al. (2000) demonstrate a 600 GHz LO mixer using YBCO hot electron bolometers. HEBs are much faster and more sensitive compared to conventional bolometers because the thermistor component is the conduction electrons (or Cooper pairs and quasiparticles) themselves, with the heat bath being the lattice of the crystal. The thermalization process of the electrons or quasiparticles themselves take nanoseconds to microseconds whereas the thermalization of the lattice takes milliseconds (Zehnder 1995).

Hot electron bolometers and SIS mixers are made of thin films and usually have several microns to submicron dimensions. Quantum dots used as single photon detectors have even smaller dimensions. On the other end of the size scale for bolometers is the astronomical bulk material particle detectors. The CUORICINO bolometers used for the CUORE experiment nearly weigh one ton as an array and are designed to detect double beta decays (Giuliani et al. 2002).

For bolometers operated below liquid helium temperatures, especially for hot electron bolometers operated at millikelvin temperatures, cryogenics and vacuum systems are a real concern. While good and stable cooling systems and cryostats have been developed

operating at those temperatures, the space is usually cramped and the readout electronics need to be set at room temperature. Astronomic research bolometers may be placed in space and one therefore would expect that the ambient temperature of space would be an improvement, but as Yvon, et al. (2008) describe in their amusing paper, things are not as simple as that. (One could argue that things in real life are *never* as simple as that.) Other bolometers may be operated at several kelvins to tens of kelvins (such as some NbN mixers to MgB_2 based bolometers) or at above liquid nitrogen temperatures, such as YBCO bolometers or YBCO hot electron bolometers. These last bolometers have the advantage of easier operability due to easier cooling constraints, but lack the sensitivity of low temperature bolometers.

Not all of the electrical response of a bolometer can be neatly classified into the categories "thermal response" and "noise." In superconductors, flux creep, intrinsic Josephson junctions, phase slip across these junctions can lead to this *nonbolometric response* (Hao et al. 1993, Anderson 1987). Any electrical response that is not due to a shifting of thermal equilibrium, but rather due to nonequilibrium effects, is called nonbolometric response. As bolometers respond to resistance changes as a function of temperature, the derivative of the resistance vs. temperature curve closely follows the amplitude of response versus temperature curve for purely bolometric response. Differences between the curves usually indicate nonbolometric effects. Nonbolometric effects are usually faster, so the measurement must also be made faster to detect nonbolometric effects. Due to this speed, it is sometimes advantageous to try to detect this effect. One must be careful, however, to distinguish these effects from the artifacts rising due to instrumentation (Fardmanesh et al. 1998).

1.2.4. Transition Edge Sensors

Bolometers, as mentioned in section 1.2.3., respond to incoming radiation by changing the temperature of the thermistor absorbing the radiation and reading the resulting temperature change. Therefore, a sharper resistance change for a given amount of temperature variation of the thermistor would lead to higher responsivity. Transition edge sensors are based on this idea. If there's a second order phase change related to the resistance of the material, presumably this would result in a sharp resistance change. (First order phase changes, by definition, do not have temperature changes, and thus cannot be

effective in this sense.) Superconductors have just this type of phase change and therefore are good candidates for such bolometers. However, a bolometer must be operated midway on its transition curve at a point with the sharpest change of its resistance. That is why such bolometers are called *transition edge sensors*.

The response of superconducting transition edge sensors is proportional to the rate of change of resistance as a function of temperature, which in turn is proportional to (among other things) the resistance of the thermistor element at the operating temperature. Therefore, the thermistor must have a sufficiently large resistance in its normal state. What this value should be depends on the application. High operating point resistance induces elevated Johnson noise levels in the device as well as negatively influencing *thermal runaway* (see section 1.3.2). Usually, the desired values of the normal state resistance are achieved in samples with a small cross section. The resistance versus temperature curve must be steep at the transition from superconducting to normal state. This is achieved only in high quality single crystal samples. Moreover, the absorber area must be large enough to cover the irradiated area, but small enough to be formed into pixels. All of these considerations lead to high quality single crystal superconducting thin films shaped with lithography as the subject medium.

Low-T_c transition edge sensors can potentially outperform their high T_c counterparts in nearly every criterion: They have much lower noise equivalent power mostly due to being operated at lower temperatures.They also have higher sensitivities and detectivities. About the only performance criterion that a high T_c transition edge sensor can outperform a low T_c sensor is the saturation level. High T_c sensors typically have orders of magnitude higher saturation levels than their low T_c counterparts. This can be important where the background radiation is high enough that it threatens to saturate the sensor. However, this danger can usually be reduced with appropriate filtering. The real reason for researching and operating high T_c detectors is the ease of use. To operate low T_c detectors, one must go from 10K for niobium bolometers all the way down to hundreds of millikelvins for some low T_c hot electron bolometer applications. Another problem is the temperature stability. Usually the superconducting transition does not happen at the stable temperature of the already expensive and complicated cooling system. One might need to heat the detector a little to get to the transition, and this is hard to maintain at a constant temperature at lower temperatures. On top of all of this, one needs high or

better vacuum to achieve such cooling. Not so with the high temperature superconducting detectors: A simple liquid nitrogen dewar, ket at rough vacuum, combined with judicious heating system is more than enough for a high temperature YBCO thin film transition edge bolometer. As will be discussed in the upcoming sections, the temperature stability of our system was improved from about $\pm 0.2K$ to $\pm 0.002K$ with the judicious use of a piece of ordinary paper (see section 3.1.3.). We have also tested, quite by accident, that a solid blow to the dewar does not degrade the bolometer performance one bit. This would be impossible with, say, a closed cycle helium refrigerator.

1.3. High T_c YBCO Epitaxial Thin Film Transition Edge Bolometers

In this section, we will go over the basic concepts of high T_c YBCO epitaxial thin film transition edge bolometers. We will briefly look into growth and substrate requirements for high quality thin film growth. Thermal parameters critical to the operation of the bolometers are discussed next, followed by the figures of merit for gauging the operation of the bolometer. Geometry of the substrate and the thin film, as well as radiation coupling, is discussed in the following subsection. Finally, we introduce some concepts related to pixel arrays such as thermal crosstalk.

1.3.1. Film Growth

As mentioned in section 1.2.4., good transition edge bolometers need to be made of high quality thin films. Therefore, film growth is a crucial step of building a transition edge sensor. YBCO is a particularly good candidate for this purpose. Its growth mechanisms is well studied and using appropriate substrates, high quality single crystal epitaxial films can be grown. However, best candidates for substrates for film quality are not usually the best candidates from a thermal point of view. Diamond, which is the best thermal candidate, ends up diffusing into YBCO and is volatile at the temperatures required for YBCO growth (600 to 800 ^{o}C). Silicon, which is a very well studied substrate and for which many micromachining techniques are developed, has too high a lattice mismatch to prevent cracking at film thicknesses higher than 50 μm (Brasunas 2003).

For high quality epitaxial film growth on a substrate, a few criteria must be met. One of these is a low lattice mismatch. A good rule of thumb for substrate-film lattice

mismatch is that a mismatch greater than 9% results in a bad film (Ohring 2001). Best substrates for direct film growth of YBCO are strontium titanium oxide ($SrTiO_3$, STO), lanthanum aluminum oxide ($LaAlO_3$, LAO) and magnesium oxide (MgO). Their thermal capacitances and conductances, as well as their lattice mismatch with YBCO, are listed in table 1.1. (Fardmanesh et al. 1998). Sapphire (Al_2O_3) has better thermal quality, but a thin buffer layer (usually CeO) needs to be deposited for good film quality.

Table 1.1. Thermal properties of various materials used as YBCO substrates (Fardmanesh et al. 1998). Sapphire heat capacity at 90K is taken from (Ditmars et al. 1982) and sapphire thermal conductivity is taken from (Berman 1955). (Source: Fardmanesh et al. 1998, Ditmars et al. 1982, Berman 1955)

Substrate	c (J/K cm^3)	k (W/K cm)
MgO	0.53	3
STO	0.43	0.052
LAO	0.59	0.16
Sapphire	0.4	0.4

Another requirement for high quality epitaxial film growth is low chemical activity across the substrate-fim interface. YBCO loses its superconducting quality if it loses too much oxygen. Similarly, carbon and carbon dioxide have been shown to adversely effect YBCO films (Brasunas 2003). YBCO doesn't have too many problems on this count. The substrates that are suitable for YBCO growth usually are chemically inert with respect to YBCO.

Thermally, one usually prefers a thin substrate. Silicon or sapphire works best in these cases, as sapphire can be commercially found at thicknesses of 20 μm and silicon micromachining is a well-developed technique. However, as mentioned above (Brasunas 2003), buffer layers are required to avoid microcracking, and even then, the film thickness at which cracking starts is not high.

As opposed to other high T_c superconductor applications, bolometers are usually operated at currents well below the critical current. Therefore, the presence pinning sites is not a big requirement. In fact, the less impurities present, the better for YBCO transition edge bolometer applications, as to avoid extra noise sources. Therefore, a highly

pure single crystal structure is preferred. Surface quality is also important. Chen, et al. (1997) find that a smoother film leads to better response. Chou, et al. find that surface morphology and precipitates on YBCO thin films have no effect on the absorptivity of YBCO (Chou et al. 1996). They point out, however, that more precipitates in their films, patterned into microbridges, led to smaller heat conductivity and therefore to a poorer bolometer. The electrical properties of the microbridge bolometers of Chou, et al. do not change appreciably as surface morphology changes. This may partly be attributed to the high penetration depth of YBCO at approximately 600 nm (Mourachkine 2002). Superconducting current flows at a skin depth equal to London penetration depth in superconductors, but in our case, the film thickness is much smaller than $2\lambda_L$. Therefore, the faults on the surface ideally form only a small volume of the current flow and have little effect on the noise properties. However, depositing an extra absorber layer on the surface of a superconductor bolometer could lead to a degradation of the superconducting properties (Alain et al. 1997, Brasunas 2003). Moreover, oxygen loss and carbon contamination through the surface also leads to such a degradation. Fardmanesh, et al. (1998) reports that thermal cycling of an unprotected YBCO bolometer in the vacuum environment required for cooling leads to oxygen loss and therefore to a degradation of superconducting properties.

Many growth techniques for high quality epitaxial superconducting thin YBCO films are detailed in literature (Wördenweber 1999, Norton 1998). YBCO thin films grow particularly well using stoichiometric targets using in situ dc magnetron sputtering, but this process requires a stoichiometric target already prepared. The films used in this study were commercially obtained from THEVA GmbH and grown using a proprietary adaptation of thermal evaporation from elemental targets (Prusseit 2000). Their deposition technique is in situ co-evaporation and involves a turntable substrate holder with an oxygen packet. The obtained films are of high quality, as will be discussed in section 3.1.2.

.

1.3.2. Thermal Parameters

We have briefly mentioned in the previous section that the thermal parameters of the substrate must be appropriate for bolometer operation. In this section, we will define these thermal parameters. A conceptual understanding will be aimed at in this

section rather than detailed calculation. Equations will be presented in chapter 2. The parameters defined and used here are those encountered in the literature when discussing infrared detectors. While it would be possible to define and discuss many other important parameters, this section is limited primarily to those used in bolometer literature. It would be useful to keep in mind the basic bolometer diagram in figure 1.8. while going through this section.

One of the most frequently encountered parameters is the *heat capacitance* C. As the bolometers discussed in this thesis is solid state bolometers, the heat capacitance used is the capacitance at a constant volume C_V, though the subscript is usually omitted. Heat capacitance is defined as the amount of heat required to raise the temperature of a substance by one Kelvin. Note that this definition involves the whole substance in question and not a unit volume of the substance. While from a thermodynamics perspective it may be more natural to talk about heat capacity, or heat capacitance per unit volume, the quantities measured in the experiments of bolometers involve total heat capacitance. As such, the volume of the matter involved is the primary contribution to C. For thin films on thinned substrates, the heat capacitance of the film itself may be significant, but for films on thick substrates (many times thicker than the film, usually thicker than 100 μm), the heat capacity of the substrate is the dominant element.

The other most important thermal parameter is *thermal conductance G*. Heat conductance of a substance is defined as the amount of heat transferred from one end of a substance to the other end per second given a 1K temperature difference between the two ends. In the case of thin film superconducting bolometers deposited on a substrate, the thermal conductance across the bulk of the film and the bulk of the substrate is usually higher than thermal conductance across the film-substrate and substrate-cold head boundary. One notable exception is yttria stabilized zirconia (Li et al. 1994). Therefore, the boundary heat resistance (whose inverse is the conductance) is the dominant term. The film-substrate interface thermal resistance is mostly due to Kapitza resistance, modified by the impurities in the film-substrate boundary. Kapitza resistance is the reflection of heat carrying phonons from an interface due to acoustic mode mismatch across said interface. The substrate-cold head interface, when it exists, usually dominates all of these resistances (films can be suspended for increased detectivity and speed, see section 1.3.4.). The substrate-cold head interface is usually a mechanical interface, aided by a ther-

mally conducting adhesive such as silver paint, vacuum grease or commercially available materials such as Apiezon^{TM}N-Grease. No matter how advanced the mounting technique of the substrate onto the cold head is, it would be almost impossible for this resistance to be lower than the interface resistance between the film and the substrate as in the latter case, one crystal directly grows from the other.

While more of an operational parameter, the *chopping frequency* (f) of the bolometer system deserves mention here. Assuming a slowly varying input power, if we allowed the radiation to fall on a bolometer without any breaks, the bolometer temperature would simply settle to a new, higher equilibrium temperature, and therefore to a new, higher resistance. Since the change in resistance is the parameter that is read out, we would end up reading zero output after a while. Therefore, a constant or a slowly varying input radiation power must be chopped at regular intervals. A readout system locked in to the chopping frequency can then measure the proper change in resistance.

Another operational parameter that warrants mention at this point for the easier reading of the rest of this section is the *operating temperature* or *operating point* T_0. As mentioned in section 1.2.4. transition edge sensors are operated at the midpoint of their superconducting transition where their resistance change as a function of temperature is highest. This point can be determined by measuring the $R(T)$ or $A(T)$ curves of the bolometer, where R is the bolometer resistance and A is the response amplitude. Usually the temperature of the heat bath (cold head or cold finger) is the measured quantity as opposed to the temperature of the superconducting film itself. The difference between the temperatures of the film and the cold head can be reduced to the minimum of the temperature increase caused by the bias power and input radiation power. Any temperature difference due to lags as one heats up the system can be reduced if one is willing to do the measurements of $R(T)$ and $A(T)$ slowly enough. Even then, the measured operating temperature T_0 may not be the transition midpoint of the superconducting film. However, assuming that the experimental setup does not change over time, one must work with the measured values.

The *time constant* τ of a bolometer represents how fast it reacts to an input power. When the input radiation power is absorbed, the temperature of the thermistor element raises by ΔT from its equilibrium value. The heat absorbed by the bolometer then diffuses to the cold head, and the bolometer again drops back to its thermal equilibrium

temperature. Using the definitions of heat capacitance and heat conductance above, we can say that as heat capacitance grows (leading to a greater affinity to hold on to heat for a given increase in the temperature), the time constant also grows. Similarly, as the heat conductance increases, the extra heat is removed from the system faster and the time constant therefore decreases.

The *thermal diffusion length* L_f represents how deep a certain amount of temperature difference (which is proportional to input heat) penetrates into the substrate. How fast heat diffuses into the substrate will be governed by the heat conductivity (heat conductance through unit length per unit area) and heat capacity (heat capacitance per unit volume). It will also depend on the rate at which we introduce new wave of input power, i.e. on the chopping frequency. Higher thermal conductivity, lower heat capacity and slower introduction of new input power will all lead to higher thermal diffusion length. This is an important parameter for determining the regime in which the bolometer operates. If the thermal diffusion length is larger than the substrate thickness, we can say that the power introduced by the radiation source has the time to be removed from the system before it is chopped and a new wave of input power falls onto the bolometer. In this regime, the substrate-cold head boundary resistance will dominate the overall heat conductance. This conductance is independent of the chopping frequency. If, on the other hand, L_f is smaller than the substrate thickness, the previous heat wave will not have had the time to leave the substrate before we introduce a new one via the chopper and the thermal conductance G will be dominated by the thermal conductance of the substrate, which scales as $f^{0.5}$ (Fardmanesh et al. 1999).

Effective thermal conductance of a current biased bolometer is its thermal conductivity minus the input power due to joule heating. The overall thermal conductance does not distinguish between the input power, whether it is from the joule heating of the bolometer due to the bias current or from the radiation power absorbed by the bolometer. Therefore, the "thermal conductance channel" will be partly used up by the effort to remove the joule heating to the cold head. The bias current of a bolometer is chosen with this criterion in mind. The larger the bias current, the larger the responsivity, but too large a bias current would block the conductance channel and make it impossible for the bolometer to stay at a stable temperature. This effect is called *thermal runaway*. Richards and Verghese recommend a current bias level so that the power per Kelvin from joule

heating does not exceed 30% of the overall conductance (Richards et al. 1989). Thermal runaway can be prevented by working at lower chopping frequencies, giving the radiation time to move out from the radiation absorber, but this required frequency quickly goes to 0 and the $1/f$ noise grows at the required frequencies (see section 1.3.3.).

1.3.3. Figures of Merit

In this subsection, we will briefly go over the figures of merit for bolometers. As in the previous section, the discussion here will be mostly conceptual and almost no equations will be present. We defer the equations to the following chapter. Specifically, the concepts of responsivity, sensitivity, noise equivalent power, detectivity and saturation will be introduced.

The two most important parameters for quantizing the performance of bolometers are specific detectivity and noise equivalent power. To understand these concepts, one must start with the definition of responsivity. *Responsivity* is defined as the amount of output signal measured per unit input power as radiation. In the case of superconducting transition edge bolometers, one wants to measure the resistance change. This can be done by current biasing the bolometer and reading out the voltage, or voltage biasing the bolometer and reading out the current. In the former case, units of responsivity is [V/W] and in the latter case, [A/W]. Responsivity of a bolometer is related to many parameters. The more effective the power of the incoming radiation may be coupled to the thermistor of the bolometer, the higher the responsivity will be. Similarly, a sharper resistivity change per unit change in the thermistor's temperature will also lead to a higher responsivity. As the bias level increases, so does the measured quantity, up to the point of thermal runaway (see section 1.3.2.). A larger effective conductivity leads to a faster response but a smaller responsivity.

The *noise equivalent power* (NEP) of a detector is defined as the incident power on a detector that would create a response equal to the power of the noise present in the detector per unit square root frequency bandwidth. Another definition is the input power that would generate a signal-to-noise ratio of unity (Dereniak and Boreman 1996, Vincent 1989). Therefore, it is a measure of the required input power so that the output can be distinguished from the noise (although this situation is greatly improved using a phase sensitive device (lock-in amplifier). Possible noise contributions to the noise equivalent

power in high-T_c transition edge bolometers include Johnson noise, phonon noise, flicker (1/f) noise, amplifier noise and background noise (Verghese at al. 1991, Richards et al. 1989, Richards 1994, Brasunas 2003, Khrebtov 1999). The first is due to the resistance of the bolometer and is frequency independent as long as the resistance is frequency independent. The second is the phonon fluctuations across boundaries of substances in thermal equilibrium and its frequency dependence is that of the heat conductance. The physical reason behind 1/f noise is not well understood (Hooge et al. 1981), but its power spectrum goes like 1/f. Amplifier noise is the noise created by the readout amplification, and background noise is the noise due to fluctuations of the incoming radiation. Both of these are white noise. All of these sources are uncorrelated noise sources and therefore their noise equivalent powers add in quadrature. The last two of these noise sources are extrinsic to the bolometer while the first three is intrinsic to it. Further discussion of noise sources in this thesis can be found in section 2.5.

Detectivity (D) is simply the inverse of NEP, while *specific detectivity* (D^*) is defined as detectivity times the square root of the effective area of the radiation absorber. This figure of merit is intended to quantify the smallest signal that can be detected by the detector. Specific detectivity is the more widely used figure, as it removes the bolometer area in question (Brasunas 2003, Vincent 1989, Dereniak and Boreman 1996). NEP increases with the area of the absorber and is therefore not suitable to determine whether a substance would make a good detector component. Specific detectivity solves this problem. Moreover, the specific detectivity of a pixel array is the same as the specific detectivity of a single pixel. D^* can therefore be used to compare two different detector systems no matter what their effective areas are (Mei et al. 1993).

1.3.4. Substrate and Thermistor Geometry

In this subsection, we will first expand upon the discussion about appropriate substrates, started in section 1.3.1.from the point of view of thermal parameters. We will then classify bolometers according to their substrate and superconducting thermistor geometry. We will discuss the advantages and disadvantages of thinned substrates. We will also discuss large area, meander patterned thermistor geometries and compare them with small area, microbridge patterned thermistor geometries. Finally, we will briefly touch upon radiation coupling and absorption schemes.

From a thermal point of view, the substrate of the film should have high Debye temperature to give a lower heat capacity. Low heat capacity increases the speed of the response as discussed in section 1.3.2.. Similarly, a high heat conductance leads to a faster response, but at the expense of responsivity and NEP. A list of various possible substrates for YBCO thin films and their corresponding thermal parameters can be found in table 1.1. . Brasunas and Moseley investigated a meander type composite bolometer on $SrTiO_3$ in 1989 and have found a NEP of 10^{-8} W/Hz$^{0.5}$ (Brasunas et al. 1989). Li, et al. have investigated the speed of response of their thin YBCO film transition edge bolometer for different substrates (Li et al. 1993). Their bolometers are unpatterned 100 by 100 μm devices with 200 nm film thickness on 1 cm by 1 cm by 1mm substrates, illuminated by a 753 nm diode laser and chopped at 100 Hz. The small size of the bolometers compared to the substrate area was intended to make sure that the thermal conductance of the bolometer was equal to the thermal conductance of the substrate (although they would be ignoring the effects of the boundary resistance with this approach). They find that the time constants of their bolometers on Yttria-stabilized-zirconia (YSZ), $SrTiO_3$ (STO), $LaAlO_3$ (LAO) and MgO are 2, 0.25, 0.13 and 0.03 ms respectively. This ordering of the time constants follows the expected values from the heat conductance and capacitance of the substrates.

The overall heat capacitance of a substrate can be decreased and its conductance increased by thinning the substrate. In his review of high temperature superconducting infrared detectors, Brasunas mentions that mechanically thinned 25 μm thick sapphire substrates are commercially available (Lakew et al. 2004). Sapphire also has the advantage of having a high Debye temperature. A CeO or STO buffer layer is necessary for high quality film growth on sapphire. Verghese and Richards opened the route to competitive high-T_c superconducting bolometers (Verghese at al. 1991) . In their paper, they investigate the viability of YBCO bolometer on 20 μm thick sapphire substrate and report a NEP of 2.4×10^{-11} W/Hz$^{0.5}$. Another approach is to suspend these thinned substrates in vacuum as opposed to coupling them directly to the cold head. Brasunas, et al. have investigated such a bolometer and have reported a 65 ms time constant and a detectivity of 6×10^9 cm/Hz$^{0.5}$W^{-1} (Brasunas and Lakew 1994). This bolometer was not monolithic in that it used carbon black as radiation absorption layer. Lakew, et al. have built a monolithic bolometer on 12 μm thin sapphire with CeO buffer layer suspended with kevlar

(Lakew et al. 2004). Their reported time constant is 90 ms and their detectivity values are on the order of 10^{10} cm/Hz$^{0.5}$W^{-1}. This was the state of the art for LN_2-cooled bolometers as of 2004. Khrebtov, et al. compare three types of substrate geometries (Khrebtov 1999). In addition to thick substrate and suspended membrane substrate bolometers, they also consider thick substrates with partially thinned back sides, so that the area behind the superconducting film is thin but the edges of the substrate are thick. This final approach has the advantage of having the high mechanical strength of the thick substrate but the low heat capacity of the thinned substrate. They have used silicon substrates for this application and report time constants on the order of 0.5 ms and detectivities on the order of 10^9 cm/Hz$^{0.5}$W^{-1}.

The geometry of the thin film is also a consideration in bolometer design. One approach is to have large area meanders of the superconductor. There are two advantages to this approach. The large area of the meander helps in radiative coupling. The higher resistance of the meander helps to increase the responsivity. A third and not so obvious advantage is that the meander structure is slightly more resistant to small errors in the patterning process. One disadvantage of the meander type bolometers is increased Johnson noise. The other option is to use a microbridge, which has smaller noise and smaller thermal coupling with the substrate, but radiation coupling is a problem with this type of geometry. A simple radiation absorber layer usually is not enough (but it is still a good idea for meander type bolometers). Dielectric lenses with substrate micromachining and antennas for radiation coupling are required. Such a design was first described by Hu and Richards in 1989, where they estimated a NEP of 2.5×10^{-12} W/Hz$^{0.5}$ (Hu and Richards 1989). It was this paper that put the high-T_c transition edge bolometers on the map, as previous estimates of NEP were not enough to be competitive. Dwir and Pavuna have theoretically and experimentally compared the microbridge pattern to the meander pattern (Dwir and Pavuna 1992) in strong and weak coupling ranges, confirming the considerations presented above. Similarly, Kakehi, et al. have also developed formulations for responsivity for strong and weak thermal coupling to the heat bath (Kakehi 1998) for their microbridge bolometer. They report a responsivity on the order of 10^4 V/W and a NEP on the order of 10^{-14} W/Hz$^{0.5}$.

One other point to keep in mind about microbridge detectors is the formation of hot spots. Hot spots are usually observed in particle detectors or single photon detectors.

They form momentarily when a local variation in temperature, possibly due to an impacting particle, turns a part of the detector from superconducting to normal state. As this could be the main process for detection, this effect could be highly desirable. Sometimes, however, hot spots form from local temperature oscillations and impurities. These hot spots degrade bolometer performance by decreasing responsivity as well as increasing noise.

Radiation absorption and radiation coupling is also an important and sometimes an essential part of bolometer design. Monolithic bolometers, those with no radiation coupling or absorption mechanism, use the thermistor element (the superconductor in our case) as the radiation absorber. The main strength of this approach is its simplicity. No complicated growth, patterning or micromachining is necessary. The faults introduced by these processes (as every extra process has the potential to introduce faults) will be nonexistent. However, the absorption coefficient of YBCO is only 20% at near infrared and drops to 1% at wavelengths of 25μm. Three approaches may be used to overcome this problem. One is a radiation absorber layer, where the incoming radiation is absorbed, causing an increase in the temperature of the absorber layer. This absorber layer would be in contact with the superconducting film, transferring the absorbed radiation to the film as heat. The second approach is to collect the incoming radiation through a dielectric lens. The substrate on which the film is grown, if it can be micromachined and is transparent to the radiation wavelengths of the particular application, is a prime candidate for such a purpose. The third approach is radiation coupling, through light tubes, Winston cavities or antennas (Richards 1994). Each of these approaches have their advantages, disadvantages and areas of application.

A radiation absorber layer has the potential to boost the responsivity of a superconducting transition edge bolometer by a couple orders of magnitude. Common absorbers are a thin layer of resistive metal such as bismuth (Richards 1994, Brasunas et al. 1989), granular Aluminum (Richards 1994), carbon black (Brasunas and Lakew 1994) and gold black (Verghese at al. 1991). Moftakharzadeh, et al. have tried a novel Cu-C absorber for YBCO and report an improvement by 78% in infrared absorption in 10 μm range (Moftakharzadeh et al. 2008). Gold black coating, which seems to be the most popular coating in literature, has an absorptivity in excess of 90% up to 45 μm (Nelms and Dowson 2005). Radiation absorbers also have their disadvantages, of which some can be overcome

by judicious engineering. Carbon diffuses into YBCO and adversely affects its superconducting properties, so either a passivation layer is required on top of YBCO before carbon based absorbers, or the absorber layer must be on the back side of the substrate. The latter solution also neatly solves the problem of degradation of YBCO film during the deposition process of the absorber. However, the speed of the bolometer is adversely affected in this case, as the radiation now has to travel through the absorber-substrate boundary, the bulk of the substrate and the substrate-film boundary. Using thinned substrates is necessary to avoid this problem. Deposition techniques that reduce boundary resistances to the theoretical minimum of Kapitza resistance are also required. Another problem of radiation absorber layers is inhomogeneity. Usually, absorber layers are amorphous rather than crystalline and hence the absorptivity is not uniform throughout the bolometer. This would come into effect for applications that require a spatial resolution of incoming radiation power.

Dielectric lenses, light tubes and antennas are more sophisticated methods to increase the responsivity of the bolometer. Silicon based dielectric lenses are excellent for infrared radiation (Hu and Richards 1989), but it is very hard to grow good quality, microcrack free YBCO on silicon even with a buffer layer. The lens could be separate from the substrate, but then the lens-substrate boundary may reflect the collected light. Light tubes are another approach to collecting radiation (Verghese at al. 1991), but the size and geometry may limit their usability. Planar antennas can be lithographed along with the bolometer for radiation coupling. Bow-tie, log-periodic, and spiral antennas are good candidates for such uses (Richards 1994, Hu and Richards 1989, Goldie et al. 2008). They could be essential to microbridges, whose small areas make them poor radiation absorbers. These antennas are usually broadband. However, due to their size, they are not as appropriate for meander type bolometers as the meander itself could be large enough for the beam diameter of the incoming radiation.

1.3.5. Pixel Arrays

Single pixel transition edge bolometers are used to detect the power level of incoming radiation. A spatial resolution of the radiation power, or imaging, requires an array of pixels. While single pixel YBCO transition edge bolometers have been widely investigated, pixel applications have not yet matured. One of the reasons behind this is

to make sure all of the pixels in an array gives an identical response. While this could be normalized using a computer, keeping the temperature of the pixels the same and reading this temperature is still a problem. Furthermore, each pixel may end up having a slightly different optimum value, and this optimum value may change in time due to thermal cycling or oxygen depletion (Fardmanesh et al. 1998). Johnson, et al. (1993) were able to produce a linear array of nearly identical YBCO meander pixels on silicon. Wentworth (Wentworth and Neikirk 1990) suggests the use of a heater dedicated to each individual pixel, a lookup table for the appropriate heating amounts and a mux matrix for the heaters. One field of study that we think is promising is combining this idea with the work of Lesquey, et al. (1995) where they use YBCO microbridges as low noise temperature regulators.

Even if one manages to get every pixel to behave the same way, readout and thermal crosstalk are still big problems (Gaugue et al. 2001). The former would require designing and implementing readout contact lines connected to a mux for scanning the pixels. One difficulty is that superconducting films are not amenable to multilayer processing. The latter, however, is an important problem. *Thermal crosstalk* is due to the lateral flow of heat through the substrate, resulting in illuminated pixel heating up other pixels. These unilluminated but heated pixels respond almost identically as the illuminated pixels. This effect, rather than the optical diffractive resolution, limits the imaging resolution of transition edge pixel arrays (Delerue et al. 2003). Bozbey, et al. proposed an ingenious method to use this effect to advantage (Bozbey et al. 2006). They used the phase of the response of thermally activated but unilluminated pixel as a contact free readout device for the illuminated pixel.

High T_c Superconducting transition edge bolometer pixels are usually formed into a *staring array* (*focal plane array*). In this configuration, an array of stationary pixels are positioned at the focal point of a light gathering optics and the response of each pixel is individually measured. It would be impractical to do this measurement simultaneously, so the pixels are scanned using a mux. Due to the difficulty in growing multilayer films, the geometry and number of pixels is limited. While other configurations, such as a single pixel scanning imager, is possible, the space and number of feedthroughs of the cryogenic devices in which the bolometer must be mounted limit the realization of such devices.

CHAPTER 2

MODELS FOR SUPERCONDUCTING YBCO BOLOMETERS

This chapter will attempt to quantify the concepts discussed in the previous chapter. As such, for most of the conceptual discussions, the reader is referred to chapter 1. This chapter will have more equations than verbose discussion.

The basic bolometer equations, and their frequency dependence details, will be discussed in section 2.1. The RC model of a transition edge bolometer will be introduced in the same section. Another approach in obtaining the same equations will be presented in the next section. This approach, the *control theory* formalism, has the advantage of being easily expendable to more complicated systems. In section 2.3, the flow of heat through the bolometer will be investigated via the heat equation. this will lead to the next section, which is on interpixel crosstalk due to heat diffusion from one pixel to the next. Finally, models and equations for the noise sources described in section 1.3.3. will be presented.

2.1. Basic Bolometer Equations and The RC Model

The basic bolometric equation starts from Ohm's law and conservation of energy. For a current biased bolometer, the response amplitude is the voltage change due to a constant bias current and changing resistance as a function of temperature.

$$\begin{aligned} \Delta V &= I_b \Delta R \\ &= I_b \frac{dR(T)}{dT} \delta T \end{aligned} \tag{2.1}$$

The change in temperature due to the incoming radiation, δT, can be obtained using energy conservation, where we equate input power into the bolometer to the power stored plus power transmitted to the cold head:

$$\eta P(\omega) + I_b^2 R(T) = G\delta T + C\frac{d(\delta T)}{dt} \tag{2.2}$$

where $P(\omega)$ is the input radiation power, $\eta = P_{\text{absorbed}}/P_{\text{input}}$ is the absorption coefficient, ω is the modulation (chopping) frequency of the input radiative power, I_b is the bias current, $R(T)$ is the temperature dependent resistance, G is the overall thermal conductance of the system, C is the overall heat capacitance, δT is the temperature rise of the thermistor with respect to the cold head. Let us first investigate the case with no power input:

$$\begin{aligned} G\delta T + C\frac{d(\delta T)}{dt} &= 0 \\ \Rightarrow \qquad \delta T &= \delta T_0 e^{-\frac{t}{C/G}} \end{aligned} \tag{2.3}$$

The solution indicates that an initial temperature rise decays with a time constant $\tau = C/G$. This result was hinted at in the section 1.3.2. Next, let us add in the radiative power with a time dependence $P(t) = P_0 e^{i\omega t}$. We end up with equation 2.2 without the second term.

$$\begin{aligned} \eta P(\omega) &= G\delta T + C\frac{d(\delta T)}{dt} \\ \delta T &= \frac{\eta P_0}{G + i\omega C} \end{aligned} \tag{2.4}$$

Finally, we add the Joule heating. We rewrite equation 2.2 with the Joule heating term as a function of δT, in effect retaining only the AC terms.

$$\begin{aligned} \eta P(\omega) + I_b^2 \frac{dR}{dT}\delta T &= G\delta T + C\frac{d(\delta T)}{dt} \\ \Rightarrow \qquad \eta P(\omega) &= \left(G - I_b^2 \frac{dR}{dT}\right)\delta T + C\frac{d(\delta T)}{dt} \\ \Rightarrow \qquad \eta P(\omega) &= G_{\text{eff}}\delta T + C\frac{d(\delta T)}{dt} \\ \Rightarrow \qquad \delta T &= \frac{\eta P_0}{G_{\text{eff}} + i\omega C} \end{aligned} \tag{2.5}$$

where $G_{\text{eff}} = G - I_b^2 \frac{dR}{dT}$ is the *effective conductance* mentioned in section 1.3.2. We sub-

stitute our result back into equation 2.1 to obtain

$$\begin{aligned} \Delta V &= I_b \frac{dR(T)}{dT}\,\delta T \\ &= \frac{\eta P_0 I_b \frac{dR(T)}{dT}}{G_{\text{eff}} + i\omega C} \\ \Rightarrow \mathcal{R}(\omega) &= \frac{\eta I_b R \alpha}{G_{\text{eff}}\,(1 + i\omega\tau)} \end{aligned} \tag{2.6}$$

In the above equation, $\mathcal{R}(\omega) = \frac{\Delta V}{P_0}$ is *the frequency dependent responsivity* and $\alpha = \frac{1}{R}\frac{dR}{dT}$ is *the temperature coefficient of resistance*. We can discern the amplitude and the phase of the response from equation 2.6:

$$\begin{aligned} |\mathcal{R}(\omega)| &= \frac{\eta I_b R \alpha}{G_{\text{eff}}\sqrt{1 + (\omega\tau)^2}} \\ \tan(\theta) &= -\frac{\omega C}{G_{\text{eff}}} \end{aligned} \tag{2.7}$$

Equation 2.6 is sometimes called *basic bolometer equation*. It leaves some questions open to discussion. In the multilayered structure of thin film transition edge bolometers, which conductance are we talking about? Which heat capacitance is used in the equation?

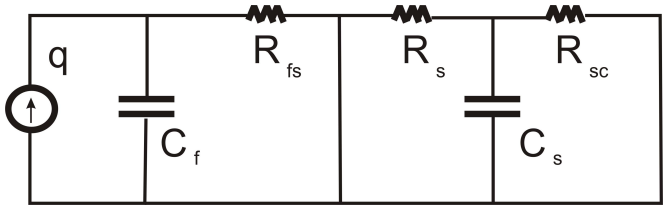

Figure 2.1. Electrical circuit analogy of a bolometer. q is the input heat per second, R_{fs}, R_s and R_{sc} are the film-substrate, substrate and cold head-substrate thermal resistances and C_f and C_s are the film and substrate heat capacitances.

The answer to these questions come from the RC model. In this model, the flow of heat from the thermistor to the heat bath is compared to an electrical circuit (Fardmanesh 2001) (see figure 2.1.). The input radiative power is considered to be the current source in this analogy. The elements of the bolometer, in a direction from the radiation absorber

to the heat bath in figure 1.8., make up the circuit elements. Each element is represented by one capacitance (its total heat capacitance) and one resistance, which is the inverse of the heat conductance inside that element. Each boundary between elements is also represented by a resistance, which corresponds to the inverse of the heat conductance across the boundary (usually Kapitza resistance). For a large element (such as the substrate), a series of resistances and capacitances corresponding to infinitesimal slices perpendicular to the direction of heat flow from the thin film to the heat bath may be considered (Fardmanesh 2001). In this thesis, we will consider all such elements to have a single lumped resistance and capacitance, and the boundaries to have a single resistance. Some approximations can be made in this picture. The heat capacitance and conductance of the thin film, due to the film's relatively small size, may be ignored. Usually, the thermal resistance (inverse of thermal conductance) across the film-substrate boundary can also be ignored. While there's some acoustic mismatch between the film and substrate, a good quality single crystal film will be the continuation (either with a rotation or some skipping, or with some stress) of the substrate's lattice, and only a discrete set of phonon modes (or narrow bands of phonon modes, in the case of stress) will be reflected back. Comparing this to the bulk heat resistance of the substrate, and that to the heat resistance from the substrate to the cold head (where we do not have the advantage of matching lattices), we can safely ignore the boundary resistance of the film-substrate interface. One other argument in favor of this is the penetration depth of the radiation into the film. The radiation may penetrate quite far into the film before it is absorbed. This length is comparable to the London penetration depth, and that is usually within one order of magnitude of the thickness of a YBCO thin film.

If the boundary resistance between the substrate and the cold head comes into play, then it is the dominating resistance. When does it come into play? To answer that, we need to look into the frequency dependence of the heat flow into the substrate. The starting point of this discussion is the heat equation:

$$D\nabla^2 T = \frac{\partial T}{\partial t} \tag{2.8}$$

Our discussion from here on follows almost exactly that of Fardmanesh, et al. (1995). Solving the heat equation in one dimension (perpendicular to the cold head contact sur-

face), where x is the distance into the substrate from the thermistor ($x = 0$ is the film-substrate boundary and $x = L$ is the substrate-cold head boundary), one gets

$$T(x,t) = T_0 e^{-\sqrt{\omega/D}}\, e^{-i\omega t} \tag{2.9}$$

where the diffusivity $D = k_s/c_s$ of the substrate is the ratio of the thermal conductivity k_s (*not* conductance) and heat capacity c_s (*not* capacitance) of the substrate. Equation 2.9 suggests the definition of a characteristic length L, dubbed *the thermal diffusion length*, as follows:

$$L = \sqrt{\frac{2D}{\omega}} \tag{2.10}$$

Using this as the penetration depth of the thermal wave into the substrate and from the definition of thermal conductivity and heat capacity, we have

$$\begin{aligned} G_s &= a k_s \frac{A}{L} \\ C_s &= b c_s A L \end{aligned} \tag{2.11}$$

where A is the relevant cross sectional area of the substrate (usually the one directly under the thin film thermistor). Fardmanesh, et al. introduce the constants a and b to account for geometrical factors.Using the above equation with the definition of the time constant and equation 2.10, we get

$$\begin{aligned} G_s &= aA\sqrt{c_s k_s \omega/2} \\ C_s &= bA\sqrt{2c_s k_s/\omega} \end{aligned} \tag{2.12}$$

At this point, let us consider the magnitude of the responsivity from equation 2.7. Under the square root in the denominator, we have $\left(1 + (\tau\omega)^2\right)$. Again, in the denominator, we have the heat conductance. Considering equation 2.10, at low frequencies, the heat

wave will reach the substrate-cold head boundary. When this boundary comes into play, its thermal resistance dominates that of the substrate, and we use a frequency independent conductance in our equations. Considering the definition of $\tau = C/G$, this situation leads to a $1/f$ dependence of the overall responsivity. On the other hand, when the chopping frequency is high enough, the heat wave does not reach the substrate-cold head boundary and we use the thermal conductance in equation 2.12. As a result, we end up with an overall $1/\sqrt{f}$ dependence of the responsivity. The frequency where we have a transition from one regime to the other, where the thermal diffusion length is comparable to the thickness of the substrate, is called the *knee frequency*.

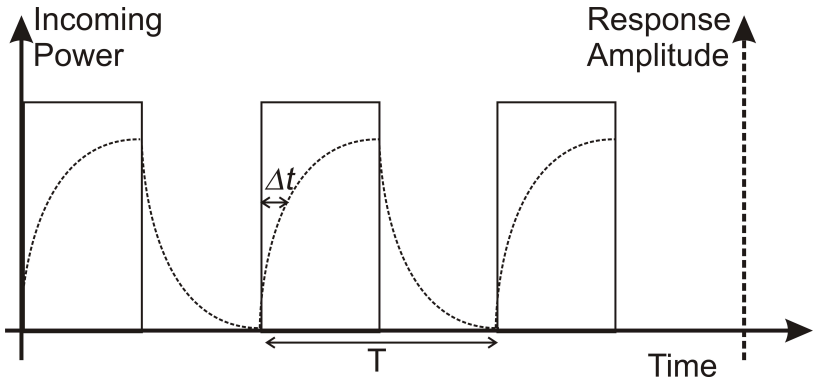

Figure 2.2. The schematic that represents the phase of response and its origins. The horizontal axis is time and the vertical axis is response. The square wave is the input heat power, whereas the dotted line represents the temperature rise in the film. The phase of response, $\phi = 2\pi\Delta t/T$, is proportional to the lag of response, Δt.

A few words about the phase of response need to be spoken here. The phase of response, as defined in equation 2.7, originates from the thermal inertia of the bolometer system. When light is shined on the bolometer, the system takes time to heat up. Similarly, when the light is chopped, it takes time to cool down. As indicated by equation 2.7, larger capacitance and smaller conductance would lead to greater inertia. This effect can also be seen in figure 2.2..

2.2. Feedback and Control Theory Model

In this section, we will briefly touch upon the derivation of the equations using the tools provided by control theory. This section is included for the sake of completeness,

and for the reason that the tools of control theory can be used to expand the derivations of the previous section to arbitrarily complex devices with relative ease. The elegance of the solution was also instrumental in the author's choice to include this method here. An example of such complex modeling can be found in Appel's review of the material (Appel and Galeazzi 2006). The experimental part of this thesis does not need this section, so the reader will be referred to an excellent review of control theory in general by Bechhoefer (Bechhoefer 2005).

In control theory, most of the calculations are done in the frequency domain and by block diagram algebra. An input function $u_i(\omega)$ is transferred to an output function $u_o(\omega) = H(\omega)\,u_i(\omega)$ by a transfer function $H(\omega)$ (see figures 2.3. and 2.4.). Some common block diagram operations are reproduced here from Galeazzi, et al. (2003) (see figure 2.5.). One starts by converting the equations of motion to the frequency domain, writes out the diagram structure for the equation, and then reduces this (possibly complicated) structure to a single transfer diagram. Control theory is particularly useful in working with equations with feedback.

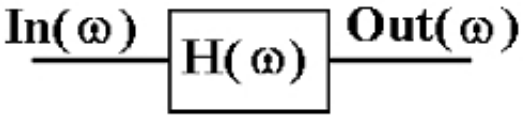

Figure 2.3. The basic block diagram.
(Source: Galeazzi and McCammon 2003)

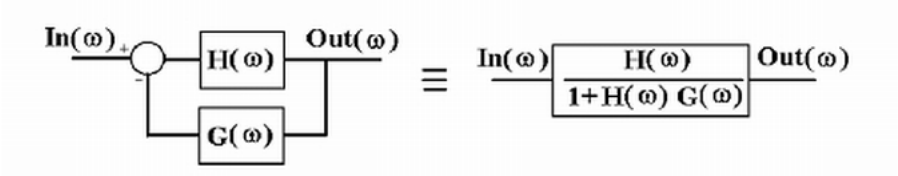

Figure 2.4. The feedback loop operation.
(Source: Galeazzi and McCammon 2003)

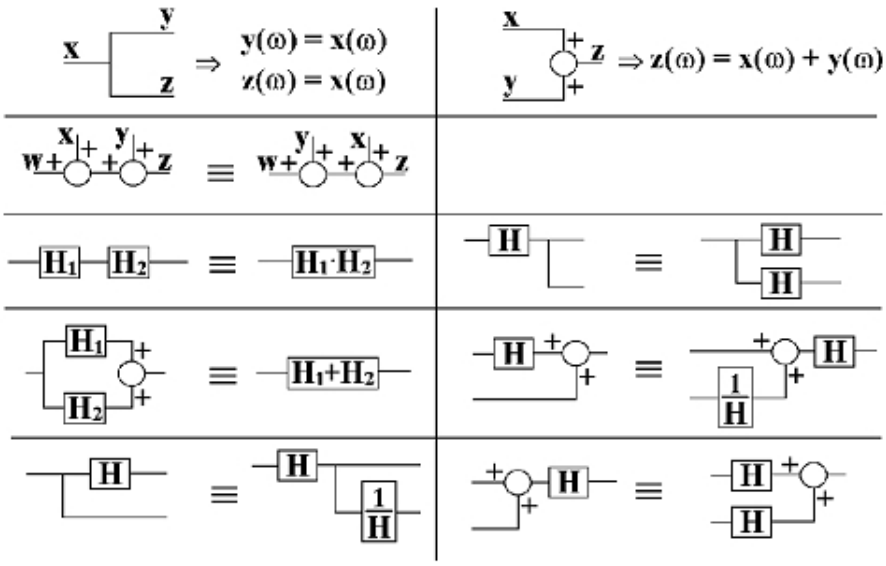

Figure 2.5. Commonly used block diagram operations.

(Source: Galeazzi and McCammon 2003)

Consider the first line of the equation 2.5, reproduced below:

$$\begin{aligned} \eta P(t) + I_b^2 \frac{dR}{dT}\delta T &= G\delta T + C\frac{d(\delta T)}{dt} \\ \Rightarrow \quad \eta P(t) + G_{\text{feedback}}\delta T &= G\delta T + C\frac{d(\delta T)}{dt} \\ \Rightarrow \quad P(\omega) + G_{\text{feedback}}\delta T &= G\delta T + i\omega C\delta T \end{aligned} \tag{2.13}$$

where the last line is in the frequency domain. This can be considered as a system with an input power that generates the output of δT. Through electrothermal feedback, the total input power depends on the output, and we have a feedback system. The right side has the lowpass transfer function (Galeazzi and McCammon 2003)

$$H(\omega) = \frac{1}{G(1 + i\omega\tau)} \tag{2.14}$$

as the feedback is simply a multiplication by G_{feedback}, one can write this system as in the block diagram in figure 2.4. (Galeazzi and McCammon 2003), which reduces the transfer function to the following equation:

$$
\begin{aligned}
H'(\omega) &= \frac{H(\omega)}{1+H(\omega)(-G(\omega))} \\
&= \frac{1}{G(1+i\omega\tau)} \cdot \frac{1}{1+\frac{1}{G(1+i\omega\tau)} \cdot (-G_{\text{feedback}})} \\
&= \frac{1}{(G-G_{\text{feedback}})(1+i\omega\tau)}
\end{aligned}
\tag{2.15}
$$

which is a familiar solution.

More complicated systems, such as hot electron bolometers, can be investigated using this method. In hot electron bolometers, two weak thermal links exist instead of one: That between the electronic system of the superconductor and the lattice of the superconductor, and the substrate-cold head boundary. The electronic system has also its own heat capacitance. Nevertheless, the heat is deposited into the lattice of the superconductor and moves both 'toward' the electronic system and the cold head. This complicated structure can be solved with the tools of control theory surprisingly easily (Galeazzi and McCammon 2003, Appel and Galeazzi 2006).

2.3. Heat Flow model

In this section, we will briefly outline some of the results in literature which solved the heat equation. This step is not necessary in dealing with a single pixel, but when dealing with several pixels and the thermal crosstalk between them, the solutions of the heat equation come in handy. We have already considered a simple case with no lateral heat flow in equation 2.9.

We will start by outlining the work of Aboudihab, et al. (1994) and Tyutyundzhiev (Tyutyundzhiev 1994). They both work with the assumption that the substrate is semi infinite (i.e. it starts at the film-substrate boundary and has infinite thickness). This assumption is valid when the thermal dissusion length is shorter than the thickness of the substrate. At this point, Tyutyundzhiev, ignoring lateral heat conduction, writes down the boundary conditions. He lets the incoming radiative power equal the heat flow at the surface of the film, and formulates that the incoming heat is the same as the outgoing heat at other boundaries of the system. Finally, he lets the temperature of the substrate at the substrate-cold head interface to be equal to that of the cold head. He then obtains the

following for the temperature of the superconducting film:

$$T_f = \frac{\eta P}{(1+i)k_f\sqrt{\omega/2D_f}}\, e^{-(1-i)\sqrt{\omega/2D_f}x} e^{i\omega t}$$

$$T_s = \frac{k_f\sqrt{\omega/2D_f}}{k_s\sqrt{\omega/2D_s}} \cdot \frac{\eta P}{(1+i)k_f\sqrt{\omega/2D_f}}$$

$$\times \qquad e^{-(1-i)\sqrt{\omega/2D_f}d_f}\; e^{-(1-i)\sqrt{\omega/2D_s}x} e^{i\omega t} \tag{2.16}$$

where k_f and k_s are the thermal conductivities of the film and the substrate respectively and d_f is the film thickness. This result ignores the thermal resistance between the film and the substrate. If this assumption is invalid, one then must formulate the same problem with multiple internal reflections of the heat, which bounces back from the boundary back into the film. Tyutyundzhiev argues that this situation resembles the Fresnel equations and this problem can be solved using appropriate boundary conditions.

Aboudihab, et al. (1994) mention that working with only one dimensional heat flow is unphysical. For a constant radiative input power, they find that the temperature rise at the top of the substrate is

$$\Delta T = \frac{2P}{A}\sqrt{\frac{t}{Gc\rho}}\, i\mathrm{erfc}\left(\frac{z}{2\sqrt{kt}}\right) \tag{2.17}$$

where z is the coordinate perpendicular to the substrate surface and is 0 at the film-substrate interface and A is the area of the bolometer. This result is clearly unphysical as the temperature would continue to rise indefinitely. Under the same conditions but this time considering the lateral diffusion of heat by solving the same equation in cylindrical coordinates, they get

$$\Delta T = \frac{2P}{A}\sqrt{\frac{t}{Gc\rho}}\left[i\mathrm{erfc}\left(\frac{z}{2\sqrt{kt}}\right) - i\mathrm{erfc}\left(\frac{\sqrt{z^2+a^2}}{2\sqrt{kt}}\right)\right] \tag{2.18}$$

where a is the radius of the region of interest, usually the incoming radiation radius. This

leads to a maximum temperature difference at the film-substrate interface of

$$\Delta T_m = \frac{\eta P}{\pi a D_s} \tag{2.19}$$

Gaugue, et al. (2001) also solve the heat equation in a detailed manner. They sliced the bolometer into its layers and carefully wrote down the boundary conditions in 2D. They the utilize Laplace transform to solve the problem. They also use a numerical method to solve their final equations, this time for two adjacent meander shapes in 3D. Comparing their results with experiment, they conclude that the illuminated pixel is well described by the 2D model, but the 2D analytical model is insufficient to explain the response of the unilluminated pixel. One therefore has to use a 3D numerical method to fully work out pixel crosstalk.

2.4. Pixel Crosstalk

Pixel crosstalk, as mentioned in section 1.3.5, is the primary limitation for the spatial resolution of images in a transition edge sensor array. It is due to the lateral diffusion of heat from one pixel to the other. Surface micromachining may be necessary to reduce or remove the effects of crosstalk (Hilton et al. 2003). Crosstalk is quantified as the ratio of the responsivities of two pixels when only one is illuminated:

$$C_{12} = \frac{\mathcal{R}_{V1}}{\mathcal{R}_{V2}} \tag{2.20}$$

where $\mathcal{R}_{V1}$ is the optical voltage responsivity of the unilluminated pixel and $\mathcal{R}_{V2}$ is the optical voltage responsivity of the illuminated pixel. Delerue, et al. (2003) have similar setups and chip dimensions to ours and have found the C_{12} to be on the order of -30dB. In their setup, this corresponded to one millimeter (as measured by the beam position on the pixels) for their spatial resolution. They also report that the crosstalk figure decreases until an optimum modulation frequency and then increases. As mentioned in the previous section, Gaugue, et al. (2001) note that a detailed calculation is needed to fully model thermal crosstalk.

Bozbey, et al., considering simple 1-D heat flow from one pixel to the next on the substrate surface, obtain a simpler result for thermal crosstalk (Bozbey et al. 2006). They find that the temperature of the unilluminated pixel which is a distance x from the illuminated pixel is

$$T(x,\omega) = T_0 e^{\left(-\sqrt{\frac{\omega}{2D}}x\right)} e^{\left(-i\sqrt{\frac{\omega}{2D}}x\right)} \tag{2.21}$$

where T_0 is the temperature of the pixel without crosstalk and D is the thermal diffusivity of the substrate. They use the phase information to superpose two different crosstalk signals from two illuminated pixels and read out the input from the unilluminated signal. This would remove the extra complications of electrical contacts on pixels to be read out. We used this equation for obtaining quantitative crosstalk data.

2.5. Noise in High T_c Epitaxial Thin Film Superconducting YBCO TEBs

Noise in any kind of detector is quantified by the autocorrelation function of the ac-coupled quantity whose noise is to be measured. For convenience, we will assume that what we're measuring is already ac-coupled. A general argument for the autocorrelation function being the measure of noise is that autocorrelation function measures how a quantity is related to the same quantity a certain time interval later. If there's little relation, then the autocorrelation function tends to zero. except for zero time interval.

Assume that we're measuring voltage, $v(t)$. The autocorrelation function is given by (Dereniak and Boreman 1996)

$$\Re(\tau) = \int_{-\infty}^{\infty} dt\, v^*(t) v(t+\tau) \tag{2.22}$$

The above equation may be weighted with an appropriate probability distribution. Note that it is written for a complex quantity; for real valued functions, the asterisk may be ignored. Wiener-Khintchine theorem states that the power spectral density of these fluctuations is given by the Fourier transform of the autocorrelation function:

$$\mathfrak{S}(\omega) = \int_{-\infty}^{\infty} d\tau e^{i\omega\tau} \mathfrak{R}(\tau) \tag{2.23}$$

As the power of each of the ω components add, voltage noises add in quadrature (Dereniak and Boreman 1996). If the power spectral density of a kind of noise is flat, it is called *white noise*. Other than white noise, $1/f$ noise is common in superconducting transition edge sensors. The name is due to $\mathfrak{S}(\omega)$ having a $1/\omega$ ($1/f$) dependence.

Various types of noises have various statistical distribution properties. *Poisson noise* has the property that its standard deviation is equal to its average. This noise type usually comes up when dealing with discrete events. Shot noise, generation-recombination and photon noise are some examples of Poisson noise (photon noise does show a slight difference). Bose-Einstein noise is usually seen in bosons being emitted in numbers, such as thermal background noise.

In the upcoming subsections of this chapter, we will look into the equations of important noise sources in bolometers. We divide the discussion into four parts. Intrinsic noise sources are due to the detector chip itself, and only changing chip design or growth techniques may improve these kinds of noise. The second section deals briefly with the noise introduced by the readout circuitry itself. The third section is the noise in instrumentation, such as the chopper frequency fluctuations. Buying better equipment usually decreases this kind of noise by virtue of having thrown money at the problem. Finally, background noise (noise from external sources) will be discussed. It should be noted that the NEPs of all of these noises add in quadrature as they are uncorrelated.

2.5.1. Intrinsic Noise Sources

The first intrinsic noise we'll discuss is the Johnson noise or Nyquist noise. It is white noise. To derive its NEP form, consider a resistor in parallel with a capacitor. The derivation here follows Dereniak (Dereniak and Boreman 1996). Let the average value of the voltage fluctuations on the resistor be $< v >$. Then, the average energy stored in the capacitor will be $1/2C < v >^2$. Using the equipartition theorem, we have

$$\frac{1}{2}C\langle v\rangle^2 = \frac{1}{2}kT$$
$$\Rightarrow \qquad \langle v\rangle^2 = \frac{kT}{C} \tag{2.24}$$

A short time τ later, the voltage across the capacitor decays exponentially. Therefore, $v(t+\tau) = v(t)e^{-\tau/RC}$. This implies:

$$\begin{aligned}
\mathfrak{R}(\tau) &= \langle v(t)\rangle\langle v(t+\tau)\rangle \\
&= \langle v^2\rangle\, e^{-\tau/RC} \\
\Rightarrow \qquad \mathfrak{S}(\omega) &= 4\int_0^\infty d\tau \mathfrak{R}(\tau)\cos\omega\tau \\
&= 4\langle v^2\rangle RC \\
&= 4kTR
\end{aligned} \tag{2.25}$$

Considering the definition of power spectral density of voltage noise as square voltage fluctuations per bandwidth, and the definition of responsivity, we obtain for the Johnson NEP

$$NEP_R^2 = \frac{4kTR}{|\mathcal{R}|^2} \tag{2.26}$$

Next is the phonon noise. This is the thermal fluctuation noise across a thermal barrier. When two objects are in thermal equilibrium, heat (and therefore phonons) are constantly exchanged across their boundary. Momentarily, one side may be getting more phonons than it gives. The NEP calculation is exactly the same as Johnson noise, with the resistance replaced by the inverse of thermal conductance and the capacitance replaced by heat capacitance. Therefore, the NEP for phonon noise is

$$NEP_{ph}^2 = 4kT^2G \tag{2.27}$$

The responsivity in the denominator is replaced by the temperature in the numerator be-

cause of the definitions of the parameters involved.

The last type of noise we'll discuss as intrinsic is the $1/f$ noise. The microscopic origins of this noise is unknown, as discussed in section 1.3.3. The paper by Hooge, et al. (1981) is considered to be definitive, but even there, the authors have been careful to state that their results are experimental and empirical. In 1969, Hooge proposed a simple relationship, in which he proposed that the underlying reason of this phenomenon was the fluctuation in the conductance. He put forth that $\mathfrak{S}_G / G^2 = \alpha_H / Nf$, where α_H is the Hooge parameter, typically on the order of 0.002, and N is the mean number of charge carriers. We will simply say that the NEP depends on the frequency as $1/f$:

$$NEP_{1/f}^2 = \frac{V_{1/f}^2}{|S|^2} \tag{2.28}$$

where

$$V_{1/f}^2 = \frac{\alpha_H I^2 R^2}{NVf} \tag{2.29}$$

with N being the carrier density and V being the volume of the film (Moftakharzadeh et al. 2008). Usually, better sample quality and better film growth techniques reduce $1/f$ noise. Many authors have suggested many options to reduce the $1/f$ fluctuations, and as many causes are out there. For example, Lacoe, et al. (1991) propose that it is magnetic flux noise. Richards (Richards 1994) also considers that the $1/f$ fluctuations are due to charge carrier fluctuations, although he observes that better electrical contacts leads to less $1/f$ noise. Karmanenko, et al. mention that film quality is a primary source of $1/f$ noise (Karmanenko et al. 2000).

Among other noise sources is the background photon noise. This is considered to be coming from various greybodies with different emissivities. Cooling as many of the items as possible, such as cooling the IR filters, is one option to remove this noise, but this process may not always be viable. This thermal noise obeys Bose-Einstein statistics. Furthermore, the radiation source itself may be noisy. If it is a blackbody, then the noise will also follow Bose-Einstein statistics. If, however, it is a laser and the fluctuations are

those of the number of photons emitted, then the noise will have a Poisson distribution.

2.5.2. Noise due to Readout Circuitry

The readout circuit, starting from the contacts made on the bolometer chip, could end up being the greatest noise source. Most of the noise from the readout circuitry can be avoided, but some are inevitable. The contact noise is due to the temperature difference fluctuations between the contact pads and contact wires, which can force the contacts as a thermocouple with a noisy voltage. Similarly, the capacitance of the contacts could change due to mechanical vibrations. Next up in the readout circuit is the preamplifier. While the preamplifier may introduce noise, using impedance matching and a good quality preamplifier removes this problem. The current source and the voltage reader may also have their noise. One sort of noise (and a source of miscalibration) that can be avoided is the temperature variation inside the various measurement devices, which lead to extraneous thermocouple voltages. Turning on these elements some time before the experimentation would even out these differences and remove this problem. One noise that can't be overcome is the Johnson noise of the readout circuit, but this can be avoided with an appropriate choice of load resistance. Yvon, et al. (2008) have outlined their problems in building the low-T_c bolometer for the Planck Instrument satellite. From the placement of the wires of the readout circuit to the manner of interpersonal relationships between the technicians of different devices, they tell a lighthearted story with a serious message about how to optimize bolometer performance.

2.5.3. Noise due to Instrumentation

In this section, we discuss the noises introduced by the supporting elements of the experiment. The first and foremost among these is the temperature controller. No matter what one sets his PID values as, if the thermal link between the cold finger (to be maintained at the transition temperature of the bolometer) and the LN_2 bath (at 77K) is strong, the temperature fluctuations will take a long time to die out, if they die out. Weakening this link can improve the temperature fluctuations of the cold head (not to be confused with the temperature fluctuations across the boundary of the substrate and the cold head, which is a fundamental result of statistical physics) by up to two orders of magnitude. This noise is especially important for a transition edge bolometer because one

needs to hold the bolometer reasonably steady at its mid-transition point.

The next important point is the noise of the amplitude modulator of the incoming radiation. This is particularly important in the case of a mechanical chopper, which is not much more than a glorified step motor. Such an instrument will have wobble, and worse, have a wobbling frequency. The only way to remove this problem is to throw money at it, buying a better chopper. Finally, we talk about microphony, the mechanical vibration noise. Electrical readout parts, or any other moving parts, may vibrate and cause noise. Building the experiment so that the resonance vibration frequencies are very high is one way to remove these noise sources.

CHAPTER 3

EXPERIMENTAL METHODS

In this chapter, we will discuss the experimental methods employed in this thesis. The first section will be on the preparation of our bolometers, from film growth (by a commercial company) to patterning. The next section is on determining the crucial thermal parameters of the bolometers such as the heat capacitance, heat conductance and thermal time constant. In the final section, we discuss the electrical characterization of the chips as well as bolometric and pixel array measurements.

3.1. Preparation of samples

This section will be dedicated to the process of obtaining the bolometer meanders. It will briefly discuss the thin film growth technique adapted by the commercial company from which we bought our films, then briefly touch upon structural characterization methods and finally detail the process of patterning the films.

3.1.1. Thin Film Growth

Our films were grown by Theva GmbH, a commercial company from Germany. They start their growth procedure by cleaning the substrates by spinning them with alcohol and mounting them on the substrate holder under laminar air flow. They then move the substrates, sealed, to the growth chamber. Theva's growth technique is based on thermal co-evaporation, which can be classified as physical vapor deposition (PVD) from the basic metallic ingredients. They evaporate the basic metals (Y, Ba and Cu) and the evaporated metal atoms reach the rotating substrate holder. The substrate temperature is kept at 650°C. These metal vapor atoms are captured on a turntable and passed through a pocket with enhanced oxygen pressure (the oxygen pressure is two to three orders of magnitude higher). The details of this deposition method is proprietary, but the generalities are discussed in a white paper (Prusseit 2000).

3.1.2. Structural Characterization

The grown films were characterized by SEM and XRD both at the commercial company and at the Materials Research Center at IYTE. Scanning electron microscope (SEM) is used to take snapshots of the surface at high magnifications. While it doesn't provide quantitative roughness measurements, it gives a very good idea about surface morphology. X-Ray detection (XRD) gives the chemical composition of the film as well as how well the crystal forms. For YBCO, the FWHM of the 2θ (005) peak, occurring at 38°, is used to determine how good a c-axis crystal is obtained. As a rule of thumb, its FWHM must be less than 0.5° for the film to be considered highly c-axis. In the XRD peaks, only YBCO peaks and those peaks of the substrate should be observed.

The Materials Research Center at IYTE uses a Phillips^{TM}XL-30S FEG SEM apparatus and Phillips^{TM}X'Pert Pro XRD apparatus.

3.1.3. Patterning

After the films were satisfactorily deposited, they needed to be patterned into meander type bolometers. First, photolithography masks were prepared using a vector graphic software (see figures 3.1., 3.2. and 3.3.. For each bolometer design, positive and negative masks were prepared, as well as contact metallization masks. In the case of etched substrate chips, etching masks were also prepared. The masks were printed on acetate with a printer having more than 2000 dpi resolution.

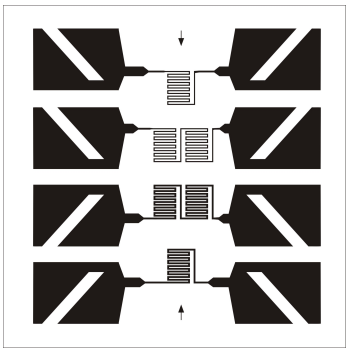

Figure 3.1. The mask used for the meanders for the independent response amplitude and phase versus frequency measurements. The meanders are 30μm and 50 μ m thick.

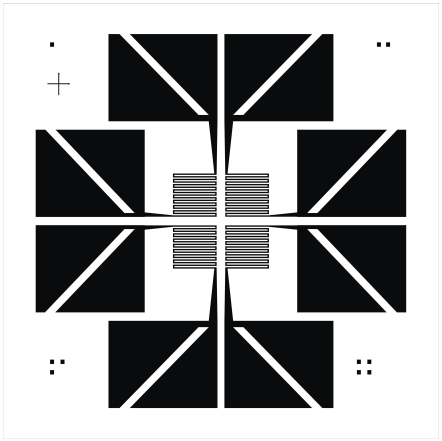

Figure 3.2. The mask used for the crosstalk measurements without the etched substrate. The meanders are 30 μm thick.

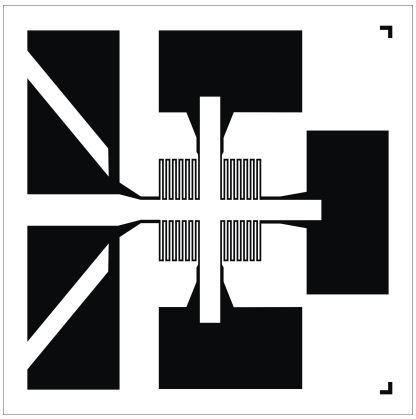

Figure 3.3. The mask used for the crosstalk measurements with etched substrate. The meanders are 30 μm thick.

The next step was to coat the films with the appropriate photoresist mask. The films were cleaned with isopropyl alcohol and pressurized 99.99% nitrogen gas before this process and visually inspected under an optical microscope for cleanliness. Then, the films were spin coated with AZ1505 positive photoresist. The spinner was homemade using a 5400 rpm hard disk. These spinners have the potential to give better results than their commercial counterparts because of the lack of wobble in their operation (see figure 3.5.). 3 droplets of the photoresist during 1 minutes of operation was the recipe used. The film was then held at 95°C for 75 seconds in a process called *soft bake* to remove the solvent in the resist. After this process, the primary pattern mask was aligned on the film and the masked film was exposed to 200W near UV light for 22 seconds. Immediately after this process, the photoresist was developed in AZ 726 MIF solution for 5-6 seconds

and rinsed in DI water. The pattern was then visually inspected under optical microscope. If this visual scan showed any faults, the photoresist was removed via acetone, alcohol and finally DI water and the process was started anew. If the pattern passed the visual test, the film was hard baked at 115°C for 65 seconds to harden the photoresist to form the etching mask.

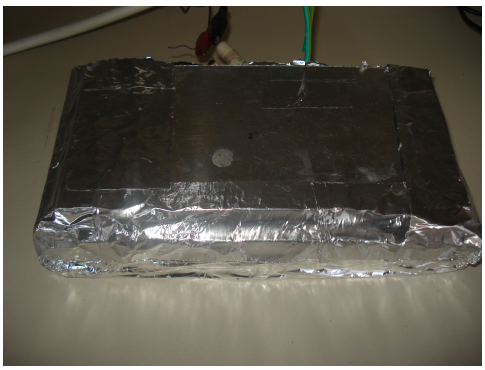

Figure 3.4. The homemade hot plate used in patterning.

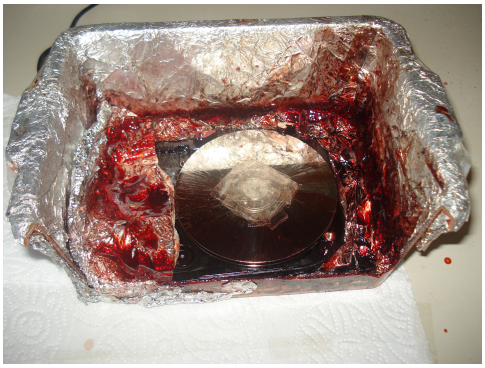

Figure 3.5. The home made spinner used in patterning.

Table 3.1. The sample codes and dimensions of the meanders shown in figures 3.1., 3.2. and 3.3., as well as the lengths and thicknesses of the meanders produced. B_1 and B_2 are shaped with the mask in figure 3.1.. B_3 is shaped into figure 3.2.. B_4 is shaped using figure 3.3..

Sample Code	Width, Area	Substrate	Film Thickness
B_1M_1	30μm, 0.3mm^2	MgO	300nm
B_1M_2	30μm, 0.6mm^2	MgO	300nm
B_1M_3	50μm, 0.5mm^2	MgO	300nm
B_1M_4	50μm, 1.0mm^2	MgO	300nm
B_2M_2	30μm, 0.6mm^2	LAO	200nm
B_2M_3	50μm, 0.5mm^2	LAO	200nm
B_3M_2	30μm, 0.54mm^2	STO	200nm
B_3M_2	30μm, 0.54mm^2	STO	200nm
B_4M_1	30μm, 0.45mm^2	MgO	200nm
B_4M_2	30μm, 0.45mm^2	MgO	200nm
B_4M_3	30μm, 0.45mm^2	MgO	200nm
B_4M_4	30μm, 0.45mm^2	MgO	200nm

Then we moved on to the wet etching process. As the smallest detail in our films had the lateral dimensions of 30μm, the 0.5μm resolution limit of wet etching process was not an issue. Similarly, the 2000 dpi masks would have been unsuitable for patterns sized under 10 microns, but they worked well enough for us. 0.5% H_3PO_4 was used as etchant. Roughly 10 seconds was the time allowed for the etchant to work before the film was cleaned in DI water. The work of the etchant can be observed with naked eye, so the process was repeated as many times as necessary and prudent.

Next was the contact metallization. Here, a liftoff photoresist mask was used on the patterned film. An SPI^{TM}sputter coater was used to deposit gold on the contacts (see figure 3.6.). The deposition conditions were P_{Ar}=0.8mbar and I_{DC}=15mA. The target-substrate distance was set at 4cm and the deposition time was 2.5 min. The resulting gold thickness was 80nm.

Figure 3.6. The SPI^{TM}sputter coater used for contact metallization.

After contact metallization and the removal of the liftoff mask, the film was placed on the cold head. The thermal link between the liquid nitrogen bath and the cold head was already weakened; this prevented the use of the inbuilt heater (see figure 3.9.). A new heater was built using SMD resistors and attached to the cold head using Apiezon^{TM}N grease and mechanically fixed in place. The substrate was also affixed on the cold head using a very thin layer of Apiezon^{TM}N grease. It was placed as close as possible to the diode temperature sensor on the cold head as possible. Lakeshore^{TM}331S temperature controller was used to control the temperature. A $\pm$2mK stability was achieved (see figure 3.7.). Finally, the electrical contacts were made using silver paint. In all cases, 4-point contact method was utilized.

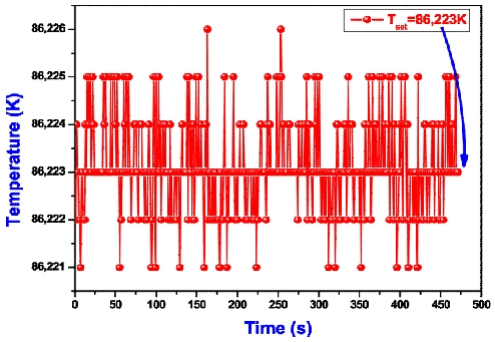

Figure 3.7. $\pm$2mK stability achieved with homemade modifications on the cold head of the cryostat.

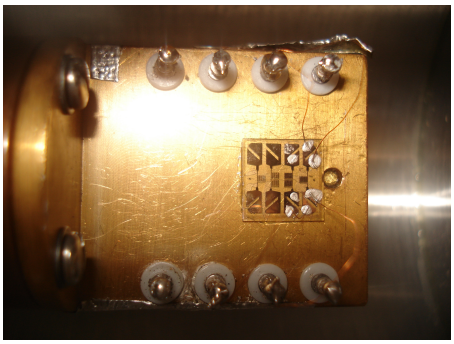

Figure 3.8. The cold finger with a chip mounted and contacts affixed.

Figure 3.9. The same cold finger, with the homemade heater installed.

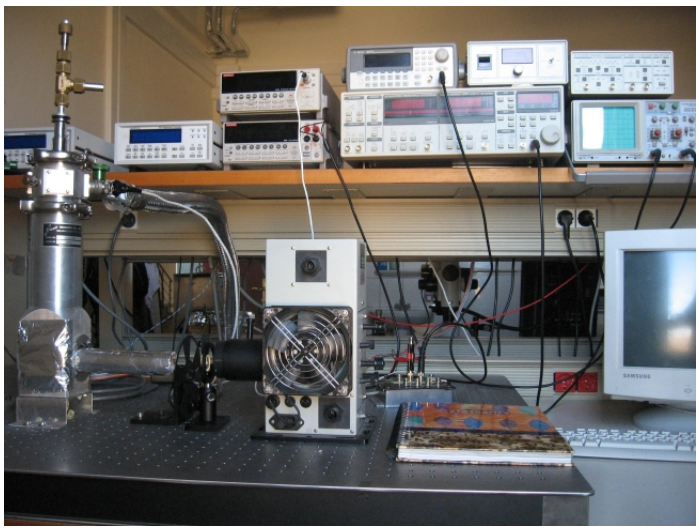

Figure 3.10. The electrical characterization system.

After the contacts dried out, the sample was put into the cryostat, which was then vacuum pumped to the lower limits of rough pumps. The optical window was covered by a very simple light tube, which ended with the mechanical chopper and the IR filter (see figure 3.11.). The system was thus prepared for electrical and bolometric characterization.

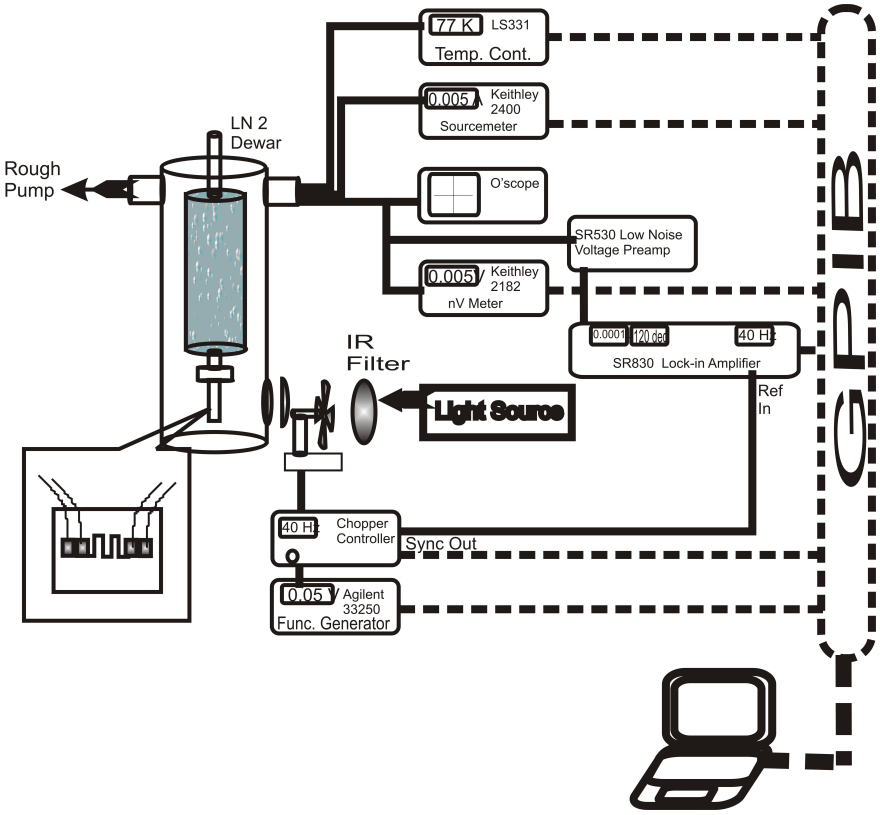

Figure 3.11. The schematic of the electrical characterization system.

3.2. Measurement of Thermal Parameters

The thermal parameters of the film, i.e. the heat capacitance, heat conductance and thermal time constant were measured for use in modeling and comparison with literature. The time constant was measured under chopped illumination on an oscilloscope. To measure heat conductance, the fact that the heat conductance of YBCO in the normal state close to T_c^{onset} is almost constant was used. An R-T graph under low current (and therefore negligible Joule heating) was performed, thus mapping the resistance of the film to temperature accurately. Then, a significantly high current was selected at a constant cold head temperature. The resistance of the film was again measured for that single current, and using the previous data, the temperature of the film was obtained. The temperature difference between the film and the cold head must be caused by the Joule

heating (Fardmanesh et al. 1995). Thus,

$$G = \frac{I^2 R}{T_{film} - T_{subs}} \tag{3.1}$$

The heat capacitance can be obtained from $\tau = \frac{C}{G}$. The time constant was measured by a 50 GHz oscillator aand was fount to be 8 ms.

3.3. Characterization and Measurements

In this section, various electrical and bolometric measurements are detailed. All of the measurements were automatized and done by a computer with the code written from scratch in LabView^{TM}. Communication with the instruments was supplied by a GPIB bus.

3.3.1. Electrical Characterization and Bolometric Measurements

All of the individual meanders underwent the following sets of measurements: Resistance versus temperature under no incoming light and with both low (100μA) and high (2-5 mA) current bias, the same resistance versus temperature measurements in the presence of light, amplitude and phase of response (with blackbody lamp and 95 mW HeNe laser) versus temperature for various bias currents, and amplitude and phase of response versus chopping frequency at the operating temperature and optimum bias current. The optimum current, typically 2mA, is calculated as detailed in section 1.3.2and experimentally roughly verified. Pixel measurements included amplitude and phase of response measurements of the illuminated and unilluminated pixels for various low (less than 100 Hz) chopping frequencies. When 0.95 mW, 1.5 mm diameter, 633 nm wavelength HeNe laser is used, no infrared filter is used. For blackbody radiation sources at 3200 K, a colored glass highpass infrared filter with 0% transmission at 800 nm and 90% transmission at 900 nm is used.

The readout circuitry starts from a metal BNC box. For R-T measurements, a Keithley 2182 sourcemeter for bias current and a Keithley 2400 nanovoltmeter is used. For the rest of the measurements, Keithley 2182 sourcemeter supplies the bias and a setup including Stanford Research^{TM}SR530 low noise voltage preamplifier and SR 830 lock-in

amplifier measures the output and noise. The lock-in amplifier is referenced to the chopper. The chopper is made by Oriel and is driven by a chopper controller from the same firm, but an Agilent 33250 function generator supplies the power because the function generator has a GPIB connector. Temperature of the system was read and PID controlled by a Lakeshore^{TM}331S Temperature controller. All of the systems were computer controlled (see figures 3.11., 3.12., 3.13. and 3.14.).

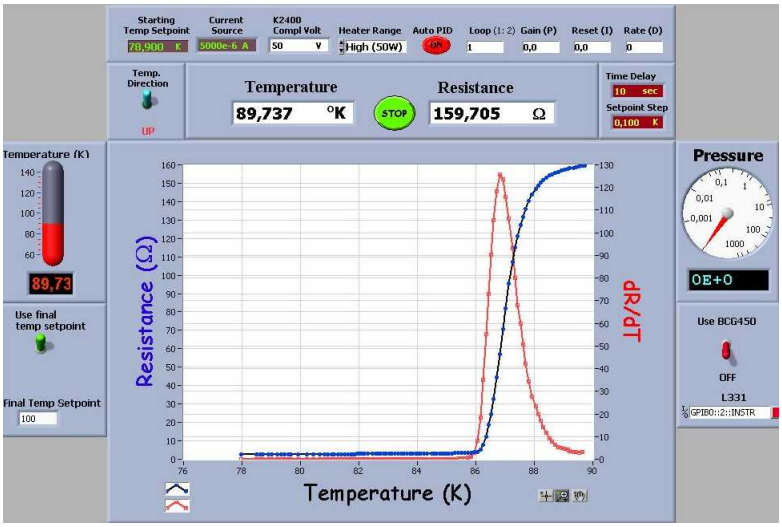

Figure 3.12. The R vs T measurement program written in LabView^{TM}.

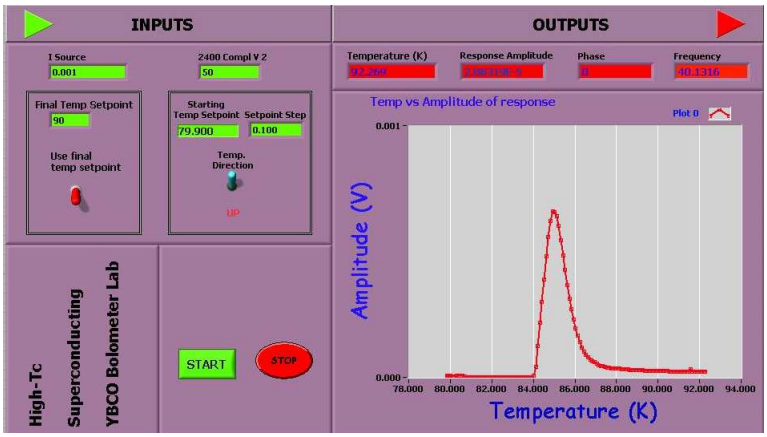

Figure 3.13. The amplitude of response vs. temperature measurement program written in LabView^{TM}.

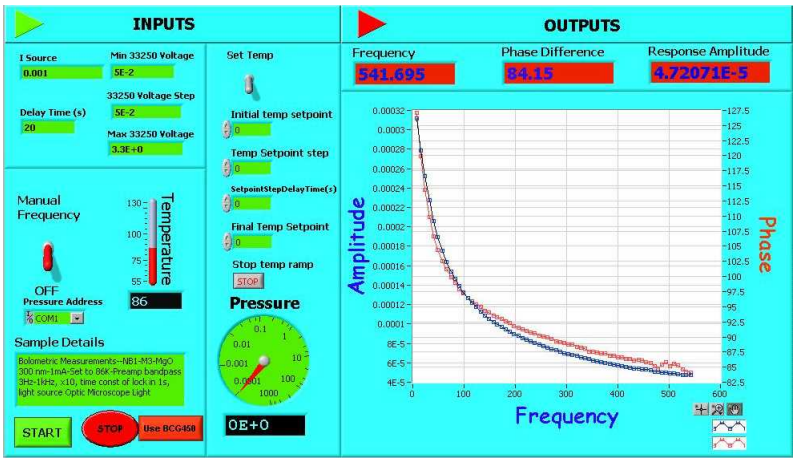

Figure 3.14. The amplitude of response and phase of response vs. chopping frequency measurement program written in LabView^{TM}.

In all of the measurements where we would have to vary temperature, we took the data either for both increasing and decreasing temperature, or only for increasing temperature. When increasing the temperature of the system from the cold bath value, the system is easier to control compared to when we let the system fall to an appointed temperature and then try to arrest the fall. The Lakeshore^{TM}331S temperature controller, as mentioned, uses a PID control system and autotuning feature is available. Moreover, we changed the setpoint values of temperature very slowly. Typical values were 0.1 to 0.2 K per 10-15 seconds. Considering that the time constant of our systems were on the order of ten milliseconds, we judged that this would be more than enough time for the film temperature to reach an equilibrium throughout the bulk of the film and the substrate. We checked this by looking at two-way RT graphs (taken both for increasing and decreasing temperatures). The two curves overlapped, so we concluded that our system was well-controlled temperature-wise.

3.3.2. Pixel Array Measurements

As mentioned in section 3.3.1, all of the pixels were individually electrically characterized before pixel array measurements were made. Two different pixel array configurations were investigated, in the first, the pixels were individually driven (see figure 3.2.) In the second, and the better configuration, all pixels were driven by the same source and the voltage difference across them were measured. This system would require $n+3$ contacts, where n is the number of pixels. The system is robust because if a pixel goes bad,

the adjacent pixels can be the start point of separate arrays at the cost of 3-point contact method being used instead of 4-point contact method.

Crosstalk measurements were made by illuminating one pixel with laser beam and measuring the response and phase of adjacent pixels. The effect of substrate etching between the pixels on crosstalk is investigated by first taking crosstalk measurements before the etching of the substrate, and then after the etching of the substrate. The etch depth was measured using a Dektak Profilometer.

CHAPTER 4

EXPERIMENTAL RESULTS

In this chapter, experimental results are presented. Structural characterization of the commercially obtained films were carried out and their results are noted. Then, all electronic characterizations of the chips and meanders are presented, along with bolometric response and fit to the theory. Lastly, pixel array response is discussed.

4.1. Structural Characterization

XRD and SEM measurements of the samples were obtained both by the commercial company that supplied our films (THEVA ^{TM}GmbH) and The Center for Materials Research at IYTE (see section 3.1.2). The results were similar. Therefore, only one of the result sets is included in this thesis.

4.1.1. XRD Results

XRD is the primary tool to test the epitaxiality and crystallinity of thin films, and to see whether any unwanted substances exist in the films. The accepted standard for high quality c-axis YBCO films is that the FWHM of the (005) peak of YBCO be less than 0.5 degrees. The FWHM values of the (005) peaks of our samples were measured to be 0.24° for the MgO substrate films and 0.2° for the STO/CeO and LAO/CeO substrate films. These results indicate a high degree of c-axis orientation (see figure 4.1.).

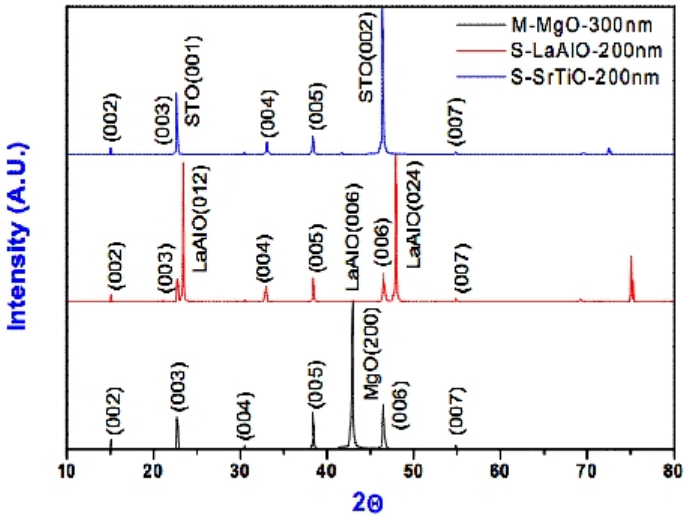

Figure 4.1. The XRD results of our films.

4.1.2. SEM Results

THEVA ^{TM}GmbH produce YBCO thin films by thermal co-evaporation method with three levels of surface roughness. We bought smoothest type (s-type in their nomenclature) and the next-rougher type (M-type in their nomenclature) films. The smoother films are intended for junction applications whereas the rougher films (with higher pinning center concentrations) are intended for high critical current applications. They adjust the surface roughness by adjusting the Y:Ba:Cu ratios. An excess of Y and Cu result in yttrium oxide and copper oxide compounds. Yttrium oxide cannot be overgrown easily, thus forming holes. These diffuse through the surface to form a hexagonal pattern around the copper oxide hillocks on the surface. Their M-type films have a larger amount of excess Y and Cu whereas the Y:Ba:Cu ratio in their S-type films is much closer to 1:2:3, producing a smoother surface. These effects can be seen in figures 4.2., 4.3., 4.4., 4.5. and 4.6.. Note the scale difference in figure 4.3..

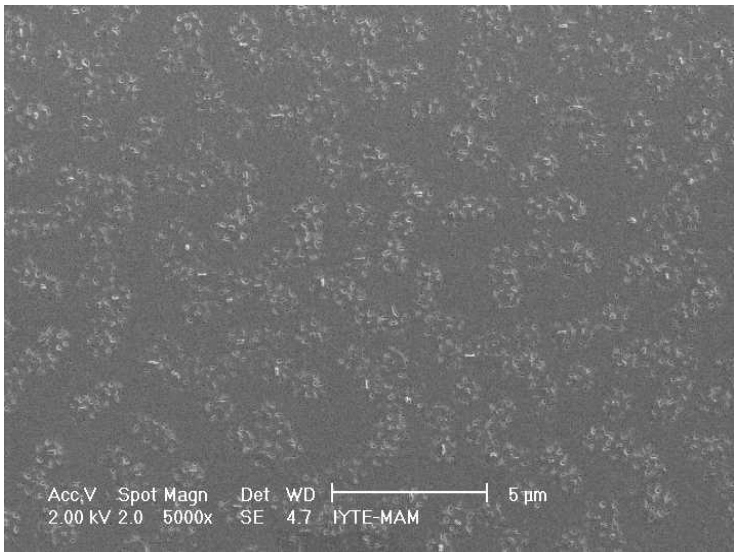

Figure 4.2. The SEM image of the film used to pattern B_1 (see table 3.1.).

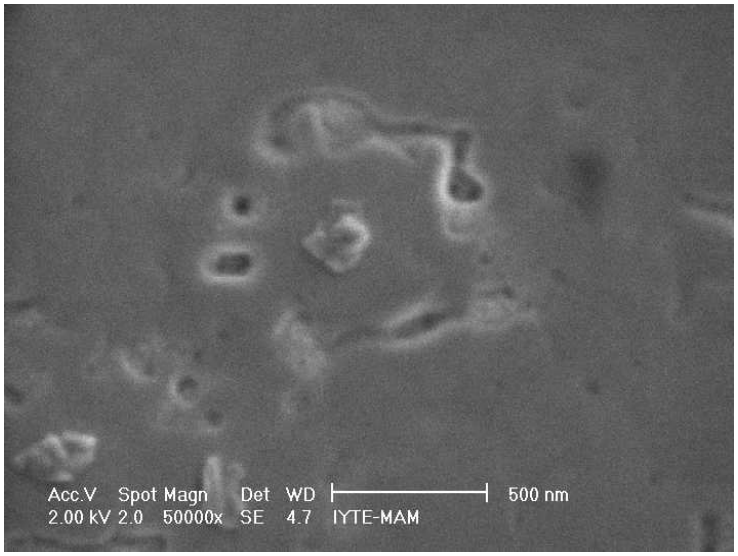

Figure 4.3. The structure repeated throughout the surface or our films, attributed to a surplus of copper and yttrium in the growth environment.

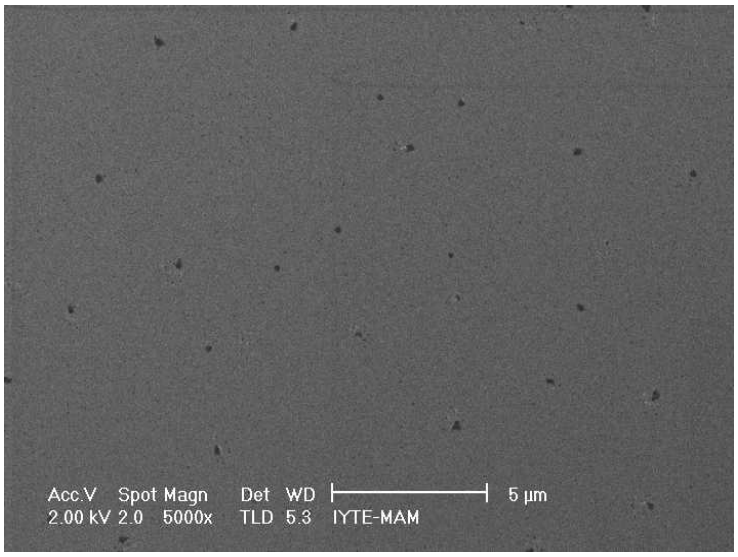

Figure 4.4. The SEM image of the film used to pattern B_2 (see table 3.1.).

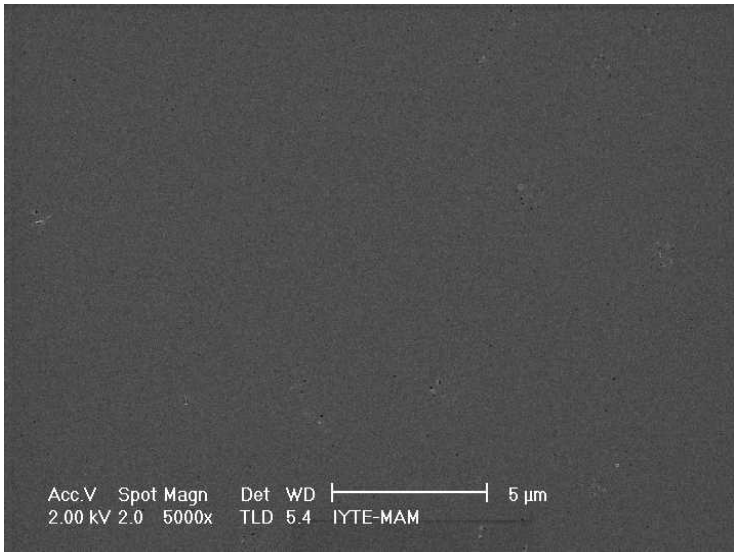

Figure 4.5. The SEM image of the film used to pattern B_3 (see table 3.1.).

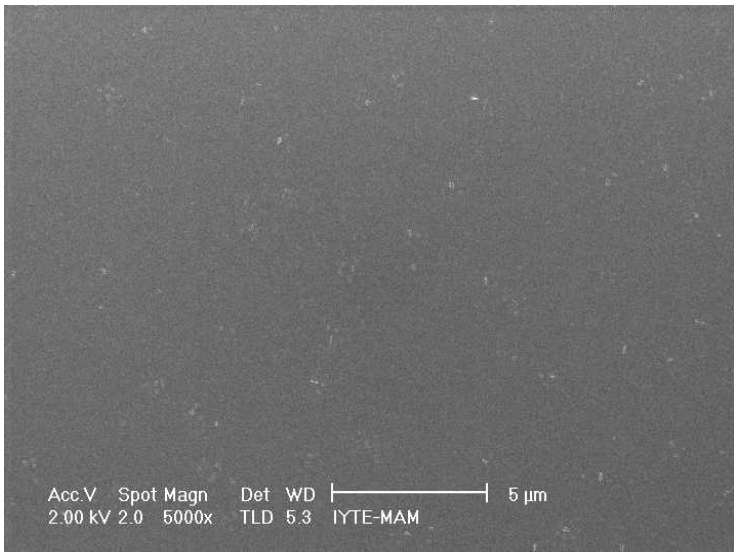

Figure 4.6. The SEM image of the film used to pattern B_4 (see table 3.1.).

4.2. Single Pixel Results

In this section, the characterization results for individual pixels is presented.

4.2.1. Photolithography Results and Contacts

After the pixels were prepared as described in section 3.1.3, they were mounted on the cold head and four-point electrical contacts were made (see figures 4.7.. The etching results were satisfactory. As can be seen in figures 4.8. and 4.9., the meander patterns were not perfect. This is partly due to the resolution limit of the printers used to create the photolithography masks. These imperfections create some noise, but as the penetration depth of YBCO is quite high, the problem is not as big as expected. Noise measurements will be presented in table 4.2. . The photographs of the meanders taken from an optical microscope are presented in figures 4.7., 4.10. and 4.11..

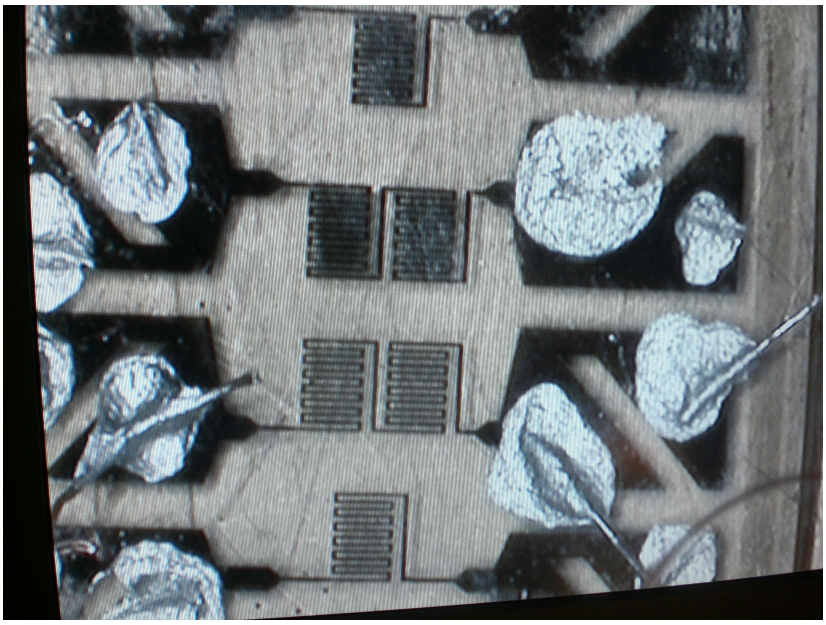

Figure 4.7. The B_1 bolometer with silver paint contacts (see table 3.1.).

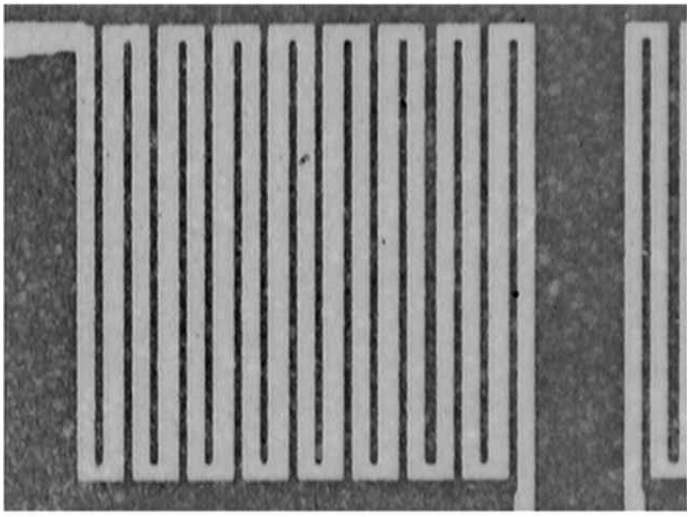

Figure 4.8. A meander detail from B_3 (see table 3.1.).

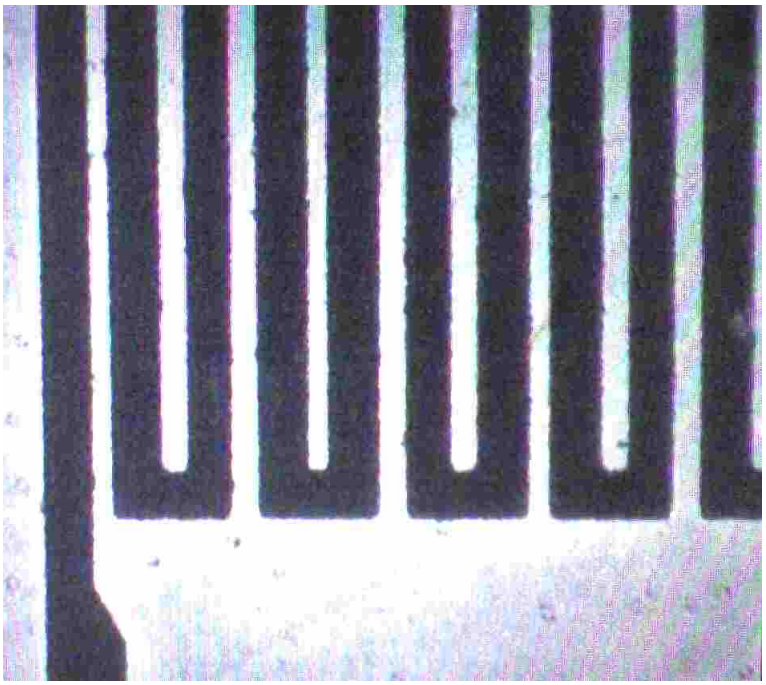

Figure 4.9. A meander detail from B_4 (see table 3.1.).

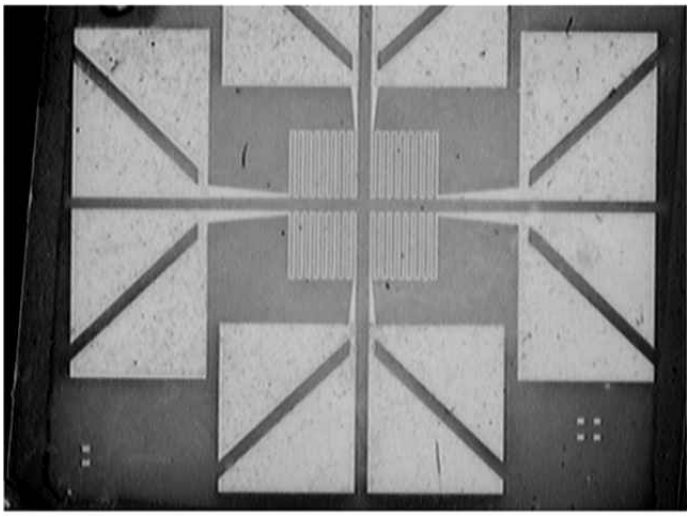

Figure 4.10. Overall picture of B_3 (see table 3.1.).

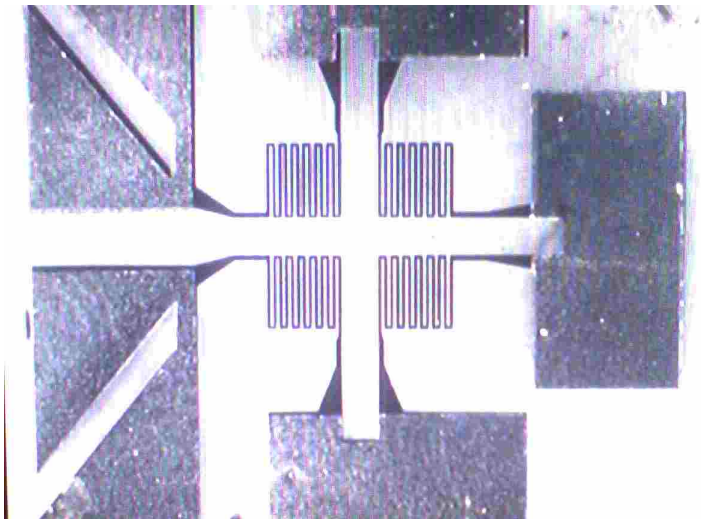

Figure 4.11. Photograph of B4 after contact pad metallization (see table 3.1.). The meanders form 1mm-wide squares.

4.2.2. Time Constant Measurements

The time constant of our bolometers were measured using a Tektronix^{TM}20 MHz oscilloscope directly connected to the voltage leads without any amplification or phase sensitive detection. These measurements have a certain amount of uncertainty due to the capacitance of the readout circuit, which adds to the time constant. On the other hand, as seen in figure 4.12., we can say that the time constant of our devices are on the order of 5 to 10 ms, which is consistent with what one expects from literature values of C and measurements of G. Literature gives the value of the heat capacity of MgO substrates as 0.53 J/K cm^3 (see table 1.1.). The area of a typical meander is on the order of 0.5 mm^2 (see table 3.1.). The thickness of the substrates are 0.5mm. This gives an overall heat capacitance under the meander as 0.13 mJ/K. The calculated value of heat conductance is roughly 11 mW/K (see below). This would result in a $\sim$10 ms time constant, which is close to the measured value.

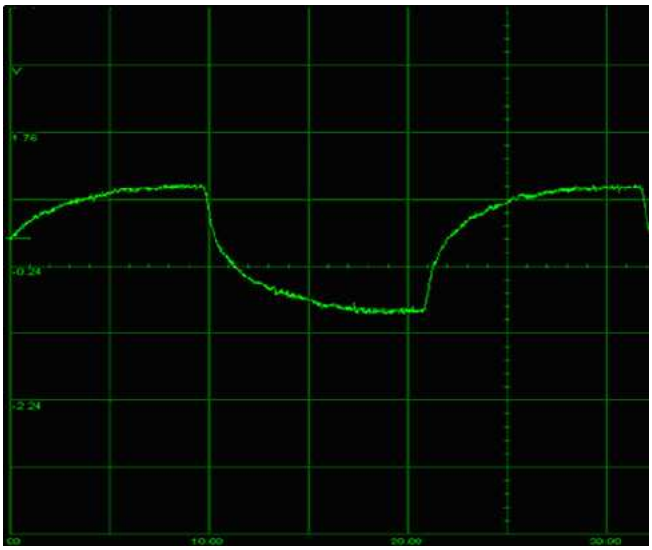

Figure 4.12. The time constant measurement for the B1M1 meander (see table 3.1.). The horizontal division size is 5ms.

4.2.3. Thermal Conductance Measurements

For the single pixel bolometers, we started our electrical characterization with IV and RT curves. The IV curve was used to obtain an IR curve in the normal region, from which we could obtain the thermal conductance of the bolometer (see figure 4.13.). At a constant temperature slightly above $T_{c-onset}$, the IV curve is taken and converted to IR curve. A second set of measurement yields the RT curve at a current with negligible joule heating, usually 100 μA for our pixels. This second curve is used as reference. The resistance corresponding to the low current of the RT data is read from the IR data. Again, from the IR data, a high current and resistance pair is chosen, and the temperature corresponding to the high resistance is read off from the RT curve. This higher temperature is caused by the joule heating of the superconducting film. From the definition of thermal conductance and using the data points indicated in figure 4.13., one obtains

$$
\begin{aligned}
G &= \frac{P_{in}}{\Delta T} \\
&= \frac{I^2 R}{\Delta T} \\
&= \frac{(9.7mA)^2\, 519.6\Omega}{4.5K} \\
&= 11mW/K
\end{aligned} \tag{4.1}
$$

Note that this is the thermal conductance of the whole system, from the film to the cold head. An important point to consider is the temperature dependence of heat capacitance. If there's a large thermal capacitance change within the 4.5K temperature difference indicated in figure 4.13., this calculation would be wrong. However, the heat capacitance of the substrate materials is a slowly changing function of temperature at the temperatures considered, and the heat capacitance of YBCO just above $T_{c-onset}$ is fairly constant (Uher and Kaiser 1987), so this is not an issue.

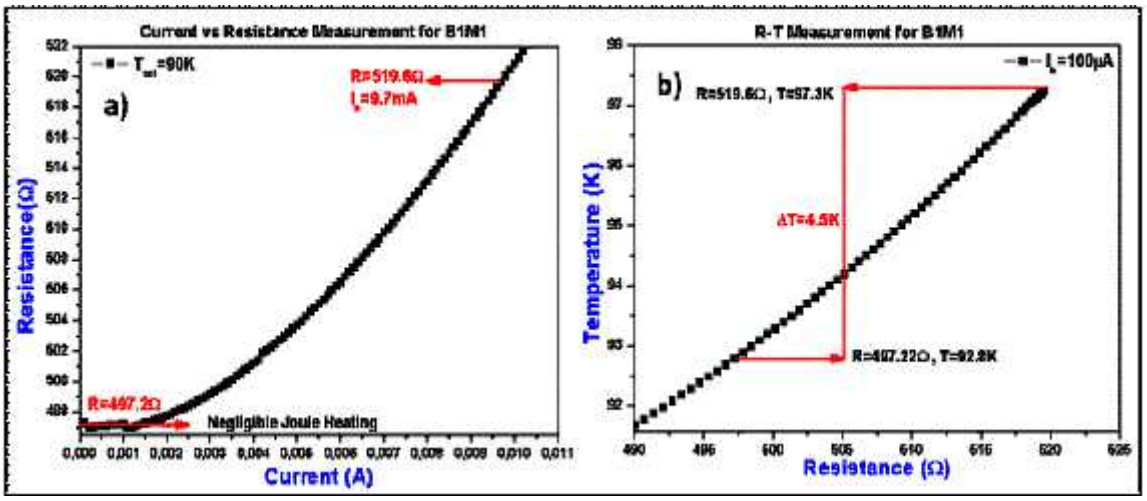

Figure 4.13. Calculation of thermal conductance from Joule heating. The figure on the left is the IR curve of the bolometer at a constant temperature slightly above $T_{c-onset}$. The figure on the right is the RT graph at a small current which would produce negligible Joule heating.

4.2.4. Resistance versus Temperature Results

The next step in the electrical characterization of our devices was the R vs. T (RT) and dR/dT vs. T measurements. A summary of our results can be found in table 4.1..

Note that the calculated resistivities of the devices differ within a film. This would be partly due to the defects in the film, defects in photolithography, and the effect of ignoring contact resistance and the resistance of the pattern from the meander to the contact pad. Nevertheless, the calculated resistivities are on the same order of magnitude. The resistivities of B3 are not calculated, because the low resistances shown in B3 (and visual inspection, once one knows what one is looking for) shows that the film is not well etched in the photolithography process. A very thin superconducting film is left on all of the substrate, which forms a short circuit. The dR/dT peak value directly affects the responsivity of the bolometer and the position of this peak is an important operating parameter.

Table 4.1. Summary of R vs T results. dR/dT_{max} is the peak dR/dT value.

Sample Code	R (Ω)	dR/dT_{max} ($\frac{\Omega}{K}$)	ΔT	ρ ($10^{-3}\Omega - mm$)
B_1M_1	80.2	302.4	2.3	0.396
B_1M_2	606.4	926.9	2.5	0.619
B_1M_3	380.3	782.7	2.1	1.365
B_1M_4	29.3	59.3	1.9	0.345
B_2M_2	563.8	1634.0	1.4	0.033
B_2M_3	307.4	805.4	1.6	0.013
B_3M_2	4.23	1.18	1.8	—
B_3M_3	5.08	1.61	1.1	—

The RT graphs of the meanders on the chip B1 are shown in figure 4.14.. In the normalized results, note the shortness of the transition tail. This is indicative of a good film. A bad film would have parts of it go to normal state first, creating an extended Shubnikov state, thus having a wide tail. This is an important quality for transition edge bolometers because this shows a narrow transition, resulting in a more sensitive dependence of resistance to temperature. Note also that the transition temperature of the meanders on the same film seem to differ. This is due to the fact that the temperature sensor is on the cold head. The temperature of the films will be slightly higher than what the sensor reads, due to Joule heating. Also, the thermal conductance of the substrate-cold head interface, which is provided by a hand-applied Apiezon^{TM}N-grease, may affect the result. Finally, on different measurements, the relative positions of the heater, the film and

the sensor may change. We did not try to optimize the uniformity of the transition temperature, as the control of the relative temperature is the important parameter in bolometer operation. As long as there's a controllable and good transition, a transition edge bolometer works equally fine whether the transition is seen at 80K or at 90K. The only exception to this rule is that colder temperatures lead to less noise of the cold side of the readout circuitry. The film noise is unaffected because the actual film temperature is at the actual transition temperature. A final point that could be made about these results is that the normal state resistances of the meanders are in the same order that the meander lengths and thicknesses would suggest, i.e. thicker and shorter meanders have less resistance.

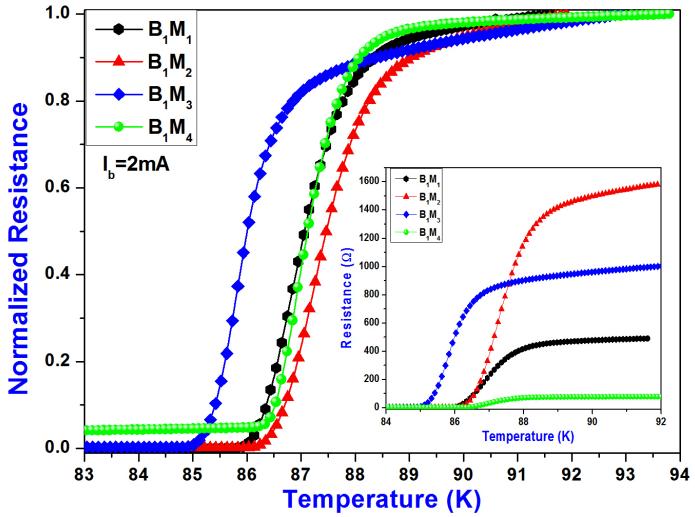

Figure 4.14. The normalized R vs T measurements for chip B1. The inset shows nonnormalized results.

On meander M1 of chip B1, we also looked into the effect of thermal runaway, as discussed in section 1.3.2.. We obtained the RT graph of the same meander under increasing bias current (see figure 4.15.). Note that the graph shifts left as the current is increased. This is due to the film being increasingly hotter than the temperature sensor. While the film would have a constant transition temperature, the temperature read by the sensor when the film is at this transition temperature is lower with higher current. Note also the steepening of the transition at 5mA. This is indicative of thermal runaway. The cold head cannot catch up with the input power (in the form of Joule heating in this case), so the film temperature rises faster than the temperature measured by the temperature

sensor on the cold head. Therefore the transition seems to be sharper. As discussed in section 1.3.2, we chose a current about 30% of this thermal runaway current. This is partly due to the fact that we would have an additional input power in the form of incoming light in bolometer operation.

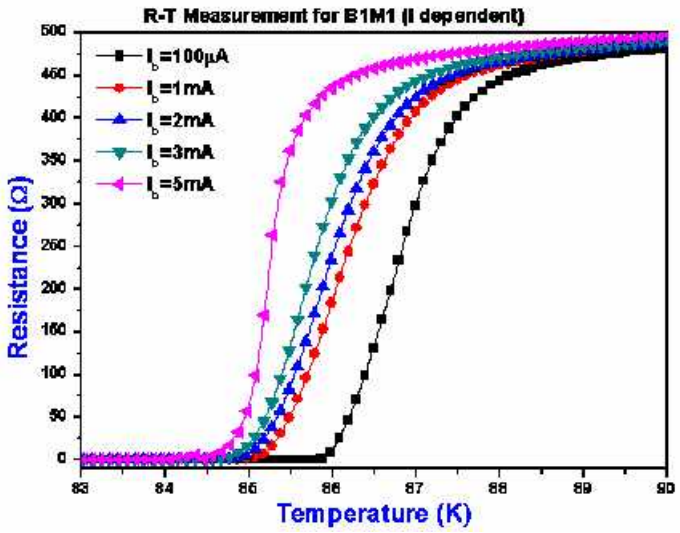

Figure 4.15. The RT measurements taken at different currents for B1M1. Thermal runaway effects can be seen at 5mA.

The dR/dT vs. T graphs of the meanders were numerically derived from the RT graphs realtime with the automation software. The result for the meanders for B1 is shown in figure 4.16.. The peak value of these graphs directly influence the responsivity, and mismatch between their shape and the shape of response amplitude versus temperature graphs should match if the observed response is completely bolometric. dR/dT values are positively correlated to R values, so the heights of the peaks follow the order of the normal state resistances of the meanders.

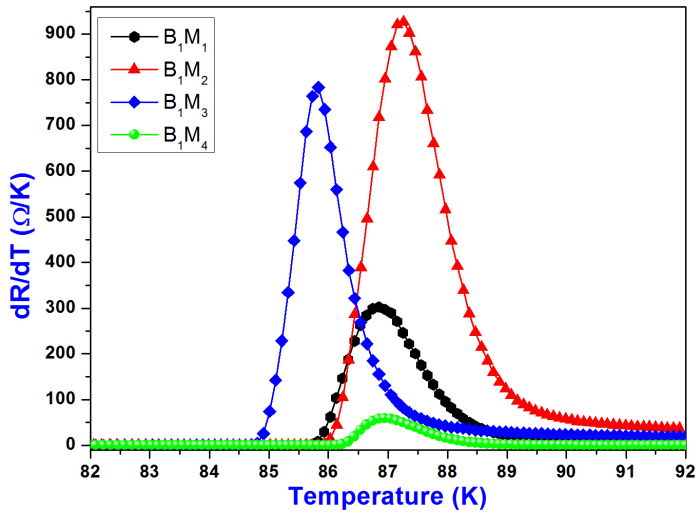

Figure 4.16. The dR/dT vs. T measurements for the chip B1.

In figures 4.17., 4.18. and 4.19., similar measurements for the meanders on chips B2 and B3 are seen. All of the discussion above for B1 applies to B2 and B3 as well. The only point of import is that the low resistances of B3 are due to the underetching of the film, leading to short circuits, as discussed above. Another important point is the positions of the transition temperatures. While this is partly explained by the temperature difference between the film and the temperature sensor, another reason for the low transition temperatures is deoxygenation under vacuum conditions, as discussed in section 1.3.1. The discrepancy may also be partly attributed to the fact that this chip stayed in room conditions (albeit protected from humidity and dust) for months before being used.

Two other points may be raised about these results. One is that meander M2 on Chip B2 has the sharpest transition and highest peak dR/dT value among the three chips. Another is that the artifact seen in meander B3M3 right after transition to normal state, which appears as a dip in resistance, is due to the bad etching and already low resistances measured.

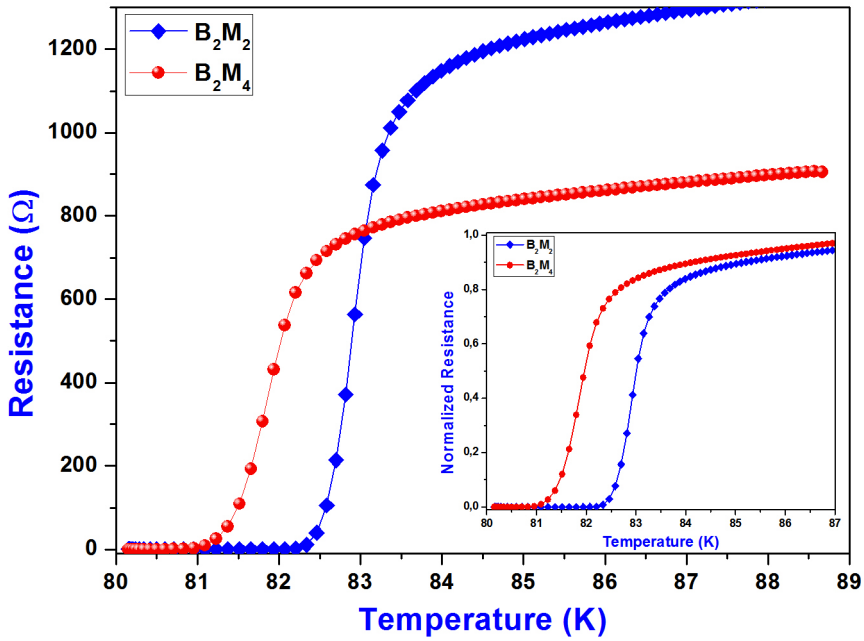

Figure 4.17. The R vs. T measurements of the B2 chip.

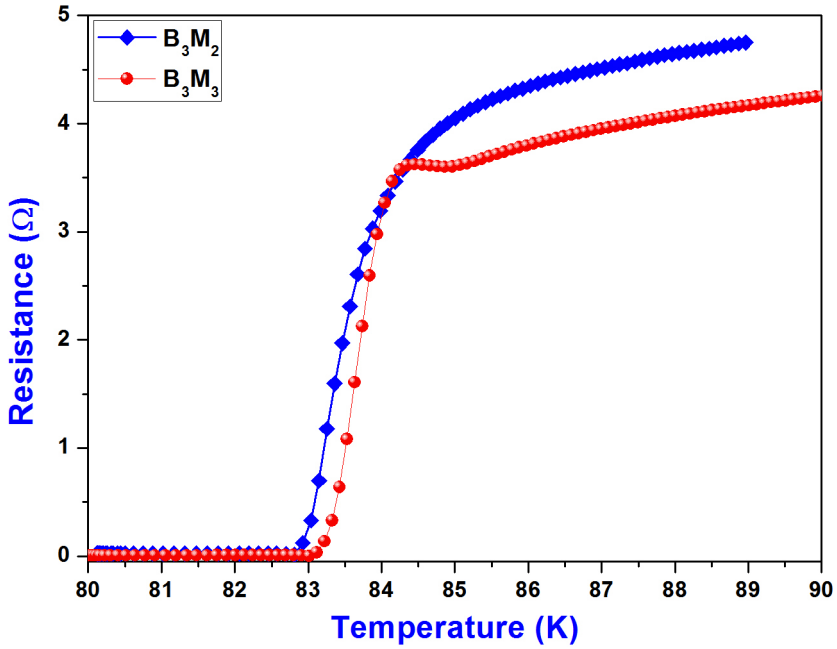

Figure 4.18. The R vs T results of the B3 chip.

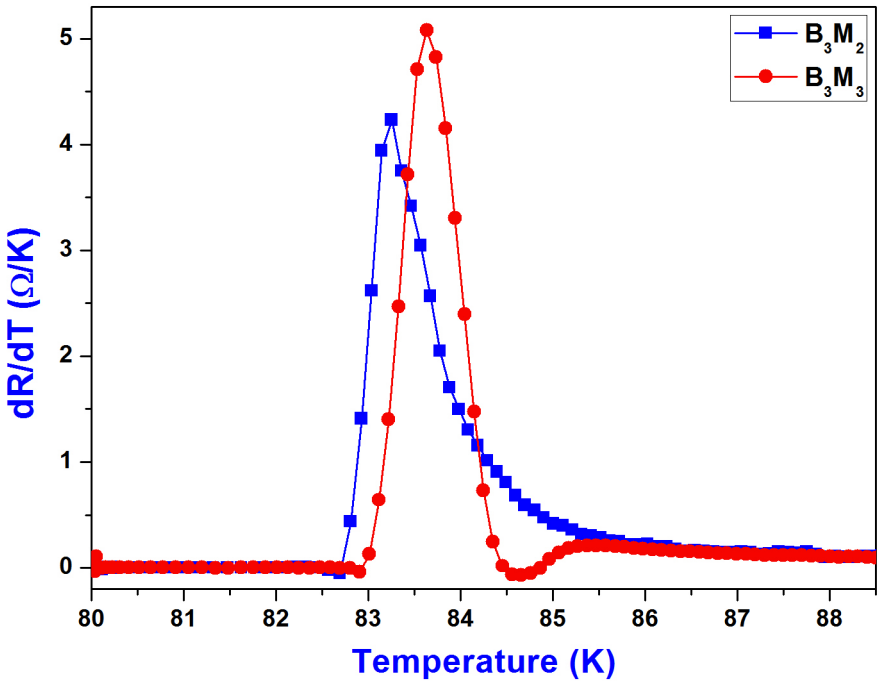

Figure 4.19. The dR/dT vs T results of the B3 chip.

4.2.5. Amplitude versus Temperature Measurements

The amplitude of response versus temperature measurements were taken with several purposes in mind. The first was to find the operating temperature of the bolometer under a given light source. The second was to see the peak response value to calculate responsivity. The third was to see whether the shape of the amplitude of response versus temperature (AT) curve would fit that of the RT curve, as would be the case if the response is completely bolometric. A summary of AT results can be found in table 4.2.. The Theoretical value of responsivity from the RC model is given in equation 2.6.

Table 4.2. Summary of A vs T results. $\mathcal{R}$ is the responsivity, $\mathcal{R}_{th}$ is the theoretical responsivity, NEP is the noise equivalent power and D^* is specific detectivity. All measurements are taken at 40 Hz chopping frequency.

Sample Code	$\mathcal{R}$ ($\frac{V}{W}$)	$\mathcal{R}_{th}$ ($\frac{V}{W}$)	NEP ($\frac{W}{\sqrt{Hz}}$)	D^* ($\frac{cm\sqrt{Hz}}{W}$)
B_1M_1	2.19	34.56	$\sim 7.4 \times 10^{-9}$	0.7×10^7
B_1M_2	12.96	41	—	—
B_1M_3	17.43	131	—	—
B_1M_4	0.8	19	—	—
B_2M_2	10.15	346	$\sim 1 \times 10^{-7}$	0.8×10^6
B_2M_3	1.61	135	$\sim 1 \times 10^{-7}$	0.8×10^6
B_3M_2	1.66	470	$\sim 1.2 \times 10^{-8}$	0.6×10^7
B_3M_3	1.31	450	$\sim 1.2 \times 10^{-8}$	0.6×10^7

The data in table 4.2. (except for the chip B3, for which we used a HeNe laser and 20 Hz chopping frequency)) was taken using an 3200K (uncalibrated) blackbody source, chopped at a frequency slightly different than 40 Hz, coupled with a highpass IR filter, putting the peak wavelength of the system at 900K. The bias current was 2mA in all of the measurements represented in table 4.2.. The chopping frequency was chosen so that it did not contain an appreciable amount of line frequency, which is 50Hz for Turkey. The theoretical responsivity assumes a perfectly aligned beam and an absorption coefficient of 1. Literature puts the absorption coefficient at below 20%, as discussed in section 1.3.4. . In this calculation, we used 28.8 μW as the total power of the incoming radiation, which we obtained using a spectrometer. We did our aligning with visible light and then inserted the IR filter in the path of the beam. We also measured the spot size using the visible light. While we were assured that the optical window of our cyrostat would pass visible and IR radiation equally up to 2000 nm by the manufacturer (Janis^{TM}), we did not carry out an independent verification of this. Moreover, while the lenses we used to focus the beam are rated well into the near IR region, they may have had different behaviors when switching from $\sim$600nm (the wavelength at which we carried out the alignment) and $\sim$900nm (the wavelength at which we carried out the measurements).

Finally, as the working wavelength is invisible, we may have inadvertently disturbed the alignment of the system during measurement. This factor, combined with the fact that we assumed the absorption coefficient of YBCO to be unity, accounts for the difference in obtained and theoretical responsivities. The factor of difference between the obtained and calculated responsivities seems to be fairly constant (on the order of 10) among the meanders measured within a chip. The NEP and specific detectivity were calculated using the voltage noise per square root hertz data from the lock-in amplifier and the responsivity.

The AT curves of the meanders on chips B1 through B3 can be found in the figures 4.20., 4.21., 4.22. and 4.23.. The meanders with larger areas absorb more radiation and therefore give a higher response. Among the meanders with similar areas, the peak value of the AT curves for each chip follow the order seen in the dR/dT vs. T peak values, as expected.

In figures 4.21. and 4.22., the RT results and AT results can be seen normalized and superimposed. The perfect mach between them shows that the amplitude of response is directly proportional to the dR/dT value. It also shows the lack of nonbolometric response at the averaging time constants we employed on the lock-in amplifier. The time constant of the lock in was set to 300 ms or 1s, and at these averaging times, whatever fast nonbolometric response may be seen has decayed away. This also shows the absence of long term nonbolometric response.

The data for B3 was taken with a 0.95 mW HeNe laser (633 nm) with a beam waist of 0.48mm, at a distance of 20 cm. As the resistance and dR/dT values for B3 was too low because of bad etching, we had to use a more powerful light source to get good data. Nevertheless, the calculated responsivities, NEP and specific detectivities were acceptable and on par with other meanders and literature, as shown in table 4.3..

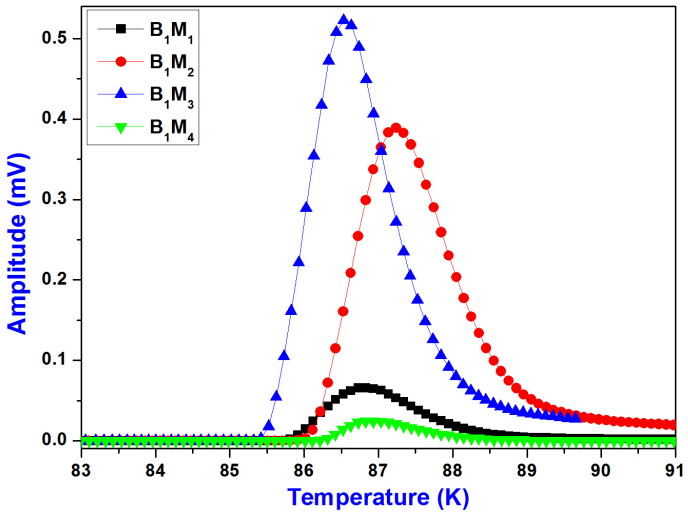

Figure 4.20. The response amplitude versus temperature graph of B1. The current was at 2mA and the light source was a filtered blackbody at Results

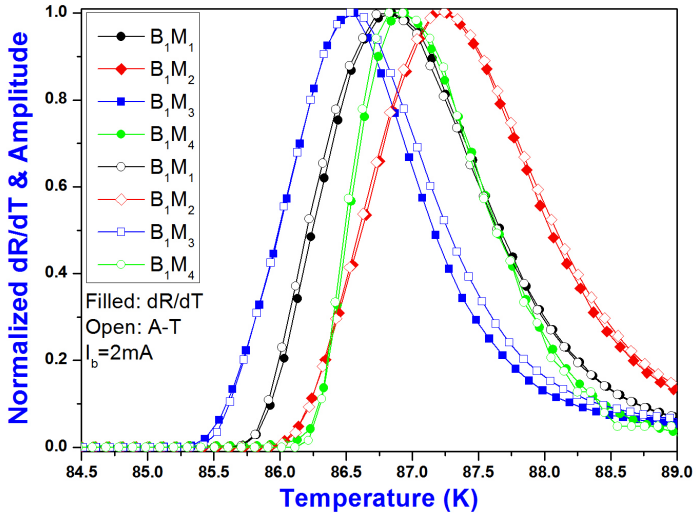

Figure 4.21. The response amplitude versus temperature and dR/dT versus temperature graphs normalized and superimposed. The results indicate a purely bolometric response.

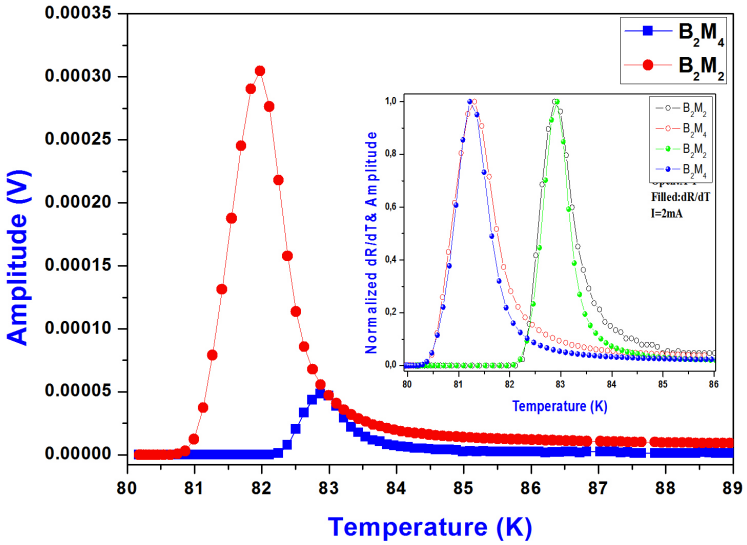

Figure 4.22. The amplitude of response versus the temperature results of the B2 chip. The inset illustrates the match with the dR/dT vs. T curves.

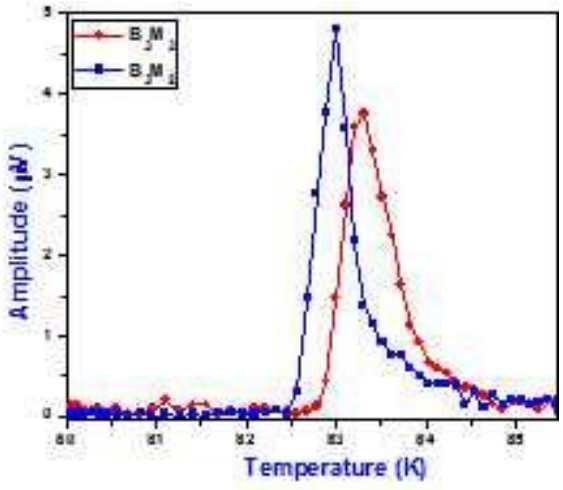

Figure 4.23. The response amplitude versus temperature graph of B3. The current was at 2mA and the light source was a highpass filtered blackbody at 3200K.

4.2.6. Amplitude of Response versus Chopping Frequency Results

We obtained the amplitude of response vs. chopping frequency (AF) curves of our devices for frequencies ranging from 5 to 550 Hz. We then fitted this data to the data given by the RC model, including the effect of substrate-cold head resistance, as discussed in section 2.1. This was done for two reasons. The first is to see how well

the RC model describes the bolometric response. The second is to identify the knee frequency, the frequency at which the thermal penetration length equals the thickness of substrate. As discussed in section 2.1, above this frequency, the boundary resistance between the substrate and the cold head does not come into play. This would be an important frequency to know in bolometer design. The substrate-cold head resistance depends on the mounting process. This resistance may be nonuniform throughout the interface, and different mountings may yield different resistances. So if a uniformity is aimed in bolometer production, it would be advisable to operate in a region which avoids this resistance.

The AF curves for the meanders on chips B1 through B3 are presented in figures 4.24., 4.26. and 4.28.. The RC model fits are shown, for selected meanders, in figures 4.25., 4.27. and 4.29.. In all of the cases, there's an excellent fit between theory and experiment. The only fitting parameter used was the absorptivity η of equation 2.6, which is meant to include as an overall factor the alignment problems, absorptivity of YBCO and incoming power change discussed in section 4.2.5. Note that all of the data presented in this section is raw data (averaged only within the time constant of the lock-in amplifier) due to the excellent temperature stability of our system as discussed in section1.2.4. . Another point to note is that the thickness of our films and the film-substrate resistance should provide us with a second knee frequency, but this frequency is too high (hundreds of kHz) to be achieved with the mechanical chopper used in our experiments.

The knee frequency of B2, which is on a LAO substrate, is calculated to be at 70 Hz using equation 2.10 and is observed to be at 65 Hz. The knee frequency of B1, for MgO substrates, is calculated to be beyond 500 Hz, which was the limit of our experiments. The knee frequency for B3 on STO is possibly observed to be around 40 Hz. The calculations indicate a knee frequency of 16 Hz. This knee frequency at 16Hz would not be easily observable in our system because the mechanical chopper has a lot of wobble in its frequency at these frequencies. The data for B3 was very noisy. This was due to the bad etching problem and low resistance, leading to low response.

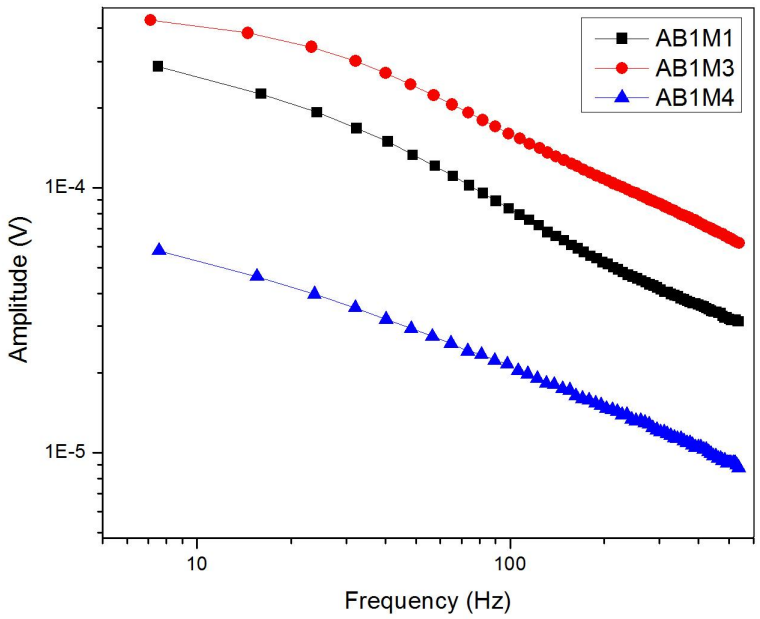

Figure 4.24. The amplitude versus frequency graph for B1.

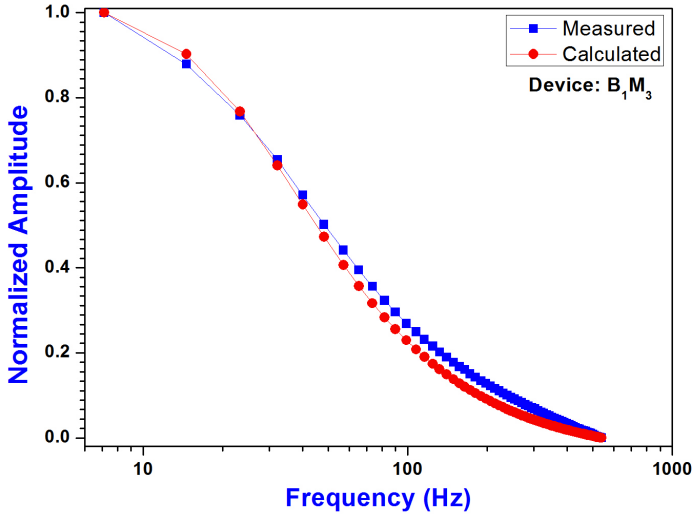

Figure 4.25. The RC model fir of a typical response from B1. The response is normalized; no other fitting parameters were played with.

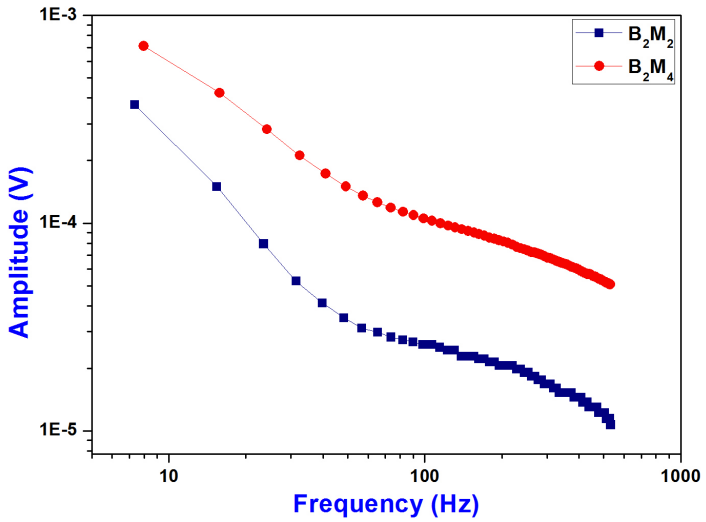

Figure 4.26. The amplitude of response versus the chopping frequency result of the B2 chip.

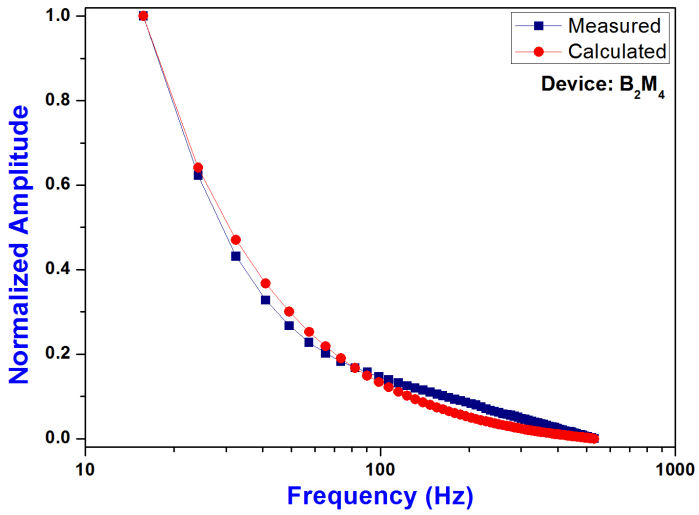

Figure 4.27. The amplitude of response versus chopping frequency results of the B2 chip, fit to the RC model.

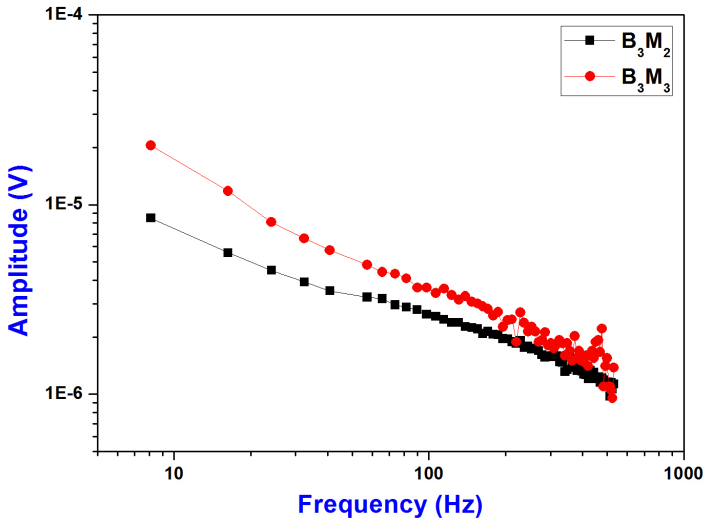

Figure 4.28. The amplitude of response versus frequency results of the B3 chip.

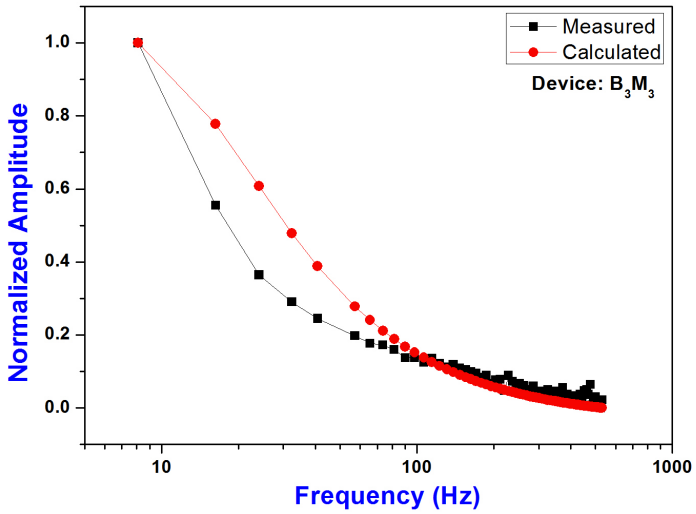

Figure 4.29. The amplitude of response versus frequency results of the B3 chip fitted to the RC model.

4.2.7. Phase of Response versus Chopping Frequency Results

The phase of response of our meanders are shown in figures 4.30., 4.31. and 4.32.. The discussion on the origin of this phase may be found in section 2.1and in figure 2.2.

. The equation for the phase of response is equation 2.7. The effective conductance in the denominator leads to the presence of knee frequency in the phase of response. In our measurements, a constant difference could be found between theory and experiment due to the constant phase difference between the time reported by the chopper to the lock-in amplifier that light was allowed to pass and the actual time that the light passed through the chopper. For reasons discussed in section 4.2.6the phase data of B3 is noisy. Again, as discussed in the same section, a knee-frequency-like curve is seen for the chip B1 at about 500 Hz. It is definitely seen at 70 Hz for B2. According to equations 2.7 and 2.12, the tangent of the phase should go like $\sqrt{f}$ for frequencies below the knee frequency and be a constant for frequencies above the knee frequency. This is tested for the meander B3M2 as seen in figure 4.33.. As it can be seen, a $\sqrt{f}$ graph fits the data well for smaller frequencies whereas the data is fairly level for higher frequencies. This deviation occurs roughly at 70 Hz, which was the knee frequency measured for this meander.

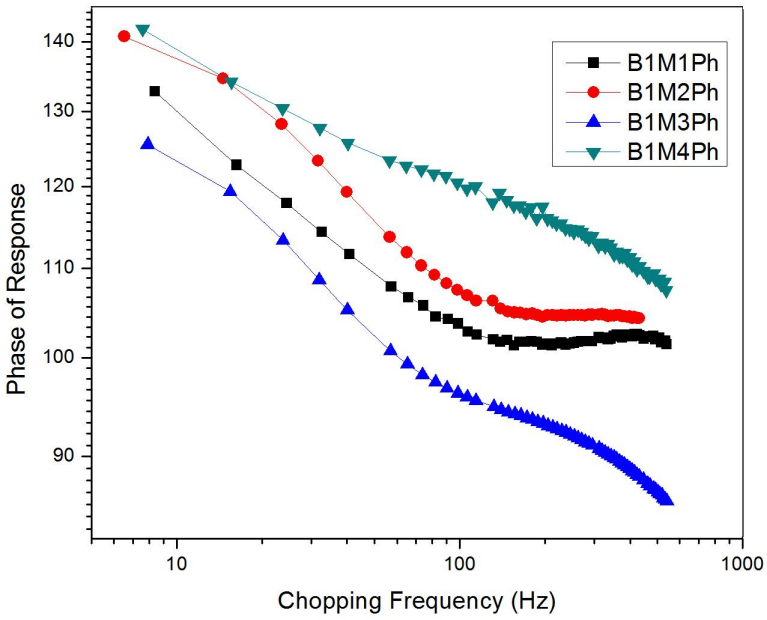

Figure 4.30. The phase of response versus chopping frequency for the B1 chip.

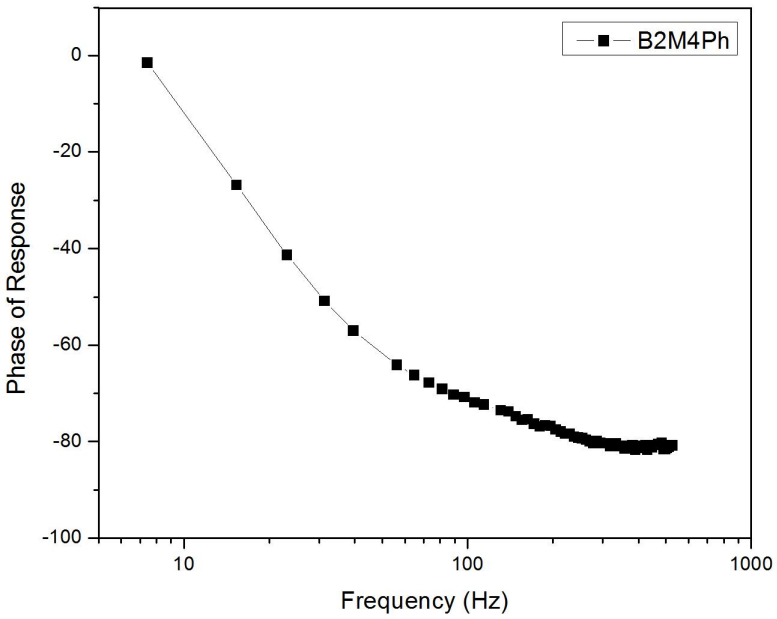

Figure 4.31. The phase of response versus chopping frequency results of the B2M4 meander.

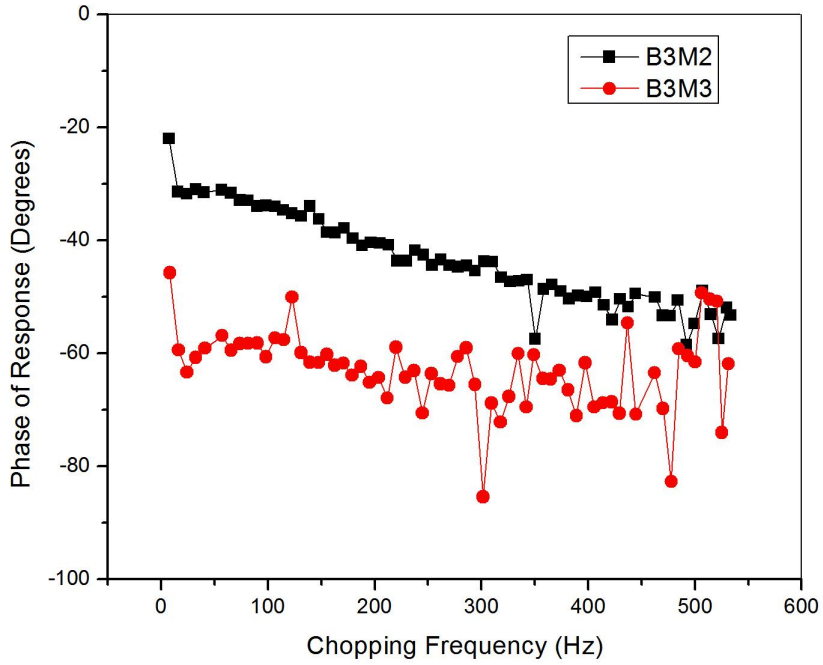

Figure 4.32. The phase of response versus chopping frequency.

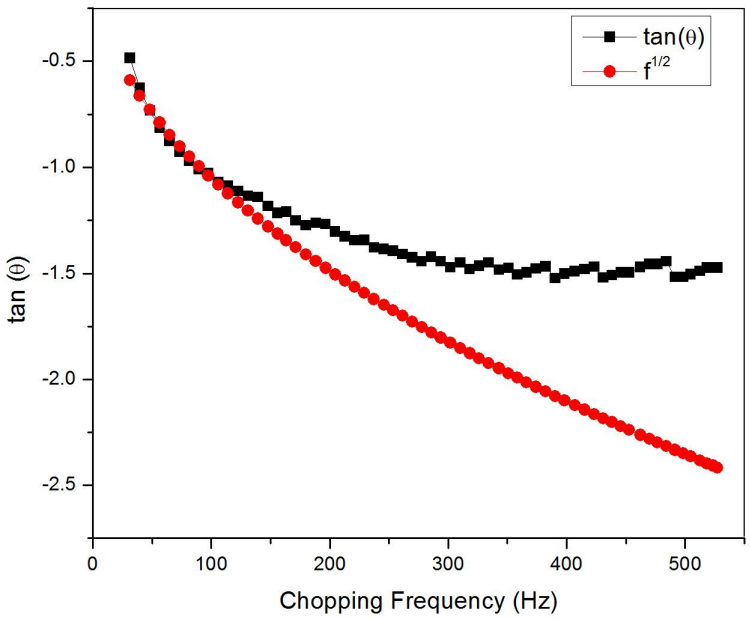

Figure 4.33. The RC Model fit to the phase versus chopping frequency data of B3M2. Note that the tangent of the phase levels out to a constant after a characteristic frequency. Note also that a constant times $\sqrt{f}$ fits the data well before this frequency and it deviates largely from this data after the vicinity of this frequency.

4.2.8. Measurements of Noise and Figures of Merit

The voltage noise per bandwidth was measured using the noise measurement feature of the Stanford Research^{TM}SR830 lock-in amplifier. This device records the deviation from a moving average and calculates the noise using an equivalent noise bandwidth derived from the time constant of the measurement and the steepness of the bandpass filter. It should be noted that this noise is the overall noise of the whole system, not just the noise of the bolometer meander. The noise measurements were made at 2mA, and at a frequency slightly different than 40 Hz for chips B1 and B2 and 20 Hz for chips B3. For chips B1 and B2, we used a filtered 3200K blackbody source, whereas for B3 we used a HeNe laser with 0.95 mW power. We had to use a different measurement setup for B3 because of the low response induced by the bad etching problem mentioned before. The calculated NEP and D* can be seen in table 4.2..

Table 4.3. Comparison of our results with those in the literature for similar structures, i.e. with the same substrate and in a thick substrate configuration. The responsivity figures are in [V/W], NEP figures are in [W/Hz$^{1/2}$] and specific detectivities are in [cmHz$^{1/2}$/W]. Literature MgO figures are taken from Eidelloth (1991), LAO figures from Moftakharzadeh et al. (2008) and STO figures from Leung et al. (1987). (Source: Eidelloth 1991, Moftakharzadeh et al. 2008, Leung et al. 1987)

	Our Devices			Literature		
	MgO	LAO	STO	MgO	LAO	STO
Responsivity	2.19	10.15	5×10^{-3}	10@10Hz	3.2@10Hz	$\ll1$
NEP	7.4×10^{-9}	10^{-7}	10^{-8}	3.9×10^{-8}	1.9×10^{-8}	10^{-6}@17Hz
D*	0.7×10^{7}	0.8×10^{6}	0.6×10^{7}	1.5×10^{7}	10^{7}	10^{6}

In table 4.3., we compare our single pixel results with those in the literature. The values chosen in literature have the same configuration as our devices, i.e. meander configurations on thick substrates of MgO, LAO and STO. The light sources are also at visible or near infrared wavelengths. As can be seen in the table, our results are comparable to or better than those presented in literature, except perhaps for the detectivity of the devices on LAO.

4.3. Pixel Array Results

In this section, we present the pixel array data for devices B3 and B4. B3 was meant to be a pixel array with the pixels driven independently for differing optimal conditions. The bad etching problem mentioned in previous sections made it hard to find an optimal spot. Nevertheless, pixel measurements were made. To overcome the small response problem, a 25 mW HeNe laser was used, with a beam waist of 1mm (roughly 1.3 mm diameter when the laser hits the pixels). The radiation was chopped at 15 Hz, a low frequency chosen for high response and acceptable wobble (the chopping frequency at any given time was within 0.15Hz of this setpoint). The preamplifier was set to $\times50$ amplification. The light was placed on the boxes on the chip indicated in figure 4.34. and

the measured responses are given in table 4.4.. The response in the tables is normalized so that each pixel reads 1.00 when light is on that pixel. A graphical representation of the data can be found in figures 4.35. and 4.35. . As can be seen in these figures, while the individual pixels respond to light when light is on them, they also respond strongly to light positions far from them. This can be explained by two effects. The first is that the responses of the pixels are so low that any extra heating produces a relatively large response. The second reason is that the light hits the connector lines and contacts on the chip, heating them up, thus producing response. In fact, the highest response is obtained with the light hitting the contact areas. No quantitative crosstalk analysis was carried out for this pixel array because of the problems described above.

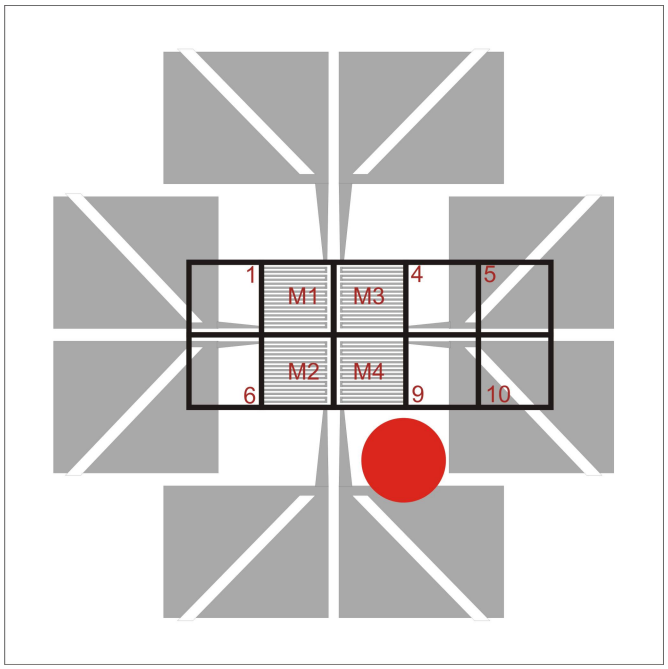

Figure 4.34. A schematic diagram of the positions of the laser beam (see table 4.4.) for B3. M2 and M3 were the measured meanders. Light was dropped into boxes 1 through 10. The red disk represents the size of the laser beam.

Table 4.4. The normalized response amplitude measured at meanders (pixels) 2 and 3 as a function of the position of the laser beam spot (see figure 4.34.). The upper block represents the response from B3M2 and the lower block represents the response from B3M3.

0.20	0.88	1.48	1.22	3.00
—	1.00	1.60	—	1.20
0.41	0.72	1.00	1.65	0.98
—	0.54	0.56	—	0.89

Figure 4.35. The response read from meander B3M2 when the light is shined on the corresponding box in figure 4.38. . Darker square means a higher response was read from the meander when the light was shined on the corresponding square. A white square means no measurement was taken from that square. Note that all of the above measurements were taken from M2, only the light's position is changed.

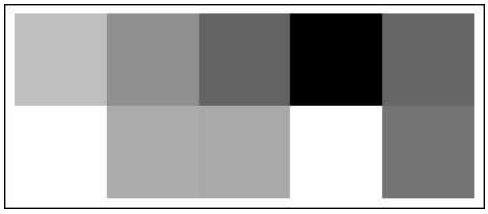

Figure 4.36. The response read from meander B3M3 when the light is shined on the corresponding box in figure 4.38. . Darker square means a higher response was read from the meander when the light was shined on the corresponding square. A white square means no measurement was taken from that square. Note that all of the measurements above are taken from M3, only the light's position is changed.

The pixel array B4 worked much better than B3, even though it sat in room conditions for a year before being patterned into a film. This is a testament to the versatility of YBCO thin film bolometers. However, in the process of measurement, due to human error, we had to warm up the chip quickly from LN_2 temperatures. A lot of water vapor condensed and froze on the chip. Even though we removed the vapor under warm flowing air, the RT graph of the chip showed a decrease in the critical temperature (which was not especially important for us), a decrease in the sharpness of the transition (which directly affects responsivity) and a general degradation of the quality of the film, evidenced in the elongated tail of the RT graph (see figure 4.37.) . This final degradation theoretically can be seen as noise, especially 1/f noise. Thermal cycling of films by itself is not a huge problem, even for Josephson junction devices patterned on YBCO films (Avci et al. 2007), but water condensation does a lot of damage. Nevertheless, the performance of the film as a pixel array was satisfactory, as can be seen in the response graphs below.

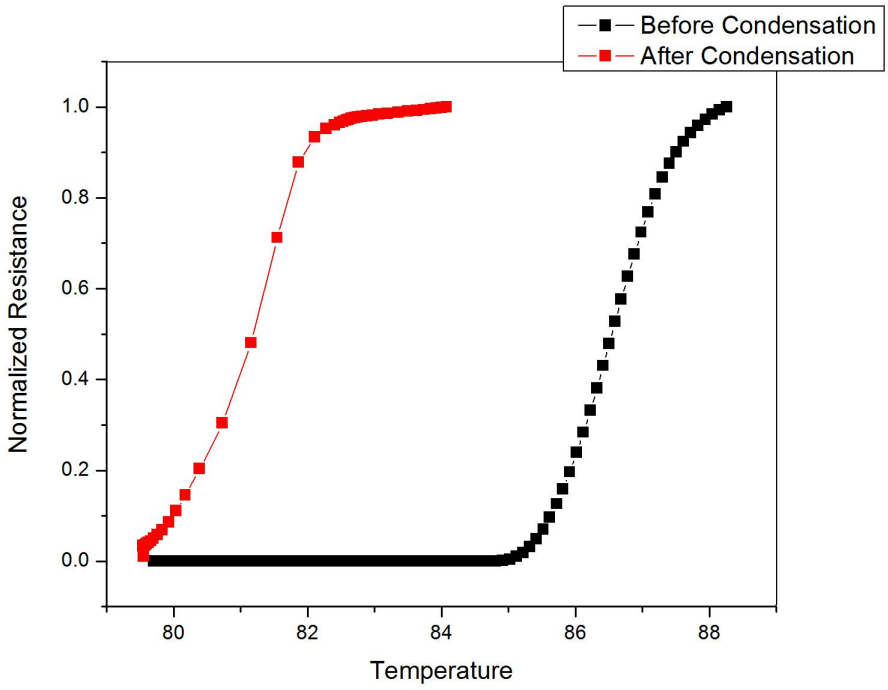

Figure 4.37. The RT Graph of B4M2 before and after a water condensation on the film due to human error.

For pixel response data for B4, we used a HeNe Laser with 0.48mm beam waist ($\sim$0.6mm diameter when it hits the chip) with 0.95mW power. It was chopped at 41 Hz. 500 mA current was used to bias all meanders at the same time. A higher current (such

as 2mA as before) could not be used because of the thermal runaway problem, which worsened after the water condensation. The preamplifier was set at $\times 5$ with a bandpass filter of 30 to 100 Hz. The lock-in time constant was set at 1s. The light was shined onto the boxes represented in figure 4.38.. The peaks of the AT graphs under the above conditions for the meanders were observed at 81.79K, 81.49K, 81.7K and 81.85K respectively for meanders M1 through M4. The whole system was set to 81.7K. The amplitude of response at this temperature for all meanders was used as a normalizing factor. The data presented in tables 4.5., 4.6., 4.7. and 4.8. are the normalized responses (actual response divided by normalization factor) read from meanders M1 through M4 when the light was shined on a corresponding position. For example, to find the normalized response of M2 when the light was shined on the fourth box on the third row in figure 4.38., look at the value at the third row, fourth column of table 4.6..

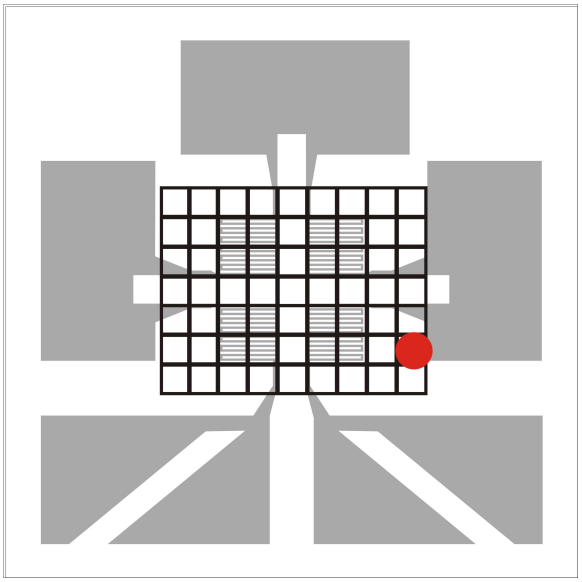

Figure 4.38. A schematic diagram of the positions of the laser beam for B4. Light was dropped into each one of the boxes. The red disk represents the size of the laser beam.

Table 4.5. The normalized response amplitude measured at B4M1 as a function of position of laser beam spot (see figure 4.38.). The position of a number in the table corresponds to a box position in figure 4.38. where the laser light was shined. Note that all of the measurements in this table were taken from M1, only the light's position is changed.

0.27	0.3	0.3	0.31	0.31	0.3	0.23	0.17	0.1
0.49	0.57	0.77	0.88	0.48	0.53	0.22	0.13	0.08
0.55	0.63	0.87	0.87	0.6	0.52	0.44	0.37	0.24
0.87	0.98	1.62	1.45	0.77	0.55	0.46	0.28	0.19
1.01	1.66	2.83	2.87	0.93	0.89	0.55	0.25	0.19
0.9	2.05	3.02	2.01	0.81	0.85	0.5	0.25	0.17
0.35	0.47	0.65	0.98	0.67	0.57	0.36	0.29	0.2

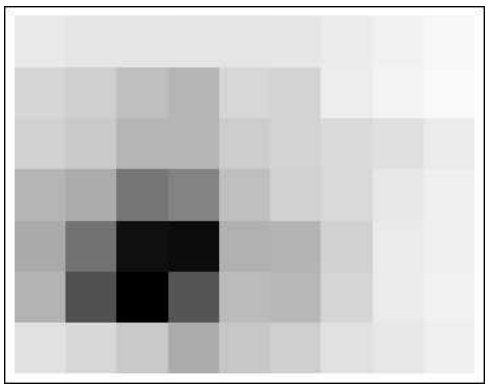

Figure 4.39. Response read from B4M1 for the laser spot in each box in figure 4.38. . Darker square means a higher response.

Table 4.6. The normalized response amplitude measured at B4M2 as a function of position of laser beam spot (see figure 4.38.). The position of a number in the table corresponds to a box position in figure 4.38. where the laser light was shined. Note that all of the measurements in this table were taken from M2, only the light's position was changed.

0.24	0.30	0.36	0.41	0.27	0.20	0.15	0.09	0.06
0.23	0.39	0.82	0.81	0.34	0.23	0.11	0.05	0.04
0.23	0.32	0.66	0.63	0.33	0.16	0.17	0.11	0.08
0.20	0.23	0.27	0.26	0.18	0.15	0.12	0.08	0.05
0.16	0.18	0.24	0.25	0.14	0.16	0.11	0.05	0.05
0.12	0.15	0.20	0.16	0.11	0.12	0.08	0.05	0.04
0.05	0.05	0.06	0.08	0.07	0.05	0.06	0.07	0.05

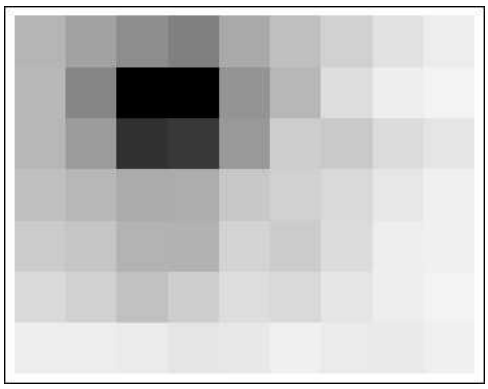

Figure 4.40. Response read from B4M2 for the laser spot in each box in figure 4.38. . Darker square means a higher response.

Table 4.7. The normalized response amplitude measured at B4M3 as a function of position of laser beam spot (see figure 4.38.). The position of a number in the table corresponds to a box position in figure 4.38. where the laser light was shined. Note that all of the measurements in this table were taken from M3, only the light's position was changed.

0.06	0.09	0.11	0.18	0.29	0.32	0.34	0.26	0.17
0.06	0.08	0.17	0.27	0.40	0.98	0.51	0.18	0.12
0.06	0.07	0.14	0.24	0.32	0.40	0.94	0.53	0.34
0.06	0.07	0.10	0.15	0.18	0.31	0.34	0.26	0.17
0.06	0.07	0.12	0.16	0.14	0.27	0.28	0.16	0.14
0.05	0.09	0.13	0.12	0.11	0.19	0.17	0.11	0.1
0.02	0.02	0.04	0.07	0.07	0.08	0.07	0.07	0.07

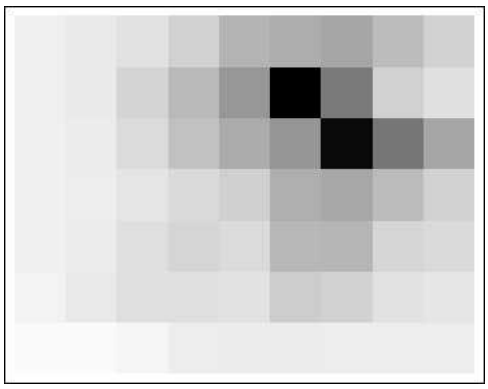

Figure 4.41. Response read from B4M3 for the laser spot in each box in figure 4.38.. Darker square means a higher response.

Table 4.8. The normalized response amplitude measured at B4M4 as a function of position of laser beam spot (see figure 4.38.). The position of a number in the table corresponds to a box position in figure 4.38. where the laser light was shined. Note that all of the measurements in this table were taken from M4, only the light's position was changed.

0.05	0.06	0.07	0.09	0.12	0.11	0.11	0.10	0.09
0.07	0.08	0.15	0.20	0.19	0.28	0.19	0.09	0.09
0.07	0.08	0.14	0.20	0.19	0.25	0.32	0.33	0.27
0.08	0.10	0.13	0.20	0.24	0.48	0.50	0.34	0.22
0.11	0.11	0.22	0.30	0.34	0.91	0.89	0.31	0.25
0.10	0.17	0.26	0.31	0.35	0.91	0.74	0.30	0.20
0.05	0.06	0.10	0.21	0.26	0.32	0.32	0.27	0.21

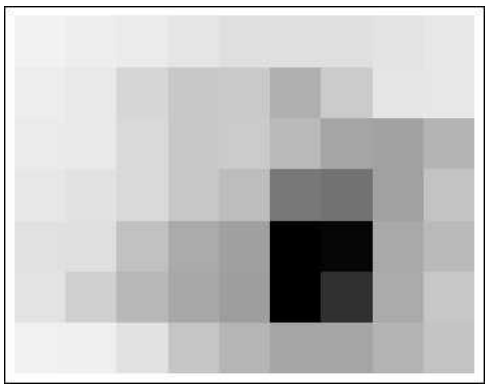

Figure 4.42. Response read from B4M4 for the laser spot in each box in figure 4.38. . Darker square means a higher response.

In all of these responses, the strongest response for each pixel is when the light shines on the pixel, as expected. Crosstalk effects are also seen. When light falls on immediately adjacent pixels, a heating of the readout pixel produces a nonzero response on the pixel. Nevertheless, visual inspection of the response color graphs indicates that most of the resolution limit of the pixels come from the pixel size at this configuration. This resolution can be made sharper with thermal isolation of pixels.

We used equation 2.21 to quantify pixel crosstalk. According to this equation, the temperature rise on one pixel due to the illumination of another pixel is proportional

to $\exp[\sqrt{\pi f/Dx}]$. For our case, the distance between adjacent pixels is 0.05 cm and the distance between the pixels which are diagonally opposite is 0.07cm. One would expect the 'effective' distance between adjacent pixels is smaller, as they have a side in common and can talk to each other easier, and the 'effective' distance between diagonally opposite pixels to be larger as they only have a corner in common.

As a first step towards this quantification, we averaged the normalized responses when the light was on a given pixel. These numbers can be seen in table 4.9.. It turns out that an empirical relationship within each quadrant may be found. The response of the nonilluminated pixels is well described by the response of the illuminated pixel times $\exp[-24.5cm^{-1} \times x]$, where x is either 0.05cm or 0.07cm, as discussed in the previous paragraph (see table 4.10.). This value, using equation 2.21, would correspond to 0.3cm^2/s for the thermal diffusivity of MgO , which is consistent with values in literature (see table 1.1.). This proves that the very simple model given in 2.21 is sufficient to do crosstalk analysis. The number $\exp[-24.5cm^{-1}]$, or similarly the natural log of the ratio of the response of an unilluminated pixel to an illuminated pixel for a standard distance, can be used to quantify the crosstalk amount between the pixels. A more negative number would imply a smaller amount of crosstalk.

Table 4.9. The normalized response amplitudes averaged over the pixels. The lower-left quadrant represents data taken from M1, found in table 4.5.. The upper left quadrant is from M2, upper right from M3 and lower right is from M4, all taken from their respective tables. Within a quadrant, the lower left number is the average of the four numbers on the corresponding table which coincide with the position of M1, The upper left is the average of the four numbers corresponding to M2, upper right to M3 and lower right to M4.

0.73	0.14	0.21	0.71
0.21	0.12	0.13	0.23
0.85	0.43	0.18	0.27
2.68	0.70	0.27	0.86

Table 4.10. The theoretical values derived from equation 2.21, using the data in table 4.9.. Note the similarity of the numbers between the two tables.

0.73	0.21	0.21	0.71
0.21	0.13	0.13	0.21
0.79	0.48	0.15	0.25
2.68	0.79	0.25	0.86

CHAPTER 5

CONCLUSIONS

In this work, we patterned and tested monolithic YBCO epitaxial thin film tick substrate high $T_c$superconducting transition edge bolometers. We obtained structural characterizations of our films using XRD and SEM measurements. We then proceeded to the electrical characterization of the meander patterns. The electrical characterizations included obtaining RT and IV curves. From these curves, we obtained the thermal characterization of our bolometers. We then proceeded to obtain the bolometric measurements of single pixels, such as the amplitude vs. temperature, bolometric response vs. temperature and phase of response vs. temperature data. We compared all of these data to theoretical models and obtained good matches. We also tried to look into the effect of the result of the structural and electronic characterizations on the bolometric measurements.

We then went on to pattern and characterize a 2×2 focal plane array of bolometers. We looked into the thermal crosstalk limited resolution of the arrays. We saw that a high response level is preferable to avoid thermal crosstalk. We also saw that our crosstalk data fits published theories. We described a method to quantized crosstalk. We saw that the produced bolometers can be used for imaging.

REFERENCES

Aboudihab, I., Gilabert, A., Azoma, A. and Roustan, J. C. 1994. Superconducting YBa_2,Cu_3,O_{7-x} thin film bolometer for infrared radiation. *Supercond. Sci. Technol.* 7:80-83.

Abrikosov, A. A. 1957. On the Magnetic Properties of Superconductors of the Second Group. *Soviet Physics JETP* 5:6.

Alain, C., Phong, L. N. and Shih, L. 1997. MgO micromachining for superconductor focal plane arrays. *Proc. SPIE* 3061:974.

Anderson, P. W. 1987.The resonating valence bond state in La2CuO4 and superconductivity. *Science* 235:4793.

Appel, J.W. and Galeazzi, M. 2006. Two models for bolometer and microcalorimeter detectors with complex thermal architectures. *Nuclear Instruments and Methods in Physics Research A* 562:272280.

Avci, I., Algul, B. P., Bozbey, A., Akram, R., Tepe, M. and Abukay, D. 2007. Investigation of Thermal Cycling Effect on the Device Performance of YBa_2,Cu_3,O_7-DC-SQUIDs. *Supercond. Sci. Technol.* 20:944-949.

Ayache, J. 2006. Grain boundaries in high temperature superconducting ceramics. *Philosophical Magazine* 86:15.

Bardeen, J., Cooper, L. N. and Schrieffer, J. R. 1957. Theory of Superconductivity. *Phys. Rev.* 108:5.

Bechhoefer, J. 2005. Feedback for physicists: A tutorial essay on control. *Reviews of Modern Physics* 77.

Bednorz,J. G. and Müller, K. A. 1986. Possible high Tc superconductivity in the Ba-La-Cu-O system. *Z. Physik B* 64(1):189193.

Bennemann, K. H. and Ketterson, J. B., eds. 2008. *The Physics of Superconductors* Germany: Springer.

Berman, R., Foster, E. L. and Ziman, J. M. 1955. Thermal Conduction in Artificial Sapphire Crystals at Low Temperatures in Nearly Perfect Crystals. *Proc. R. Soc. Lond.* A19:231:1184.

Bozbey, A., Fardmanesh, M., Schubert, J. and Banzet, M. 2006. Electrical-Contact Free Readout of the Response of Superconductive Bolometer Arrays Using the Thermal Crosstalk. *Applied Optics*. 45:28.

Brasunas, J. C. and Lakew, B. 1994. High Tc Superconductor Bolometer with Record Performance. *Appl. Phy. Lett.* 64:6.

Brasunas, J. C., Moseley, S. H., Lakew, B., Ono, R. H., McDonald, D. G., Beall, J. A. and Sauvageau, J. E. 1989. Construction and performance of a high-temperature-superconductor composite bolometer. *J. Appl. Phys.* 66:9.

Brasunas, J.C. (Khare, N., ed.) 2003. High-Temperature Superconducting IR Detectors. *Handbook of High-temperature Superconductor Electronics*. CRC Press.

Burns, G. 1991. *High-temperature Superconductivity: An Introduction* Elsevier Science & Technology.

Chen, H. Z., Chow, T. C., Hong, M. T., Lin, T. L., Lin, K. S., Cheng, Y. F., Chen, Y.C. and Chou, H. 1997. The broadband optical detection of precipitational free YBCO thin films *Physica C* 274:24-37.

Cherednichenko, S., Ronnung, F., Gol'tsman, G., Kollberg, E. and Winkler, D. 2000. Hot-electron bolometer mixer *Physica C: Superconductivity*. 4:341-348:2653-2654.

Chou, H., Chen, H. Z., Chow, T. C., Lin, T. L., Chen, Y. C. and Wang, D. P. 1996. Surface Morphology Effect to Photoresponse in High Tc Superconducting Microbridge *Appl. Phys. Lett.* 69:1306-1308.

Delerue, J., Gaugue, A., Testé, P., Caristan, E., Klisnick, G., Redon, M. and Kreisler, A. 2003. YBCO Mid-Infrared Bolometer Arrays. *IEEE Transactions on Applied Superconductivity* 13:2.

Dereniak, E. L. and Boreman, G. D. 1996. *Infrared Detectors and Systems.* Wiley-Interscience.

Ditmars, D. A., Ishihara, S., Chang, S. H., Bernstein, G. and West, E. D. 1982. Enthalpy and Heat-Capacity Standard Reference Material Synthetic Sapphire (alpha-Al_2O_3 from 10 to 2550K. *J. Res. Nat. Bur. Stand.* 87:2:159-163.

Dwir, B. and Pavuna, D. 1992. A sensitive YBaCuO thin film bolometer with ultrawide wavelength response. *J. App. Phys.* 72:9.

Eidelloth, W. Optical response of highly oriented YBCO thin films. *IEEE Trans. Magn.* 27:2828.

Fardmanesh, M. 2001. Analytic thermal modeling for dc-to-midrange modulation frequency responses of thin-film high-Tc superconductive edge-transition bolometers. *Applied Optics* 40:7.

Fardmanesh,M., Rothwarf, A. and Scoles, K.J. 1995. Low and midrange modulation frequency response for YBCO infrared detectors: interface effects on the amplitude and phase. *IEEE Trans. on Appl. Superconductivity* 8:1.

Fardmanesh, M., Rothwarf, A. and Scoles, K.J. 1995. YBa_2,Cu_3,$O_{7-\delta}$ Infrared Bolometers: Temperature Dependent Responsivity and Deviations From The dR/dT curve. *Journal of Applied Physics* 77:9:4568-4575.

Fardmanesh, M., Scoles, K. and Rothwarf, A. 1998. DC Characteristics of Patterned YBa2Cu3O Superconducting Thin-Film Bolometers: Artifacts Related to Joule Heating, Ambient Pressure, and Microstructure. *IEEE Transactions on Applied Superconductivity* 8:2.

Fardmanesh, M., Scoles, K. and Rothwarf, A. 1999. Control of the responsivity and the detectivity of superconductive edge-transition YBa_2,Cu_3,$O_{7-\delta}$ bolometers through substrate properties. *Appl. Optics* 38:22.

Galeazzi, M. and McCammon, D. 2003. Microcalorimeter and bolometer model. *Journal of Applied Physics* 93:8.

Gaugue, A., Testé, P., Delerue, J., Gensbittel, A., De Luca, A., Kreisler, A., Voisin, F., Klisnick, G. and Redon, M. 2001. YBaCuO Mid-Infrared Bolometers: Substrate Influence on Inter-Pixel Crosstalk. *IEEE Transactions on Applied Superconductivity*. 11:1.

Ginzburg, V. L. and Landau, L. D. 1950. *Zh. Eksp. Teor. Fiz.* 20:1064.

Giuliani, A., Arnaboldi, C., Brofferio, C., Bucci, C., Cremonesi, O., Fiorini, E., Nucciotti, A., Pavan, M., Pedretti, M., Pessina, G., Pirro, S., Pobes, C., Previtali, E., Sisti, M., Vanzini, M. and Zanotti, L. 2002. Dark Matter Search In The Milano Double Beta Experiment And Prospects For The CUORE Project. *Nuclear Physics B (Proc. Suppl.)* 110:64.

Goetz, A. 1939. The Possible Use of Superconductivity for Radiometric Purposes. *Phys. Rev.* 55:1270.

Goldie, D. J., Audley, M. D., Glowacka, D. M., Tsaneva, V. N. and Withington, S. 2008. Transition edge sensors for bolometric applications: responsivity and saturation. *J. Appl. Phys.* 103:084509.

Gorter, C. J. and Casimir, H. B. G. 1934. *Physik. Z.* 35:963 (1934).

Hao, J. H., Zhou, F. Q., Zhou, X. R., Sun, H. D., Yi, X. J. and Li, Z. G. 1993. Responsivity calculation and measurement of YBCO optical detector. *IEEE Transactions on Applied Superconductivity* 3:1.

Hilton, G. C., Beall, J. A., Deiker, S., Beyer, J., Vale, L. R., Reintsema, C .D., Ullom J. N. and Irwin, K. D. 2003. Surface Micromachining for Transition-Edge Detectors. *IEEE Transactions on Applied Superconductivity* 13:2.

Hooge, F. N., Kleinpenning, T. G. M. and Vandamme, L. K. J. 1981. Experimental studies on l/f noise. *Rep. Prog. Phys.* 44.

Hu, Q. and Richards, P. L. 1989. Design analysis of a high Tc superconducting microbolometer. *Appl.Phys.Lett.* 55:23.

Johnson, B. R., Ohnstein, T., Han, C. J., Higashi, R., Kruse, P. W., Wood, R. A., Marsh, H. and Dunham, S. B. 1993. $YBa_2Cu_3O_7$ Superconductor microbolometer arrays fabricated by silicon micromachining. *IEEE Transactions on Applied Superconductivity* 3:1.

Josephson, B. D. Possible New Effects in Superconducting Tunnelling. *Phys. Lett.* 1:251.

Kakehi, Y., Yotsuya, T., Kusaka, T., Suzuki, Y., Ogawa, S. and Imokawa, H. 1998. Infrared radiation detector with $YBa_2Cu_3O_X$ thin film. *Jpn. J. Appl. Phys.* 37:4774.

Karmanenko, S. F., Semenov, A. A., Khrebtov, I. A., Leonov, V. N., Johansen, T. H., Galperin, Yu. M., Bobylk, A. V., Dedoboretzk, A. I., Gaevskik, M. E., Lunevk A. V. and Surisk, R. A. 2000. Fabrication process and noise properties of antenna-coupled microbolometers based on superconducting YBCO films. *Supercond. Sci. Technol.* 13:273286.

Kelly, M. K., Barboux, P., J.-M. Tarascon, J.-M. and Aspnes, D. E. 1989. Optical properties of copper-oxygen planes in superconducting oxides and related materials *Phys. Rev. B* 40:6797.

Khrebtov, I. A. 2002. Noise properties of high temperature superconducting bolometers. *Fluctuation and Noise Letters.* 2:2:R51-R70.

Kreisler, A. J. and Gaugue, A. 2000. Recent progress in high-temperature superconductor bolometric detectors: from the mid-infrared to the far-infrared (THz) range. *Supercond. Sci. Technol.* 13:1235-1245.

Lacoe, R. C., Hurrell, J. P., Springer, K., Raistrick, I. D., Hu, R., Burch, J. F. and Simon, R. S. 1991. Low Frequency 1/f Noise Measurements In YBa_2,Cu_3,O_7 Thin Films and The Implications For Hts Ir Detectors. *IEEE Transactions on Magnetics* 27:2.

Lakew, B., Brasunas, J.C., Aslam, S. and Pugel, D.E. 2004. High-Tc transition-edge superconducting (TES) bolometer on a monolithic sapphire membrane - construction and performance. *Sensors Actuat. A-Phys.* 114:1:36-40.

Lesquey, E., Gunther, C., Flament, S., Desfeux, R., Hamet, J. F. and Robbes, D. 1995. Progress Toward a low-noise temperature regulation using a superconductive high-T_c microbridge. *IEEE Transactions of Applied Superconductivity* 5:2.

Leung, M., Broussard, P. R., Claassen, J. H., Osofsky, M. and Wolf, S. A. 1987. Optical detection in thin granular films of Y-Ba-Cu-O at temperatures between 4.2 and 100 K. *Appl. Phys. Lett.* 51:2046.

Li, K., Johnson, J. E. and Aker, B. W. 1993. High responsivity YBa2Cu3O7-x microbolometers with fast response times. *J. Appl. Phys.* 73:1531.

Li, X., Shi, X., Wang, L., Li, S., Qi, Y., Yang, B., Wang, X. and Shi, D. 1994. A small-area high-T, superconducting bolometer with Y-Ba-Cu-0 thin film. *Rev. Sci. Instrum.* 65:l.

London, F. and London, H. 1935. The Electromagnetic Equations of the Supraconductor. *Proc. Roy. Soc.* A:149.

Maxwell, E. 1950. Isotope Effect in the Superconductivity of Mercury. *Phys. Rev.* 78:477.

Mei, Y. J., Wang, M. W., Hsieh, W. K., Chang, C. Y., Huang, C. J. and Tseng, T. Y. 1993. Bolometric Response of High Temperature Superconducting Thin Films. *Chinese Journal of Physics* 31:6-11.

Meissner, W. and Ochsenfeld, R. 1933. Ein neuer Effekt bei Eintritt der Supraleitfahigkeit. *Die Naturwissenschaften* 21:787 (1933).

Mischke, M. 2003. Wavelength Dependence of the Photoresponse of a Yittirium-Barium-Copper-Oxide Thin Film (Ph. D. Thesis). University of Notre Dame.

Moftakharzadeh, A., Kokabi, A., Bozbey, A., Ghods-Elahi, T., Vesaghi, M., Khorasani, S., Banzet, M., Schubert, J. and Fardmanesh, M. Detectivity of YBCO transition edge bolometer: modulation frequency, bias current and absorber effects. *J. Phys.: Conf. Ser.* 97:012009.

Mourachkine, A. 2002. *High-Temperature Superconductivity in Cuprates–The Nonlinear Mechanism and Tunneling Measurements Series: Fundamental Theories of Physics Vol. 125* Germany: Springer.

Nelms, N. and Dowson, J. 2005. Goldblack coating for thermal infrared detectors. *Sensors and Actuators A* 120:403407.

Norton, D. P. 1998. *Annu. Rev. Mater. Sci.* 28:299-343.

Norton, P. R. 1999. Infrared detectors in the next millennium. *Proc. SPIE* 3698:652-665.

Ohring, M. 2001. *The Materials Science of Thin Films*. Academic Press.

Onnes, H. K. 1911. The resistance of pure mercury at helium temperatures. *Commun. Phys. Lab. Univ. Leiden*.

Rahman, F. 2006. Superconducting detectors in astronomy. *Contemporary Physics* 47:4.

Richards, P. L. 1994. Bolometers for infrared and millimeter waves. *J. Appl. Phys.* 76:1.

Richards, P. L., Clarke, J., Leoni, R., Lerch, P. H., Verghese, S., Beasley, M. E., Geballe, T. H., Hammond, R. H., Rosenthal, P. and Spielman, S. R. 1989. Feasibility of the high T superconducting bolometer. *Applied Physics Letters* 54:283.

Richards, P. L., Verghese, S., Geballe, T. H. and Spielman, S. R. 1988. The high T_c superconducting bolometer. *IEEE Trans. Magn.* MAG-25:1335-1338.

Rieke, G. H. 2007. Infrared detector arrays for astronomy. *Annu. Rev. Astron. Astrophys.* 45:77115

Rogalski, A. 2002. Comparison of performance limits of infrared detector materials. *Proc. SPIE* 4650:117127.

Rogalski, A. 2003. Infrared detectors: status and trends. *Progress in Quantum Electronics.* 27:59210.

Saint-James, D., Sarma, G. and Thomas, E. J. 1969. *Type II superconductivity.* Oxford, New York:Pergamon Press.

Schlechtweg, M. and Tessmann, A. 2006. From 100 GHz to Terahertz Electronics - Activities in Europe. *Compound Semiconductor Integrated Circuit Symposium*.

Seeber, B., ed. 1998. *Handbook of Applied Superconductivity.* Institute of Physics Publishing.

Semenov, A. D., Goltsman G. N. and Sobolewski, R. 2002. Hot-electron effect in superconductors and its applications for radiation sensors. *Supercond. Sci. Technol.* 15:R1-R16.

Shubnikov, L. V.,Khotkevich, V. I., Shapelev. D. Yu and Rjabinin, Yu N. 1937. *Zh. Eksp. Teor. Fiz.* 7:221.

Tinkham, M. 1975. *Introduction to Superconductivity.* Krieger Pub. Co.

Tyutyundzhiev, N. Bolometric Response of YBCO Thin Films to Blackbody Radiation. *Bulgarian Journal of Physics* 21:36-44.

Uher, C. and Kaiser, A. B. Thermal Transport Properties of $YBa_2Cu_3O_7$ Superconductors. *Phys. Rev. B* 36:10.

van Duzer, T., Turner, C. W. 1998. *Principles of Superconductive Devices and Circuits.* Prentice Hall.

Verghese, S., Richards, P. L., Char, K. and Sachtjen, S. A. 1991. Fabrication of an infrared bolometer with a high Tc superconducting thermometer. *IEEE Transactions on Magnetics* 27:2:4.

Vincent, J. D. 1989. *Fundamentals of Infrared detector Operation and Testing*. John Wiley & Sons.

W. Prusseit. 2000. Methods of HTS deposition: thermal evaporation. *THEVA GmbH: internal report*.

Wördenweber, R. 1999. Growth of high-Tc thin films. *Supercond. Sci. Technol.* 12:R86.

Wentworth, S. M. and Neikirk, D. P. 1990. Far-Infrared Composite Microbolometers. *IEEE MTT-S Digest*. 1309-1310.

Winkler, D. 2003. Superconducting analogue electronics for research and industry. *Supercond. Sci. Technol.* 16:15831590.

Wu, M.K., Ashburn, J.R., Torng, C.J., Hor, P.H. and Meng, R.L. 1987. Superconductivity at 93 K in a new mixed-phase Y-Ba-Cu-O compound system at ambient pressure. *Phys. Rev. Lett.* 58:908

Yvon, D., Panh, J., Land, J., Eng, P., Briand, N., Guyot, G., Pons, G, Narbonne, J., Brienza, D., DeBernardis, P. and Masi, S. 2008. My Bolometer is Running a Fever, or Why Very Low Noise Performances Requires Global Design of the Apparatus. *J. Low Temp. Phys.* 151:448458.

Zehnder, A. 1995. Response of superconductive films to localized energy deposition. *Phys. Rev. B* 52:17.